STABILITY ANALYSIS OF ADVANCED COMPOSITE ARCHES

ZHANPENG LIU

A thesis in fulfilment of the requirements for the degree of Master of Philosophy

School of Civil and Environmental Engineering

University of New South Wales

Sydney, Australia

2019

Thesis/Dissertation Sheet

Surname/Family Name	:	**Liu**
Given Name/s	:	**Zhanpeng**
Abbreviation for degree as give in the University calendar	:	**M. Phil.**
Faculty	:	**Engineering**
School	:	**School of Civil and Environmental Engineering**
Thesis Title	:	**Stability analysis of advanced composite arches**

Abstract 350 words maximum: (PLEASE TYPE)

Advanced composite arches can deliver superior mechanical performance to fulfil the criteria of the modern engineering design. Functionally graded material (FGM) and nano-reinforced materials are two of the most efficient advanced composite materials. Because of the material property varies continually in the cross-section, the structural analysis is very challenging comparing to homogeneous materials.

This dissertation aims to develop an analytical framework in the static behaviour of FG arches and nano-reinforced arches. Firstly, the linear static responses and the geometric nonlinear static responses are analysed; the significant of the geometric nonlinear analysis is stated by result comparison. Secondly, the static buckling analysis is conducted; particularly, two buckling modes are discussed, which are the limit point buckling and the bifurcation buckling. Finally, the equilibrium paths are illustrated in different buckling scenarios.

Energy methods are adopted to establish the equilibrium differential equations. To verify the results of the proposed methods, numerical models are developed by using finite element analysis (FEA) software ANSYS. In the FE modelling, the cross-section of the arch is discretised into multiple layers to simulate the variation of the material property. From the numerical verification, the proposed analytical solution agrees well to the numerical models. Furthermore, a renovative nano-composite arch – the Functionally Graded Porous - Graphene Platelets Reinforced (FGP-GPLRC) arch is proposed in this research. By using the proposed analytical equations, the static responses and buckling behaviours is well analysed. From the results, the proposed FGP-GPLRC arch has an impressive strength-weight ratio against buckling. Compare to homogeneous arches, the FGP-GPLRC arch has a significant reduction in the self-weight without scarifying the buckling capacity. This dissertation makes a notable contribution to those design engineering where requires a high strength arch structure with strict size or weight limitation. Also, it provides a useful references and benchmarks for the researchers in the area of advanced composite arches.

ORIGINALITY STATEMENT

‘I hereby declare that this submission is my own work and to the best of my knowledge it contains no materials previously published or written by another person, or substantial proportions of material which have been accepted for the award of any other degree or diploma at UNSW or any other educational institution, except where due acknowledgement is made in the thesis. Any contribution made to the research by others, with whom I have worked at UNSW or elsewhere, is explicitly acknowledged in the thesis. I also declare that the intellectual content of this thesis is the product of my own work, except to the extent that assistance from others in the project's design and conception or in style, presentation and linguistic expression is acknowledged.’

Signed ……………………………………………..............

Date …………………………………………………..........

AUTHENTICITY STATEMENT

'I certify that the Library deposit digital copy is a direct equivalent of the final officially approved version of my thesis. No emendation of content has occurred and if there are any minor variations in formatting, they are the result of the conversion to digital format.'

INCLUSION OF PUBLICATIONS STATEMENT

UNSW is supportive of candidates publishing their research results during their candidature as detailed in the UNSW Thesis Examination Procedure.

Publications can be used in their thesis in lieu of a Chapter if:

- The student contributed greater than 50% of the content in the publication and is the "primary author", ie. the student was responsible primarily for the planning, execution and preparation of the work for publication
- The student has approval to include the publication in their thesis in lieu of a Chapter from their supervisor and Postgraduate Coordinator.
- The publication is not subject to any obligations or contractual agreements with a third party that would constrain its inclusion in the thesis

Please indicate whether this thesis contains published material or not.

☐ *This thesis contains no publications, either published or submitted for publication (if this box is checked, you may delete all the material on page 2)*

☐ *Some of the work described in this thesis has been published and it has been documented in the relevant Chapters with acknowledgement (if this box is checked, you may delete all the material on page 2)*

☒ *This thesis has publications (either published or submitted for publication) incorporated into it in lieu of a chapter and the details are presented below*

CANDIDATE'S DECLARATION

I declare that:

- I have complied with the Thesis Examination Procedure
- where I have used a publication in lieu of a Chapter, the listed publication(s) below meet(s) the requirements to be included in the thesis.

Name	Signature	Date (dd/mm/yy)

Postgraduate Coordinator's Declaration (to be filled in where publications are used in lieu of Chapters)

I declare that:

- the information below is accurate
- where listed publication(s) have been used in lieu of Chapter(s), their use complies with the Thesis Examination Procedure
- the minimum requirements for the format of the thesis have been met.

PGC's Name	PGC's Signature	Date (dd/mm/yy)

For each publication incorporated into the thesis in lieu of a Chapter, provide all of the requested details and signatures required

<table>
<tr><td colspan="7">Details of publication #1:
Full title: Nonlinear behaviour and stability of functionally graded porous arches with graphene platelets reinforcement
Authors: Zhanpeng LIU, Chengwei YANG, Wei GAO, Di WU and Guoyin LI
Journal name: International Journal of Engineering Science
Volume/page numbers: 139/ 37-56
Date accepted/ published: 15 December 2018</td></tr>
<tr><td>Status</td><td>Published</td><td>☒</td><td>Accepted and In press</td><td></td><td>In progress (submitted)</td><td></td></tr>
<tr><td colspan="7">The Candidate's Contribution to the Work
As the first author of this publication, the candidates contributeed more than 50% of the work and carried out the research work includes the literature review, analytical equations derivation, numerical modelling, results validation, article writing, revisions and proofreading.</td></tr>
<tr><td colspan="7">Location of the work in the thesis and/or how the work is incorporated in the thesis:
This publication is located in the Chapter 4 in this thesis. It presents a newly proposed light weight nano-composite arches, the static responses and stability analysis is studied.</td></tr>
<tr><td colspan="7">Primary Supervisor's Declaration
I declare that:
• the information above is accurate
• this has been discussed with the PGC and it is agreed that this publication can be included in this thesis in lieu of a Chapter
• All of the co-authors of the publication have reviewed the above information and have agreed to its veracity by signing a 'Co-Author Authorisation' form.</td></tr>
<tr><td colspan="2">Supervisor's name</td><td colspan="3">Supervisor's signature</td><td colspan="2">Date (dd/mm/yy)</td></tr>
</table>

<table>
<tr><td colspan="3">Co-author's declaration
I authorise the inclusion of this publication in the student's thesis and certify that:
• the declaration made by the student on the declaration for a thesis with publication form correctly reflects the extents of the student's contribution to this work;
• the student contributed greater than 50% of the content of the publication and is the "primary author" ie. the student was responsible primarily for the planning, execution and preparation of the work for publication.</td></tr>
<tr><td>Co-author's name</td><td>Co-author's signature</td><td>Date (dd/mm/yy)</td></tr>
<tr><td></td><td></td><td></td></tr>
<tr><td></td><td></td><td></td></tr>
<tr><td></td><td></td><td></td></tr>
<tr><td></td><td></td><td></td></tr>
</table>

Acknowledgements

First of all, I’d like to sincerely express my appreciation to my supervisors Professor Wei Gao and Associate Professor Guoyin Li for their invaluable help throughout my research work, it is impossible to finish the research work without their guidance. Also, it is my great honour to work with my colleague Dr. Di Wu and Dr. Chengwei Yang, I am grateful for their advises and assistance in the research work.

Secondly, I’d like to deeply appreciate the support from my family – my parents Qianguo Liu and Xing Liu, my wife Min Hu and my daughter Mika Liu. Without their love and faith in me, this thesis can never be accomplished.

At the end, I am greatly honoured to be sponsored by Australian Government Research Training Program (RTP) Scholarship. I’d like to thank Australian Government for the financial support to help me to complete this research work.

Abstract

Advanced composite arches can deliver superior mechanical performance to fulfil the criteria of the modern engineering design. Functionally graded material (FGM) and nano-reinforced materials are two of the most efficient advanced composite materials. Because of the material property varies continually in the cross-section, the structural analysis is very challenging comparing to homogeneous materials.

This dissertation aims to develop an analytical framework in the static behaviour of FG arches and nano-reinforced arches. Firstly, the linear static responses and the geometric nonlinear static responses are analysed; the significant of the geometric nonlinear analysis is stated by result comparison. Secondly, the static buckling analysis is conducted; particularly, two buckling modes are discussed, which are the limit point buckling and the bifurcation buckling. Finally, the equilibrium paths are illustrated in different buckling scenarios.

Energy methods are adopted to establish the equilibrium differential equations. To verify the results of the proposed methods, numerical models are developed by using finite element analysis (FEA) software ANSYS. In the FE modelling, the cross-section of the arch is discretised into multiple layers to simulate the variation of the material property. From the numerical verification, the proposed analytical solution agrees well to the numerical models. Furthermore, a renovative nano-composite arch – the Functionally Graded Porous - Graphene Platelets Reinforced (FGP-GPLRC) arch is proposed in this research. By using the proposed analytical equations, the static responses and buckling behaviours is well analysed. From the results, the proposed FGP-GPLRC arch has an impressive strength-weight ratio against buckling. Compare to homogeneous arches, the FGP-GPLRC arch has a significant reduction in the self-weight without scarifying the

buckling capacity. This dissertation makes a notable contribution to those design engineering where requires a high strength arch structure with strict size or weight limitation. Also, it provides a useful references and benchmarks for the researchers in the area of advanced composite arches.

TABLE OF CONTENTS

List of Figures

Nomenclature

γ	Porosity distribution coefficient
ε	Longitudinal normal strain
ε_b	Bending strain
ε_m	Membrane strain
ε_{mb}	Buckling membrane strain
η_L^{GPL}, η_W^{GPL}	Dimension coefficient of the graphene platelets
θ	Angular coordinate
Λ_{GPL}	Weight fraction of the GPLs reinforcement in percentage
Π	Total potential energy
ρ	Density
ρ_{GPL}	Density of GPLs
ρ_M	Density of metal matrix
ρ_1	Density coefficient
σ	Stress
φ	Half of the included angle of arch
ξ_L^{GPL}, ξ_W^{GPL}	Elastic modulus coefficient of nanocomposites
A	Area of the cross section

$A_{f1}, A_{f2}, A_{f3}, A_{f4}$ Coefficients for fix-supported arches

$A_{p1}, A_{p2}, A_{p3}, A_{p4}$ Coefficients for pin-supported arches

$B_{f1}, B_{f2}, B_{f3}, B_{f4}$ Coefficients for fix-supported arches

$B_{p1}, B_{p2}, B_{p3}, B_{p4}$ Coefficients for pin-supported arches

C_{θ}, C_{φ} Coefficients

$D_{f1}, D_{f2}, D_{f3}, D_{fsb1}, D_{fsb2}, D_{fsb3}, D_{fvb1}, D_{fvb2}, D_{fvb3}$ Coefficients for fix-supported arches

$D_{p1}, D_{p2}, D_{p3}, D_{psb1}, D_{psb2}, D_{psb3}, D_{pvb1}, D_{pvb2}, D_{pvb3}$ Coefficients for pin-supported arches

E Elastic modulus

E_M Elastic modulus of metal matrix

E_{max} Maximum elastic modulus

E_{min} Minimum elastic modulus

E_i Elastic modulus of the inner core

E_o Elastic modulus of the outer shell

E_1 Elastic modulus of the non-porous nanocomposite structures

e_o Porosity coefficient

e_m Mass coefficient

f The fall of the arch

K_a Axial stiffness

K_b Bending stiffness

k Power-law exponent

L	The span of the arch
l_{GPL}	Length of the graphene platelets
M	Bending moment
M_c	The central bending moment
M_f	Nonlinear bending moment for fix-supported arches
$M_{f,linear}$	Linear bending moment for fix-supported arches
M_p	Nonlinear bending moment for pin-supported arches
$M_{p,linear}$	Linear bending moment for pin-supported arches
N	Axial compressive force
N_c	The central axial compressive force
N_{cr}	The critical compressive force of instability
N_f	Nonlinear compressive force for fix-supported arches
$N_{f,linear}$	Linear compressive force for fix-supported arches
N_p	Nonlinear compressive force for pin-supported arches
$N_{p,linear}$	Linear compressive force for pin-supported arches
o	The origin of angular coordinate
q	The sustained uniformly distributed radial load
q_{bb}	Anti-symmetric buckling load
q_{sb}	Symmetric snap-through buckling load
R	Initial radius of arch

r Radius of the cross section

r_e Effective radius of gyration

S_θ, S_φ Coefficients

t_{GPL} Thickness of the graphene platelets

V Volume

V_{GPL} Volume fraction of GPLs

v Radial displacement

$\tilde{v}$ $= v/R$ Dimensionless radial displacement

$\tilde{v}_b$ Dimensionless radial buckling displacement

$\tilde{v}_f$ Nonlinear dimensionless radial displacement for fix-supported arches

$\tilde{v}_{f,linear}$ Linear dimensionless radial displacement for fix-supported arches

$\tilde{v}_p$ Nonlinear dimensionless radial displacement for pin-supported arches

$\tilde{v}_{p,linear}$ Linear dimensionless radial displacement for pin-supported arches

w Axial displacement

w_{GPL} Width of the graphene platelets

$\tilde{w}$ $= w/R$ Dimensionless axial displacement

$\tilde{w}_b$ Dimensionless axial buckling displacement

$\tilde{w}_f$ Nonlinear dimensionless axial displacement for fix-supported arches

$\tilde{w}_{f,linear}$ Linear dimensionless axial displacement for fix-supported arches

$\tilde{w}_p$ Nonlinear dimensionless axial displacement for pin-supported arches

$\tilde{w}_{p,linear}$ Linear dimensionless axial displacement for pin-supported arches

y Coordinate of the point in the principle axis

Z Radial axis in the cross section

Chapter 1

Introduction

1.1 Motivation of research

Arch was adopted in structure design since thousands of years ago, it has been testified as one of the most efficient engineering structures by the latest research in topology optimisation (Zuo Z.H. et al. 2009). It widely used in engineering design as shown in Figure 1.1. The stability is one of the primary considerations in arch design because it undergoes compressive force rather than tension. The buckling mechanism is complicated and can be triggered by various reasons such as structure imperfections, load eccentricity and variations of material properties. Buckling as a major failure mode in many engineering practises may lead to severe consequences. On the other hand, the composite material is widely used in the engineering industry and is approved to be a feasible method in mechanical performance improvement. However, for those advanced composite `material includes functionally graded material (FGM), porous steel and nanoplatelet reinforced nanocomposite material, there is lack of design code/standard for such a structure to be applied in general engineering practise. Thus, the buckling analysis is of paramount importance for the proposed composite arches to prove its feasibility in engineering implementation. This research is to investigate the stability analysis of advanced composite arches, hence, contribute to a stronger, lighter and more environmentally friendly design arches in the engineering industry.

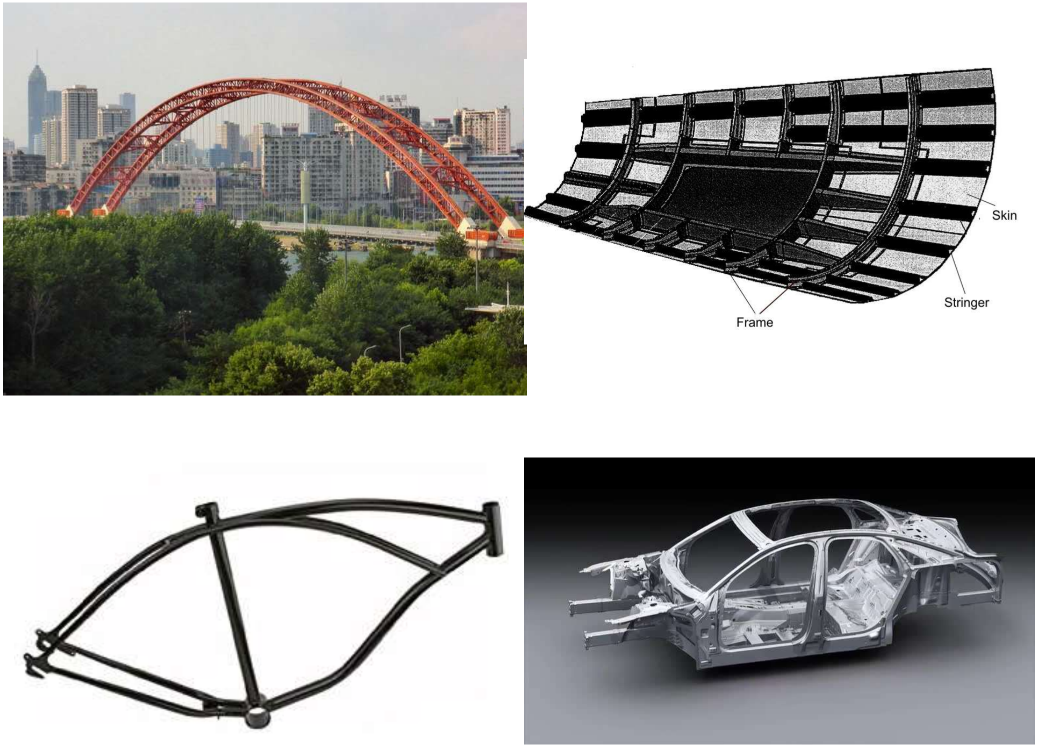

Figure 1.1 Arches in engineering design

1.2 Objective and scope

From the literature review, the stability analysis of advanced composite arches is rarely found from the open literature. The objective of this thesis is to contribute the enhancement of structural analysis of advanced composite arches, thus to propose advanced composite arches that can be adopted for those practical engineering design which has extremely requirement in weight, spacing and strength. Original research will be conducted to develop analytical approaches with enhancement in the result accuracy and computation efficiency. This analytical approach can be potentially adopted as a benchmark for FEM development, reliability analysis and numerical experiments.

Also, this thesis proposes a practical structure design framework for advanced composite arch structures. Explicitly, the proposed research will conduct following investigations in advanced composite arches including:

1. Establish an analytical analysis framework for linear and geometrically nonlinear static response.
2. Establish an analytical analysis framework for buckling analysis

This thesis is to investigate the in-plane static behaviour includes the linear, geometrically nonlinear, and the buckling analysis of composite arches. It proposed the analytical solution and validated by newly established numerical modelling. Firstly, the analytical solution of the composite arch will be derived by using potential energy method. The differences between the linear solution and the geometrically nonlinear solutions will be demonstrated and compared. Secondly, the various buckling modes will be investigated including the limit point and the bifurcation scenarios. The buckling strength and buckling modes switches are calculated and demonstrated by examples. Then the equilibrium path will be obtained to illustrates both pre-buckling and post-buckling behaviour considering the geometric nonlinearity. Finally, numerical examples will be studied by adopting various material distribution and geometric properties; the advantage of the proposed advanced composite arches will be presented.

1.3 Outline of thesis

This thesis consists of five chapters, a brief summary of the contents is presented in as following:

Chapter 1 presents the introduction of the thesis, and consists of the research motivation, objective, thesis outline and the list of publications.

Chapter 2 presents a detailed literature review in the area of mechanics of arches structures, the current composite arch structures and the graphene platelet (GPL) and GPL reinforced structures.

Chapter 3 presents the research work in the functionally graded (FG) arches. The in-plane static responses and buckling analysis of FG arches with pin-pin and fix-fix supports are investigated. Analytical linear/nonlinear solutions are derived by adopting the virtual energy method. Also, a numeric model is established by using commercial finite element software ANSYS 18.1. The results of the proposed method are validated, the computational accuracy and efficiency is discussed by illustration.

Chapter 4 consists of the research work published in the *International Journal of Engineering Science*. Functionally graded porous (FGP) arches with graphene platelets (GPLs) reinforcements (i.e., FGP-GPLRC arches) is newly proposed. The FGP-GPLRC arch has extraordinary mechanical performance, the strength-weight ratio against deflection and buckling is extremely high. The in-plane static analysis considering geometric nonlinearity is conducted, particularly the system responses, internal actions and the stability analysis with two buckling mode – the symmetric buckling and anti-symmetric buckling. Results are verified with the commercial FEM software ANSYS 18.1, the proposed method increases the calculation efficiency amazingly while the accuracy is testified.

Chapter 5 concludes the thesis; the conducted research work is summarised. Recommendations of the future research in structural analysis of advanced composite arches are proposed.

1.4 List of publications

One journal paper and two conference papers are published during the research studies including:

Journal Paper:

Zhanpeng Liu, Chengwei Yang, Wei Gao, Di Wu and Guoyin Li. Nonlinear Behaviour and Stability of Functionally Graded Porous Arches with Graphene Platelets Reinforcements. *International Journal of Engineering Science 137 (2019)* 37-56

Conference Paper:

Zhanpeng Liu, Chengwei Yang, Wei Gao and Guoyin Li. Static Response of Functionally Graded Circular Shallow Arches with Consideration of Geometric Nonlinearity. 3rd Australian Conference on Computational Mechanics (ACCM-3), Feb 12-14 2018 Melbourne Australia. (Best paper award)

Zhanpeng Liu, Di Wu, Wei Gao and Guoyin Li. Static Buckling Analysis of Functionally Graded Shallow Arches Considering Geometric Nonlinearity. 25th Australasian Conference on Mechanics of Structures and Materials (ACMSM25), Dec 4-7 2018 Brisbane Australia.

Chapter 2

Literature Review

2.1 Introduction

Arch is one of the most efficient structures which is prevalently implemented in modern engineering designs. Aerospace and military engineers adopt arch as the major structural element to support the overall structural skeleton, which are shown in Figure 2.1, due to the specific and rigorous requirements on the weight and strength of the overall structure. Therefore, researches in the advanced arch structures with specific requirements of high strength-to-weight ratio is meaningful.

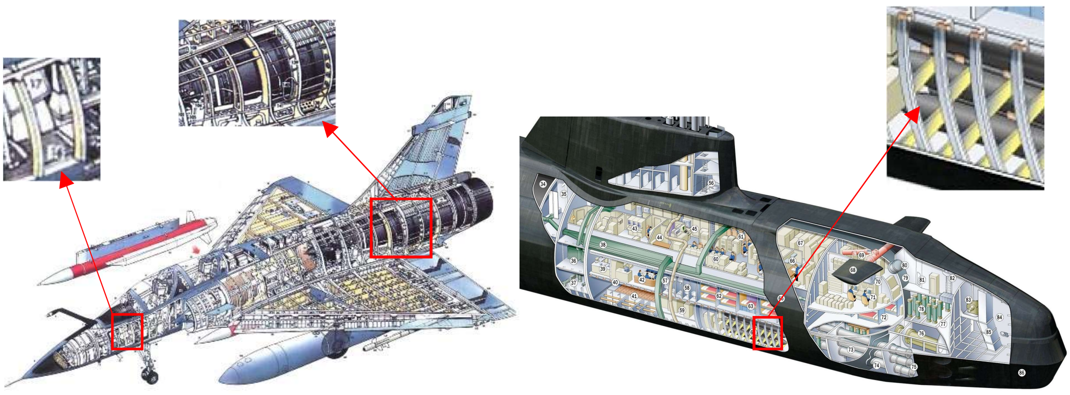

(a) (b)

Figure 2.1 Applications of arch in (a) aircraft and (b) submarine

2.2 System response and stability of arches

Research in the non-linear analysis and buckling analysis can be chased back to few decades ago. Numerous researches in stability analysis of conventional arch structure can be found from open literatures. Walker adopted Rayleigh-Ritz finite element method to investigate the large deflection behaviour of a shallow circular arch under a vertical point load, the stability including the symmetric deformation path and the post-buckling path behind the bifurcation point is presented (Walker, 1969). DaDeppo and Schmidt studied the anti-symmetric buckling of a deep, slender arch, subjected to a slowly increasing symmetric load based on the Bernoulli-Euler assumption, the result was validated by the classical eigenvalue theory of buckling of arches (DaDeppo & Schmidt, 1969). Austin presented a review article in the in-plane bending and buckling of deep arches (Austin, 1971). In 1976, Austin and Ross published their work to fill the gap of the research in arches, particularly, the critical loads and the corresponding reactions, maximum moments, and crown deflections of two-hinged and fixed, parabolic and circular arches of constant cross section subjected to a vertical concentrated load at the crown or a vertical load uniformly distributed along the arch axis. Calhoun and DaDeppo developed a curved nonlinear finite element to analyse the behaviour of slender high-rise arches undergo large deflections (Calhoun and DaDeppo, 1983); the in-plane bending and buckling modes with fixed-fixed supports were analysed. Elias and Chen proposed a geometrically nonlinear curved-beam finite element for shallow and deep arches, it can be applied to the load-deflection and buckling analysis. Wen and Suhendro developed a nonlinear curved-beam finite element for three-dimensional space system; principle of potential energy and polynomial functions is adopted (Wen and Suhendro, 1991).

Pi et al conducted a series of researches in the static response and stability of conventional arches (Pi, Bradford, & Uy, 2002; Pi & Trahair, 1996; 1998; 1999 Pi et al., 2007; Pi, Bradford & Tin-Loi, 2007). The in-plane equilibrium path and equilibrium path switches of pinned-fixed arches under an arbitrary radial concentrated load is investigated (Liu, Bradford, & Pi, 2017;). Dou presented the work in the elastic buckling of steel arches with discrete lateral braces (Dou et al., 2018). Also, other than the in-plane static stability analysis, investigations in the lateral-torsional buckling (Liu et al., 2017; Liu et al., 2017), flexural-torsional (Dou et al., 2015; 2016) and in-plane dynamic buckling (Liu et al., 2017; 2018) of arches are also published.

2.3 Current research in composite arches

2.3.1 Concrete filled steel tube (CFST) arches

CFST arch is increasingly prevalent in civil engineering, especially in the bridge engineering as shown in Figure 2.2. Because the concrete core is confined by the steel tube, the load capacity and ductility are increased significantly. Furthermore, the concrete core provides an effective resistance to increase the local buckling capacity of the steel tube. Comparing to the conventional steel arches, one of the most consideration of CFST arch is the time depended long-term strain caused by the concrete core (Arockiasamy et al., 2000; Ma and Wang, 2013; Ranzi et al., 2013). Pi et al. investigated the long-term nonlinear behaviour and in-plane buckling of the shallow CFST arches and derived the analytical solutions by virtual energy method. The in-plane strength of CFST tubular circular arches in studied by Pi et al., the commercial FE package ABAQUS/Standard is used for the nonlinear elastic and elastic-plastic analyses. Pi and Bradford presented the work in the long-term analyses of CFST arches accounting for the interval uncertainty.

Luo et al presented works in the long-term analysis of structural behaviour and stability of CFST arches in a systematic level (Luo et al., 2013a; 2013b; 2015); results shown the long-term effects, such as the creeps, shrinkage and temperature change, have a significate influence on the structural behaviour and the buckling modes. Wu et al. conducted a time-variant random interval response of CFST arches (Wu et al., 2016a; 2016b). Wu et al. researched in the non-deterministic analysis in long-term behaviours of CFST, a finite-element-based computational method is proposed for time-dependent structural stability analysis of CFST arch with uncertain parameters (Wu, Gao, & Tangaramvong, 2017a).

Figure 2.2 Applications of CFST arches in civil engineering

2.3.2 Functionally graded material (FGM) and FGM arches

In 1980s, Japanese space program proposed a revolutionary composite material - the functionally graded material (FGM) (Koizumi M. 1997). It can enhance the mechanic performance of the material, also reduce the delamination and crack under the high temperature working environment. The FGM is commonly made from two material phases - metal phase and ceramic phase. Apart from the conventional composite materials, the transition between FGM is continuous and is defined by a continuous function. Nowadays, the FGM is widely used in engineering practise. Because of its extraordinary mechanical and thermal performance, numerus researches were conducted in the investigation of the structural behaviour of the FGM structures. The free vibration analysis of FG beams is studied by Aydogdu (Aydogdu, 2007). Shaker carried out stochastic finite element analysis of the free vibration of FGM plates, the basic random variables include ceramic and metal Young's modulus and Poisson's ratio (Shaker et al. 2007). Şimşek studied the free and force vibration of FG beam subjected to a concentrated moving harmonic load (Şimşek and Kocatürk. 2009); Lagrange's equations is used under the Euler-Bernoulli beam theory. Taczała investigated the nonlinear buckling and post-buckling responses o fstiffened FGM plates in thermal environments by adopting finite element method (Taczała et al. 2017). Frikha presented their work in the static analysis of FGM shells considering the geometric nonlinearity with a discrete double directors shell element (Frikha and Dammak, 2017). Also, the non-deterministic analysis in the FG structures can be found from the open literature. Wu et al. conducted the non-deterministic analysis in the FG beam by adopting finite element method; the interval uncertainties are assumed through both Euler-Bernoulli and Timoshenko beam theories (Wu et al. 2017b); and the stochastic uncertainties area ssumed through the Euler-Bernoulli beam theories (Wu et al. 2017c).

However, there are only a few published papers can be found related to FG arches. Bateni and Eslami conducted in the non-linear in-plane stability analysis of FG circular shallow arches under central concentrated force (Bateni & Eslami, 2014) and uniform radial pressure (Bateni & Eslami, 2015). Shafiee et al investigated in the in-plane and out-of-plane buckling of FGM arches (Shafiee, Naei, & Eslami, 2006), nonlinear analytical analyses were conducted, the equilibrium path and the post-buckling behaviours were investigated in systematic level. Asgari et al carried out a non-linear thermo-elastic and buckling analysis of FG shallow arches (Asgari et al., 2014); theoretical investigation in the nonlinear thermal bending and buckling of the through-the-thickness FGM shallow arches was conducted.

2.4 GPLs and GPLs reinforced structures

Graphene platelets reinforcement is the latest nano-manufactory technology in the material science (Govorov et al., 2018; Shahverdi, & Barati 2017; Srividhya et al., 2018; Wentzel, Millers, & Sevostianov 2017). Other than its excellence in electronic and thermal performances, researches also showed that the graphene platelets (GPLs) nanocomposites have a significant improvement in mechanical properties of the matrix at low nanofiller content. Established research works have demonstrated that the GPLs reinforcement can strengthen the porous structure sufficiently without sacrificing its weight reduction advantage (Kitipornchai, Chen, & Yang, 2017; Yang, Wu, & Kitipornchai, 2017), and has a higher mechanical strength comparing to the carbon nanotubes (CNTs) (Rafiee et al., 2009).

The mechanical behaviour of functionally graded material and nano-composites have been modelled recently (Hashemi, 2016; Attia, & Rahman, 2018; Dehrouyeh-Semnani, 2018; Evci, & Gulgec, 2018; Wentzel, & Sevostianov, 2018; Taati, 2018). Furthermore, the Pioneer researchers have conducted a series of studies in mechanical behaviour of

FGP-GPLRC structures. Chen et al presented their works in the free and forced vibrations, elastic buckling, and static bending of shear deformable FGP beam (Chen, Yang, & Kitipornchai, 2015; 2016a). Kitipornchai et al investigated the free vibration and elastic buckling of FGP beam reinforced by GPLs. The nonlinear vibration and post-buckling behaviour of the FGP-GPLRC beam is studied (Chen, Yang, & Kitipornchai, 2016b). By introducing multi-layer GPLs to beam, the static buckling strength can be improved (Yang, Wu, & Kitipornchai, 2017). Wu et al conducted a series of research in the dynamic instability in thermal environment, thermal buckling and thermal post-buckling behaviours of GPLs reinforced functionally graded polymer composite beams (Wu, Kitipornchai, & Yang, 2016; Wu, Kitipornchai, & Yang, 2017a; Wu, Yang, & Kitipornchai; 2017) and plate (Wu, Kitipornchai, & Yang, 2017b). Feng et al studied the nonlinear free vibration of polymer nanocomposite beams reinforced with non-uniformly distributed graphene platelets (Feng, Kitipornchai, & Yang, 2017a; 2017b). Song et al presented research work in the free and forced vibration of functionally graded polymer composite plates reinforced with GPLs (Song, Kitipornchai, & Yang, 2017;), buckling and post-buckling of biaxially compressed functionally graded multilayer GPLs reinforced polymer composite plates (Song et al., 2017). Zhao et al conducted bending and vibration analysis of functionally graded trapezoidal nanocomposite plates reinforced with GPLs (Zhao et al., 2017). Wang et al investigated the eigenvalue buckling of GPLs reinforced functionally graded cylindrical shell (Wang et al., 2018) and with cut-out (Wang et al., 2017). Numerical methods are also adopted in the investigation of the FGP structures. Wu et al integrated a finite element method analysis framework for free and forced vibration analyses of FGP beam type structures (Wu et al., 2018a) and the non-deterministic linear elastic problem of bar-type FGP structures with uncertain-but-bounded system parameters (Wu et al., 2018b).

Huang et al studied the buckling behaviour of functionally graded graphene platelet-reinforced composite (FG-GPLRC) shallow arches with elastic rotational constraints under uniform radial load (Huang et al., 2018). Yang et al investigated the in-plane instability of functionally graded multilayer composite shallow arches reinforced with a low content of GPLs under a central point load (Yang et al., 2018).

However, the system responses and buckling analyses of the FGP-GPLRC arches have not yet been studied in the published works. The FGP-GPLRC arch combines advantages of the porous materials and nano-reinforced materials, which can fulfil the strict requirements in the lightness and the strength in modern engineering design.

Chapter 3

Static response and in-plane stability of FG arches

3.1 Introduction

This chapter presents an analytical approach to the static responses and in-plane buckling analysis of FGM circular shallow arch sustaining uniform radial pressure. Analytical solutions are derived by potential energy method based on Euler-Bernoulli beam theory. Results are verified by ANSYS APDL 18.1, the accuracy and the calculation efficiency are compared. System responses, internal actions and buckling analyses of the FGM arches are investigated. The significance of the geometric nonlinearity of FGM arches is discussed.

3.2 Linear analysis in static response

A circular FG shallow arch is considered as shown in Figure 3.1. The material properties (e.g. the Young's modulus.) vary continuously along the radial direction in the cross section. A power-law function given by Eq. (3.1) is adopted to describe the changing of Young's modulus in the cross section.

$$E_{(Z,\,k)} = (E_o - E_i)\left(\frac{Z}{r}\right)^k + E_i \qquad \text{for } 0 \le Z \le r \tag{3.1}$$

where Z is the radial axis of the cross section, r is the radius of the cross section, k is the power-law exponent, E_o and E_i denote the Young's modulus of the outer and the inner layer respectively.

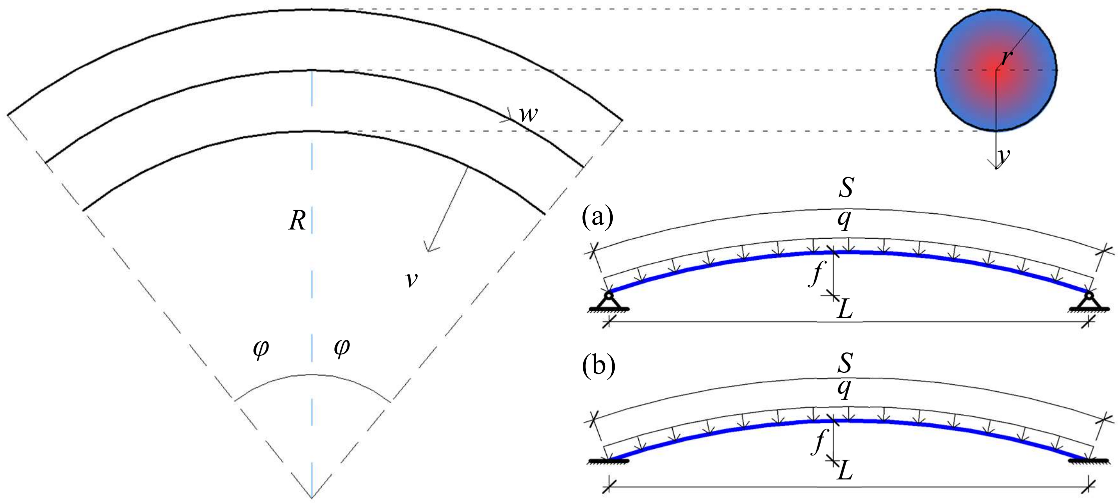

Figure 3.1 FG shallow arch under uniform distributed load with support condition: (a) pinned support, (b) fixed support

Based on the Euler-Bernoulli hypothesis, the strain at an arbitrary point is the sum of the membrane strain ε_m and bending strain ε_b while the shear strains are neglected. The linear elastic strain equation for circular arches can be obtained as (Simitses G.J., 1976):

$$\varepsilon = \varepsilon_m + \varepsilon_b = \frac{\partial \widetilde{w}}{\partial \theta} - \widetilde{v} - \frac{y}{R}\left(\frac{\partial^2 \widetilde{v}}{\partial \theta^2} + \frac{\partial \widetilde{w}}{\partial \theta}\right) \tag{3.2}$$

where $\widetilde{w}$ and $\widetilde{v}$ denote dimensionless axial and radial displacement, i.e. $\widetilde{w} = w/R$ and $\widetilde{v}$ $= v/R$.

While the arch is sustaining the uniform distributed load q and at equilibrium, the virtual potential energy vanishes:

$$\delta\Pi = \int_V \sigma \delta\varepsilon \mathrm{d}V - \int_{-\varphi}^{\varphi} qR^2 \delta\widetilde{v} \mathrm{d}\theta = 0 \tag{3.3}$$

By substituting Eq. (3.2) into Eq. (3.3) the potential energy equation of thin arches can be rewritten as:

$$\delta\Pi = \int_{-\varphi}^{\varphi} AR\sigma\delta\left[\frac{\partial\widetilde{w}}{\partial\theta} - \widetilde{v} - \frac{y}{R}\left(\frac{\partial^2\widetilde{v}}{\partial\theta^2} + \frac{\partial\widetilde{w}}{\partial\theta}\right)\right] - qR^2\delta\widetilde{v}\,\mathrm{d}\theta = 0 \tag{3.4}$$

and Eq. (3.4) can be rearranged as:

$$\delta\Pi = \int_{-\varphi}^{\varphi} -NR\left(\delta\frac{\partial\widetilde{w}}{\partial\theta} - \delta\widetilde{v}\right) - M\left(\delta\frac{\partial^2\widetilde{v}}{\partial\theta^2} + \delta\frac{\partial\widetilde{w}}{\partial\theta}\right) - qR^2\delta\widetilde{v}\,\mathrm{d}\theta = 0 \tag{3.5}$$

where N and M are compressive axial force and bending moment of the arch given in Eq. (3.6) and Eq. (3.7):

$$N = \int_A -\sigma \mathrm{d}A = -\int_A E_{(Z,k)}\varepsilon_m \mathrm{d}A = -\left(\frac{\partial\widetilde{w}}{\partial\theta} - \widetilde{v}\right)K_a \tag{3.6}$$

$$M = \int_A \sigma y \mathrm{d}A = \int_A E_{(Z,k)}\varepsilon_b y \mathrm{d}A = -\frac{1}{R}\left(\frac{\partial^2\widetilde{v}}{\partial\theta^2} + \frac{\partial\widetilde{w}}{\partial\theta}\right)K_b \tag{3.7}$$

where K_a and K_b are the axial stiffness and the bending stiffness given by Eq. (3.8) and Eq. (3.9):

$$K_a = 2\pi\int_0^r [\,(E_o - E_i)\left(\frac{Z}{r}\right)^k + E_i\,]Z\mathrm{d}Z \tag{3.8}$$

$$K_b = \pi\int_0^r [\,(E_o - E_i)\left(\frac{Z}{r}\right)^k + E_i\,]Z^3\mathrm{d}Z \tag{3.9}$$

Substituting Eq. (3.6) and Eq. (3.7) into Eq. (3.5) and performing the calculus of variations leads to equilibrium equations in the radial direction and the axial direction given by Eq. (3.10) and Eq. (3.11):

$$r_e^2\left(\frac{\partial^4\tilde{v}}{\partial\theta^4}+\frac{\partial^3\tilde{w}}{\partial\theta^3}\right)-R^2\left(\frac{\partial\tilde{w}}{\partial\theta}-\tilde{v}\right)-\frac{qR^3}{K_a}=0 \tag{3.10}$$

$$r_e^2\left(\frac{\partial^3\tilde{v}}{\partial\theta^3}+\frac{\partial^2\tilde{w}}{\partial\theta^2}\right)+R^2\left(\frac{\partial^2\tilde{w}}{\partial\theta^2}-\frac{\partial\tilde{v}}{\partial\theta}\right)=0 \tag{3.11}$$

where r_e is the effective radius of gyration given by:

$$r_e=\sqrt{\frac{K_b}{K_a}} \tag{3.12}$$

The following boundary conditions are considered to solve differential equations Eq. (3.10) and Eq. (3.11): $\tilde{v}=0$ and $\tilde{w}=0$ at $\theta=\pm\varphi$ for pin-supported FG arches and $\tilde{v}=0$ and $\frac{\partial\tilde{v}}{\partial\theta}=0$ at $\theta=\pm\varphi$ for fix-supported FG arches. Additionally, for pin-supported FG arches, the bending strain at the boundary is zero thus $\left(\frac{\partial^2\tilde{v}}{\partial\theta^2}+\frac{\partial\tilde{w}}{\partial\theta}\right)=0$ at $\theta=\pm\varphi$; for fix-supported FG arches, the slope at the boundary is zero thus $\frac{\partial\tilde{v}}{\partial\theta}=0$ at $\theta=\pm\varphi$. Hence the dimensionless axial displacements and dimensionless radial displacements can be obtained as:

$$\tilde{w}_{p,linear}=A_{p1}(A_{p2}+A_{p3}+A_{p4}) \tag{3.13}$$

where

$$A_{p1}=\frac{qR}{K_a[R^2(2\varphi\cos^2(\varphi)-3\cos(\varphi)\sin(\varphi)+\varphi)+r_e^{\,2}(\cos(\varphi)\sin(\varphi)+\varphi)]} \tag{3.14}$$

$$A_{p2}=(R^2+r_e^{\,2})\cos(\theta)\sin(\varphi)\theta \tag{3.15}$$

$$A_{p3}=-(3R^2+r_e^{\,2})\cos(\varphi)\varphi\sin(\theta) \tag{3.16}$$

$$A_{p4} = 2\cos(\varphi)R^2\sin(\varphi)\theta \tag{3.17}$$

and

$$\tilde{v}_{p,linear} = A_{p1}(B_{p1} + B_{p2} + B_{p3}) \tag{3.18}$$

where

$$B_{p1} = (R^2 + r_e^{\,2})[\varphi - \sin(\theta)\sin(\varphi)\theta] \tag{3.19}$$

$$B_{p2} = (R^2 - r_e^{\,2})\sin(\varphi)\left[\cos(\theta) - \cos(\varphi)\right] \tag{3.20}$$

$$B_{p3} = -\cos(\varphi)\varphi[R^2(3\cos(\theta) - 2\cos(\varphi)) + r_e^{\,2}\cos(\theta)] \tag{3.21}$$

for pin-supported FG arches, and

$$\tilde{w}_{f,linear} = A_{f1}(A_{f2} + A_{f3}) \tag{3.22}$$

where

$$A_{f1} = \frac{qR}{K_a[R^2(\varphi\cos(\varphi)\sin(\varphi) + \varphi^2 + 2\sin^2(\varphi)) + r_e^{\,2}\varphi(\cos(\varphi)\sin(\varphi) + \varphi)]} \tag{3.23}$$

$$A_{f2} = (R^2 + r_e^{\,2})(\cos(\theta)\sin(\varphi)\theta\varphi - \sin(\theta)\cos(\varphi)\varphi^2) \tag{3.24}$$

$$A_{f3} = 2R^2\sin(\varphi)(\sin(\varphi)\theta - \sin(\theta)\varphi) \tag{3.25}$$

and

$$\tilde{v}_{f,linear} = A_{f1}\varphi(R^2 + r_e^2)(B_{f1} + B_{f2}) \tag{3.26}$$

where

$$B_{f1} = \varphi - \cos(\theta)\cos(\varphi)\varphi - \sin(\theta)\sin(\varphi)\theta \tag{3.27}$$

$$B_{f2} = \sin(\varphi)(\cos(\varphi) - \cos(\theta)) \tag{3.28}$$

for fix-supported FG arches.

For pin-supported FG arches, subsuming Eq. (3.13) and Eq. (3.18) into Eq. (3.6) and Eq. (3.7), the linear elastic solution of compressive force N and the bending moment M can be obtained as:

$$N_{p,linear} = qR\left[1 - \frac{2qRr_e^2\cos(\theta)\sin(\varphi)}{K_a A_{p1}}\right] \tag{3.29}$$

$$M_{p,linear} = \frac{2(qRr_e)^2\sin(\varphi)[\cos(\theta) - \cos(\varphi)]}{K_a A_{p1}} \tag{3.30}$$

For fix-supported FG arches, subsuming Eq. (3.22) and Eq. (3.26) into Eq. (3.6) and Eq. (3.7), the linear elastic solution of compressive force N and the bending moment M can be obtained as:

$$N_{f,linear} = qR\left[1 - \frac{2qR\varphi r_e^2\cos(\theta)\sin(\varphi)}{K_a A_{f1}}\right] \tag{3.31}$$

$$M_{f,linear} = \frac{2(qr_e)^2R^3\sin(\varphi)[\varphi\cos(\theta) - \sin(\varphi)]}{K_a A_{f1}} \tag{3.32}$$

3.3 Nonlinear analysis in static response

Researches shown the axial deformation of shallow arch has an insignificant influence on the radial deformation (Pi Y.-L et al., 1998; 2002; 2007), thus it is neglected in the nonlinear elastic strain equation. The nonlinear elastic strain equation is obtained as (Simitses G.J., 1976):

$$\varepsilon = \frac{\partial \widetilde{w}}{\partial \theta} - \widetilde{v} + \frac{1}{2}\left(\frac{\partial \widetilde{v}}{\partial \theta}\right)^2 - \frac{y}{R}\left(\frac{\partial^2 \widetilde{v}}{\partial \theta^2}\right) \tag{3.33}$$

By substituting Eq. (3.33) into Eq. (3.3) the equilibrium equation of potential energy considering the geometric nonlinearity can be obtained as:

$$\delta\Pi = \int_{-\varphi}^{\varphi} - NR\left(\delta\frac{\partial \widetilde{w}}{\partial \theta} - \delta\widetilde{v} + \frac{\partial \widetilde{v}}{\partial \theta}\delta\frac{\partial \widetilde{v}}{\partial \theta}\right) - M\delta\frac{\partial^2 \widetilde{v}}{\partial \theta^2} - qR^2\delta\widetilde{v}\,\mathrm{d}\theta = 0 \tag{3.34}$$

where N and M are compressive axial force and bending moment of the arch given in Eq. (3.35) and Eq. (3.36):

$$N = \int_A - \sigma \mathrm{d}A = -\int_A E_{(Z,k)}\varepsilon_m \mathrm{d}A = -\left[\frac{\partial \widetilde{w}}{\partial \theta} - \widetilde{v} + \frac{1}{2}\left(\frac{\partial \widetilde{v}}{\partial \theta}\right)^2\right]K_a \tag{3.35}$$

$$M = \int_A \sigma y \mathrm{d}A = \int_A E_{(Z,k)}\varepsilon_b y \mathrm{d}A = -\frac{1}{R}\left(\frac{\partial^2 \widetilde{v}}{\partial \theta^2}\right)K_b \tag{3.36}$$

Substituting Eq. (3.35) and Eq. (3.36) into Eq. (3.5) and performing the calculus of variations leads to equilibrium equations in the radial direction and the axial direction given by Eq. (3.37) and Eq. (3.38):

$$\frac{\partial N}{\partial \theta} = 0 \tag{3.37}$$

$$-\frac{\partial^2 M}{\partial \theta^2} + NR\frac{\partial^2 \widetilde{v}}{\partial \theta^2} + NR - qR^2 = 0 \tag{3.38}$$

and rearranging Eq. (3.38) by substituting Eq. (3.36) leads to:

$$\frac{\partial^4 \widetilde{v}}{\partial \theta^4}\frac{K_b}{NR^2} + \frac{\partial^2 \widetilde{v}}{\partial \theta^2} - \frac{qR - N}{N} = 0 \tag{3.39}$$

For pin-supported arches, the radial displacements, the axial displacements and the bending moment are zero at the support at both ends. By applying these boundary conditions, the dimensionless displacements $\tilde{w}$ and $\tilde{v}$ can be obtained by solving differential equations Eq. (3.37) and Eq. (3.39):

$$\begin{aligned}\tilde{w}_p = &\frac{qR-N_p}{6N_p}\left(2-\frac{qR}{N_p}\right)\left(\theta^3-\theta\varphi^2\right)+\frac{(qR-N_p)^2K_b\theta}{N_p^3R^2}\left(1-\frac{C_\theta}{C_\varphi}\right)\\ &+\frac{q(qR-N_p)K_b^{1.5}}{N_p^{3.5}R^2\varphi}\frac{S_\theta\varphi-S_\varphi\theta}{C_\varphi}+\frac{(qR-N_p)^2K_b^{1.5}}{4N_p^{3.5}R^3\varphi}\frac{S_\theta C_\theta\varphi-S_\varphi C_\varphi\theta}{C_\varphi^2}\end{aligned} \tag{3.40}$$

$$\tilde{v}_p = \frac{(qR-N_p)K_b}{N_p^2R^2}\left(\frac{C_\theta}{C_\varphi}-1\right)+\frac{qR-N_p}{2N_p}\left(\theta^2-\varphi^2\right) \tag{3.41}$$

for the pin-supported FG arches and

$$\begin{aligned}\tilde{w}_f = &\frac{(qR-N_f)^2\sqrt{K_b}}{N_f^{2.5}R}\left(\frac{\varphi^2S_\theta C_\theta}{S_\varphi^2}+\frac{3C_\varphi}{4}-C_\theta\right)\\ &+\frac{q}{N_f^2}\left(\frac{1}{N_f}-\frac{1}{R}\right)\left(\frac{\varphi S_\theta K_b^2}{S_\varphi R^2N_f}-\theta K_b\right)+\frac{(qR-N_f)\theta}{6N_f}\left(1-\frac{qR-N_f}{N_f}\right)\left(\theta^2-\varphi^2\right)\end{aligned} \tag{3.42}$$

$$\tilde{v}_f = \frac{(qR-N_f)}{N_f^2}\left[\frac{\varphi(C_\theta-C_\varphi)}{S_\varphi R}\sqrt{N_fK_b}+\frac{N_f}{2}\left(\theta^2-\varphi^2\right)\right] \tag{3.43}$$

for the fix-supported FG arches, where:

$$\begin{aligned}&S_\theta=\sin\left(R\theta\sqrt{\frac{N}{K_b}}\right),\ S_\varphi=\sin\left(R\varphi\sqrt{\frac{N}{K_b}}\right)\\ &C_\theta=\cos\left(R\theta\sqrt{\frac{N}{K_b}}\right),\ C_\varphi=\cos\left(R\varphi\sqrt{\frac{N}{K_b}}\right)\end{aligned} \tag{3.44}$$

By substituting Eq. (3.41) into Eq. (3.36), the nonlinear equation of bending moment can be obtained as:

$$M_p = \frac{(qR - N_p)K_b}{N_p R}\left(\frac{C_\theta}{C_\varphi} - 1\right) \tag{3.45}$$

for the pin-supported arches and

$$M_f = (qR - N_f)\left[\sqrt{\frac{K_b}{N_f}}\frac{C_\theta \varphi}{S_\varphi} - \frac{K_b}{N_f R}\right] \tag{3.46}$$

for the fix-supported arches.

Eq. (3.37) implies the axial force is constant through arch, which can be expressed as:

$$N = \frac{1}{2\varphi}\int_{-\varphi}^{\varphi} N \mathrm{d}\theta \tag{3.47}$$

Substituting Eq. (3.35) and Eq. (3.41) into Eq. (3.46), and considering the displacements at the support are constant, the following equilibrium equation can be obtained:

$$D_{p1}\frac{(qR - N_p)^2}{N_p^2} + D_{p2}\frac{qR - N_p}{N_p} + D_{p3} = 0 \tag{3.48}$$

where

$$D_{p1} = \frac{5K_b}{4\varphi^2 N_p R^2}\left[\frac{S_\varphi^2}{5C_\varphi^2} - \frac{S_\varphi}{C_\varphi \varphi R}\sqrt{\frac{K_b}{N_p}} + 1\right] + \frac{1}{6} \tag{3.49}$$

$$D_{p2} = \frac{K_b}{\varphi^2 N_p R^2} - \frac{S_\varphi K_b^{1,5}}{C_\varphi N_p^{1.5} R^3 \varphi^3} + \frac{1}{3} \tag{3.50}$$

$$D_{p3} = \frac{r_e^2 N_p}{K_b \varphi^2} \tag{3.51}$$

for the pin-supported FG arches and

$$D_{f1}\frac{(qR-N_f)^2}{N_f^2}+D_{f2}\frac{qR-N_f}{N_f}+D_{f3}=0 \tag{3.52}$$

where

$$D_{f1}=\frac{C_\varphi}{4\varphi RS_\varphi}\left(3\sqrt{\frac{K_b}{N_f}}+\frac{\varphi RC_\varphi}{S_\varphi}-\frac{4S_\varphi K_b}{\varphi RN_fC_\varphi}\right)+\frac{5}{12} \tag{3.53}$$

$$D_{f2}=\frac{K_b}{N_fR^2\varphi}\left(\frac{C_\varphi R\sqrt{N_f}}{S_\varphi\sqrt{K_b}}-1\right)+\frac{1}{3} \tag{3.54}$$

$$D_{f3}=\frac{N_fr_e^2}{\varphi^2K_b} \tag{3.55}$$

for fix-supported FG arches.

The axial force N_p and N_f considering the geometric nonlinearity can be obtained by solving Eq. (3.45). and Eq. (3.61) respectively.

3.4 In-plane stability analysis

The energy equation of the in-plane buckling can be obtained from the second variation of the total potential energy Eq. (3.5), where the buckling displacements are expressed as $\tilde{v}_b=\delta\tilde{v}$ and $\tilde{w}_b=\delta\tilde{w}$.

$$\delta^2\Pi=\int_{-\varphi}^{\varphi}\left(\varepsilon_{mb}^2+\varepsilon_m\frac{\partial\tilde{v}_b}{\partial\theta}+\frac{r_e^2}{R^2}\frac{\partial^2\tilde{v}}{\partial\theta^2}\right)\mathrm{d}\theta=0 \tag{3.56}$$

where

$$\varepsilon_{mb}^2=\varepsilon_{mb}\left(\frac{\partial\tilde{w}_b}{\partial\theta}-\frac{\partial\tilde{v}_b}{\partial\theta}+\frac{\partial\tilde{v}}{\partial\theta}\frac{\partial\tilde{v}_b}{\partial\theta}\right) \tag{3.57}$$

Considering the axial buckling displacement, $\frac{\partial \varepsilon_{mb}}{\partial \theta} = 0$ can be obtained which implies that ε_{mb} is constant in the axial direction. The following differential equation can be obtained by re-arranging Eq. (3.56)

$$\frac{\partial^4 \tilde{v}_b}{\partial \theta^4}\frac{K_b}{NR^2} + \frac{\partial^2 \tilde{v}_b}{\partial \theta^2} - \frac{\varepsilon_{mb} K_b}{N r_e^2}\left(1 + \frac{\partial^2 \tilde{v}}{\partial \theta^2}\right) = 0 \tag{3.58}$$

and the average membrane strain during buckling ε_{mb} can be obtained as

$$\varepsilon_{mb} = \frac{1}{2\varphi}\int_{-\varphi}^{\varphi} \varepsilon_{mb} \mathrm{d}\theta = \frac{1}{2\varphi}\int_{-\varphi}^{\varphi}\left(\frac{\partial \tilde{w}_b}{\partial \theta} - \frac{\partial \tilde{v}_b}{\partial \theta} + \frac{\partial \tilde{v}}{\partial \theta}\frac{\partial \tilde{v}_b}{\partial \theta}\right)\mathrm{d}\theta \tag{3.59}$$

Substituting Eq. (3.41) into Eq. (3.58) and apply the pin-supported support boundary conditions in Eq. (3.60):

$$\tilde{v}_b = \frac{\partial^2 \tilde{v}_b}{\partial \theta^2} = 0 \text{ at } \theta = \pm\varphi \tag{3.60}$$

leads

$$\tilde{v}_b = \frac{\varepsilon_{mb} K_a^2 \left(qR - N\right)}{N^2 R}\left(D_{pvb1} + D_{pvb2} + D_{pvb3}\right) \tag{3.61}$$

where

$$\begin{aligned} D_{pvb1} &= \left(\theta^2 - \varphi^2\right) R \\ D_{pvb2} &= \frac{\left(C_\varphi S_\theta \theta - C_\theta S_\varphi \varphi\right)}{2\sqrt{N}} \\ D_{pvb3} &= \frac{K_b}{(qR - N)R}\left(\frac{2qR}{N} - 1\right)\left(\frac{C_\theta}{C_\varphi} - 1\right) \end{aligned} \tag{3.62}$$

By substitute Eq. (3.61) into Eq. (3.58) and Eq. (3.59), the equilibrium equation under the snap-through symmetric buckling scenario for a pin-supported FG arch can be obtained as:

$$D_{psb1}\frac{(qR-N_p)^2}{N_p^2}+D_{psb2}\frac{qR-N_p}{N_p}+D_{psb3}=0 \tag{3.63}$$

where

$$\begin{aligned} D_{psb1} &= \frac{8N_p^{1.5}R^3\varphi^3C_\varphi^3}{K_b^{1.5}}-\frac{6N_pR^2\varphi^2S_\varphi}{K_b}+C_\varphi\left[\frac{R\sqrt{N_p}}{\sqrt{K_b}}\varphi\left(72C_\varphi^2+33\right)-105C_\varphi S_\varphi\right] \\ D_{psb2} &= \frac{64C_\varphi^3\varphi^3R^3N_p^2}{K_b^{1.5}}+\frac{96C_\varphi^3\varphi R\sqrt{N_p}}{\sqrt{K_b}}+C_\varphi\left(\frac{24\varphi R\sqrt{N_p}}{K_b}-120C_\varphi S_\varphi\right) \\ D_{psb3} &= \frac{24N_p^{2.5}R^5C_\varphi^3\varphi}{\left(K_b\right)^{2.5}}\left[1+\frac{K_b\varphi^2}{3N_pR^2}-\frac{N_pR^2}{r_e}\right] \end{aligned} \tag{3.64}$$

Solving Eq. (3.48) and Eq. (3.63) simultaneously, the symmetric snap-through buckling load $q = q_{sb}$ for pin-supported FG arches can be obtained.

Moreover, substituting Eq. (3.43) into Eq. (3.58), and then apply the boundary conditions stated in Eq. (3.65)

$$\tilde{v}_b = \frac{\partial \tilde{v}_b}{\partial \theta} = 0 \quad \text{at } \theta = \pm\varphi \tag{3.65}$$

leads

$$\tilde{v}_b = \frac{-\varepsilon_{mb}K_a}{2NS_\varphi^2}\left(D_{fvb1}+D_{fvb2}+D_{fvb3}\right) \tag{3.66}$$

where

$$D_{fvb1}=\left(1-\frac{C_\varphi^2 qR^2}{N}\right)\left(\theta^2-\varphi^2\right)$$

$$D_{fvb2}=\frac{S_\varphi \varphi\sqrt{K_b}(3qR-N)}{N^{1.5}R}(C_\theta-C_\varphi) \quad (3.67)$$

$$D_{fvb3}=\varphi qR\left(\theta\left(S_\theta S_\varphi+\frac{\theta}{\varphi}\right)+\varphi\left(C_\theta C_\varphi-2\right)\right)$$

By substituting Eq. (3.66) into Eq. (3.59), the equilibrium equation under the snap-through symmetric buckling scenario for a fix-supported FG arch can be obtained as:

$$D_{fsb1}\frac{(qR-N_f)^2}{N_f^2}+D_{fsb2}\frac{qR-N_f}{N_f}+D_{fsb3}=0 \quad (3.68)$$

where

$$D_{fsb1}=\frac{C_\varphi}{4S_\varphi^2}\left[\left(R\sqrt{\frac{N}{K_b}}\frac{6S_\varphi}{\varphi}+\frac{\varphi}{S_\varphi}\right)+5C_\varphi^2\right]-\frac{3K_b}{\varphi^2 NR^2}+\frac{4}{3}$$

$$D_{fsb2}=\frac{4K_b}{\varphi^2R^2N}+\frac{3C_\varphi\sqrt{K_b}}{S_\varphi\varphi\sqrt{N}R}+\frac{\sqrt{K_b}}{S_\varphi^2R\sqrt{N}}+\frac{2}{3} \quad (3.69)$$

$$D_{fsb3}=\frac{C_\varphi\sqrt{K_b}}{\varphi S_\varphi R\sqrt{N}}-\frac{1}{\varphi^2}\left(\frac{K_b}{NR^2}+\frac{N}{K_a}\right)+\frac{1}{3}$$

Solving Eq. (3.52) and Eq. (3.68) simultaneously, the symmetric snap-through buckling load $q=q_{sb}$ for fix-supported FG arches can be obtained.

When the arch has initial imperfections or under perturbations, it may buckle in the anti-symmetric mode. In this case, the membrane strain $\varepsilon_{mb}=0$, substitute it into Eq. (3.58) leads to

$$\frac{\partial^4\tilde{v}_b}{\partial\theta^4}\frac{K_b}{NR^2}+\frac{\partial^2\tilde{v}_b}{\partial\theta^2}=0 \quad (3.70)$$

For pin-supported arches, solving Eq. (3.70) by apply the boundary conditions stated in Eq. (3.60) leads to

$$\sin\left(R\varphi\sqrt{\frac{N_p}{K_b}}\right)=0 \tag{3.71}$$

and the fundamental solution for Eq. (3.71) can be obtain as

$$R\varphi\sqrt{\frac{N_p}{K_b}}=\pi \tag{3.72}$$

then

$$N_p = N_{pcr} = \frac{\pi^2 K_b}{R^2\varphi^2} \tag{3.73}$$

Substituting Eq. (3.73) into Eq. (3.48), the anti-symmetric buckling load for pin-supported FG arches q_{bb} can be solved.

For fix-supported arches, solving Eq. (3.70) by applying the boundary conditions stated in Eq. (3.65) leads to

$$\tan\left(R\varphi\sqrt{\frac{N_f}{K_b}}\right)=R\varphi\sqrt{\frac{N_f}{K_b}} \tag{3. 74}$$

and the lowest value to satisfy Eq. (3.74) can be obtain as

$$R\varphi\sqrt{\frac{N_f}{K_b}}\approx 1.4303\pi \tag{3. 75}$$

$$N_f = N_{fcr} = \frac{(1.4303\pi)^2 K_b}{R^2\varphi^2} \tag{3. 76}$$

By substituting Eq. (3.76) into Eq. (3.52), the anti-symmetric buckling load for fix-ended FG arches q_{bb} can be solved.3.5

Result validation and numerical examples

In order to validate the proposed method, numerical verifications were performed in ANSYS by adopting BEAM188 elements. As the variation of the material properties cannot be modelled in the finite element as the current stage, the cross-section is discretised into 200 layers in its radial direction to simulate the various of materials as illustrated in Figure 3.2; 360 elements are used along the span of the arch. Four case studies are demonstrated in this session. Following computer configurations are used in the numerical simulation:

System: Microsoft Windows 7

CPU: Intel Core i7-6700 3.4 GHz

RAM: 16.0 GB

First two examples present static responses with the numerical verifications. In the first example, a pin-supported FG arch under radial uniform distributed load is investigated by adopting the derived equations. The following parameters are adopted: E_o = 390 GPa, E_i = 210 GPa, r = 200 mm, L = 12 m, f/L = 1/12 and applied uniform distributed load q = 3905.2 kN/m. The results of this example are illustrated in Figures 3.3 to 3.6, which include the radial central displacement (v_c, $\theta = 0$), axial displacement at quarter point ($w_{q,}$, $\theta = 0.5\varphi$), central compressive axial force (N_c, $\theta = 0$) and central bending moment(M_c, $\theta = 0$) by various power-law exponent k from 0 to 5, respectively. The numerical verification of fix-supported FG arch is illustrated in the Figures 3.7 to 3.10.

The following parameters are adopted: E_o = 390 GPa, E_i = 210 GPa, r = 200 mm, L = 12 m, f/L = 1/12 and applied uniform distributed load q = 2662.7 kN/m. Results show the proposed analytical solution agrees well to the ANSYS's prediction. In Figure 3.6 and Figure 3.10, it can be observed that the linear elastic analysis predicts a very small decrement in axial forces while the nonlinear analysis demonstrates a significant increasing. Moreover, the result shows the nonlinear static responses of the FG shallow circular arch are more significant that the linear analysis.

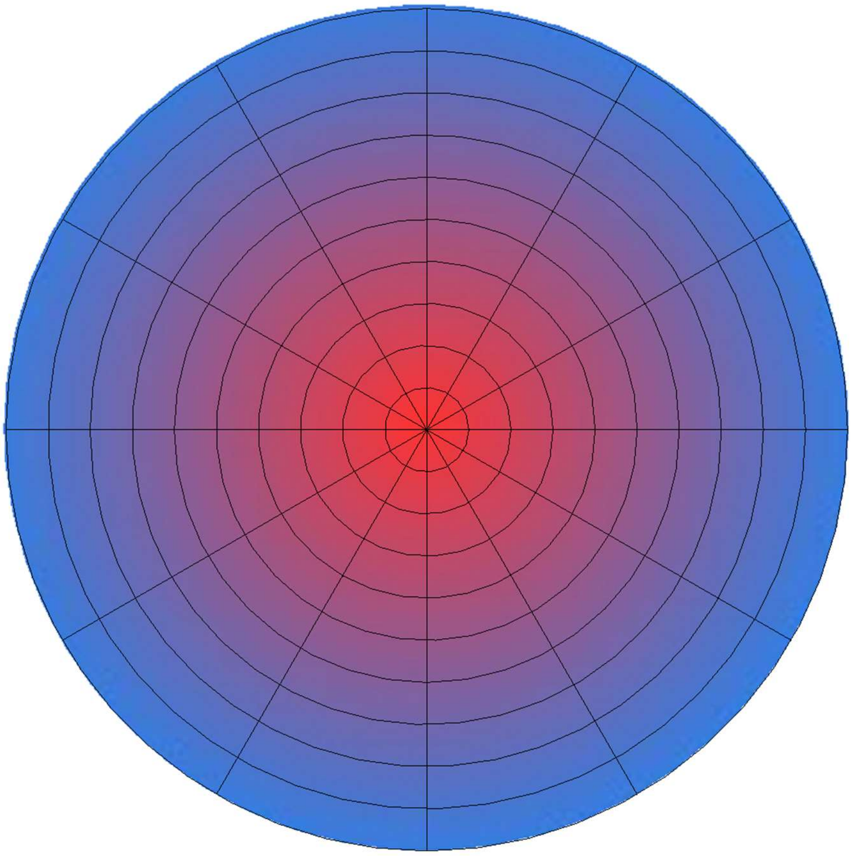

Figure 3.2 Illustration of cross-section of FEA model

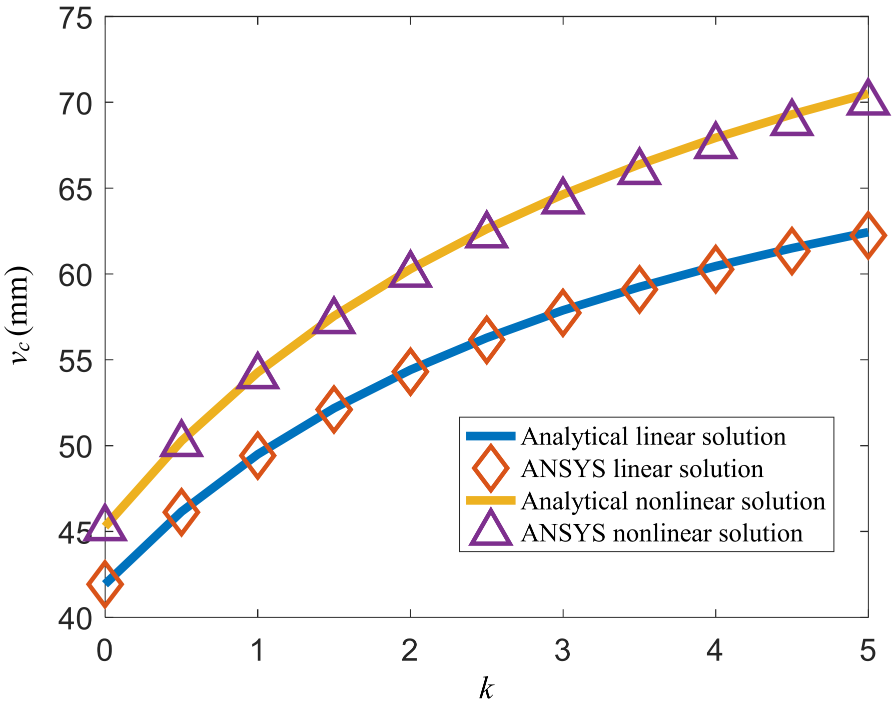

Figure 3.3 Radial central displacement v_c of pin-supported FG arches

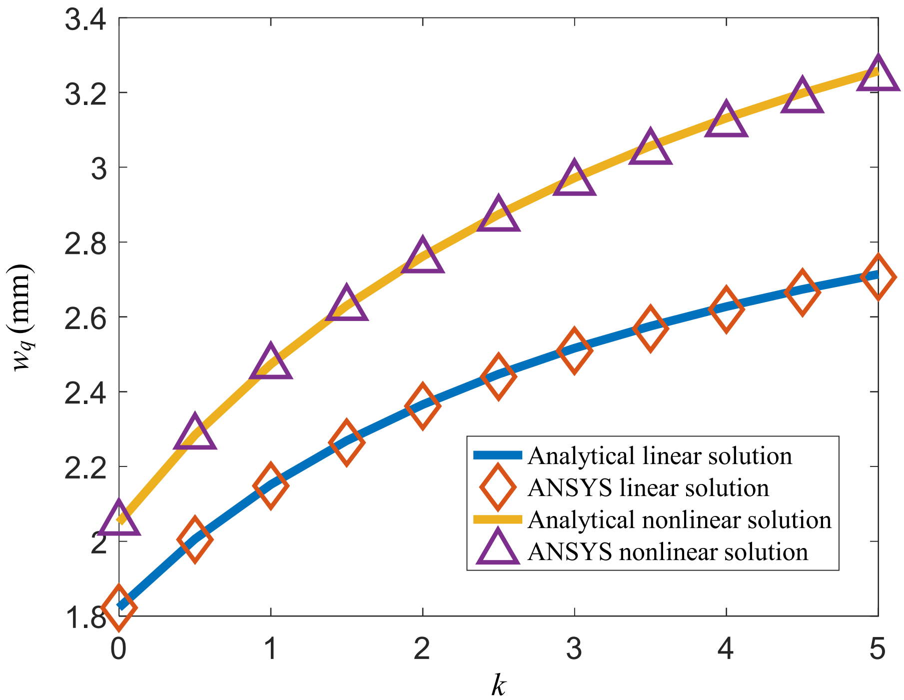

Figure 3.4 Axial displacement at quarter point w_q of pin-supported FG arches

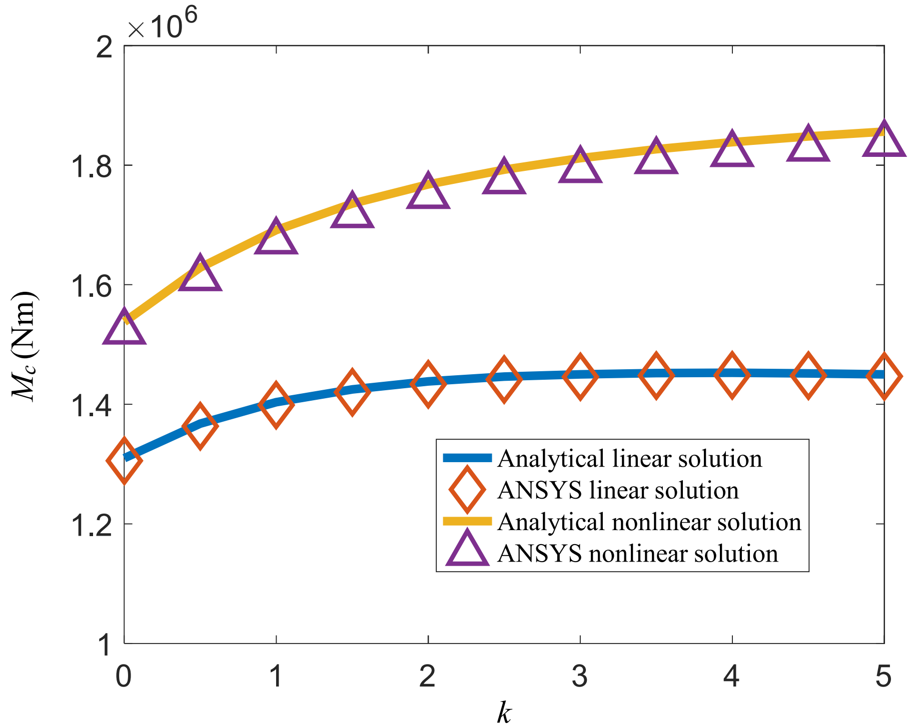

Figure 3.5 Central moment M_c of pin-supported FG arches

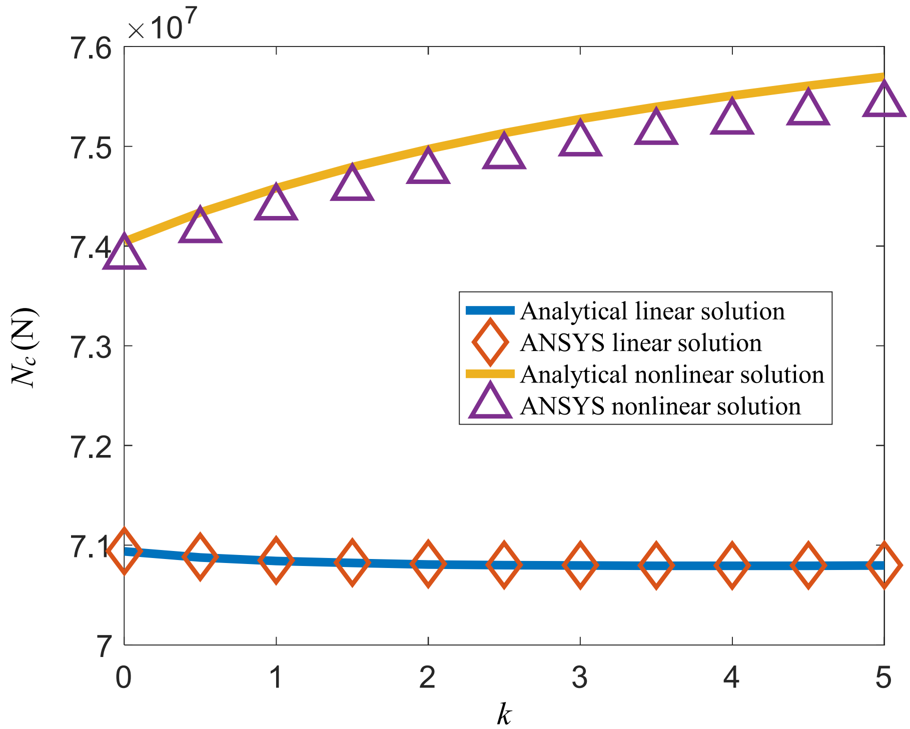

Figure 3.6 Central axial force N_c of pin-supported FG arches

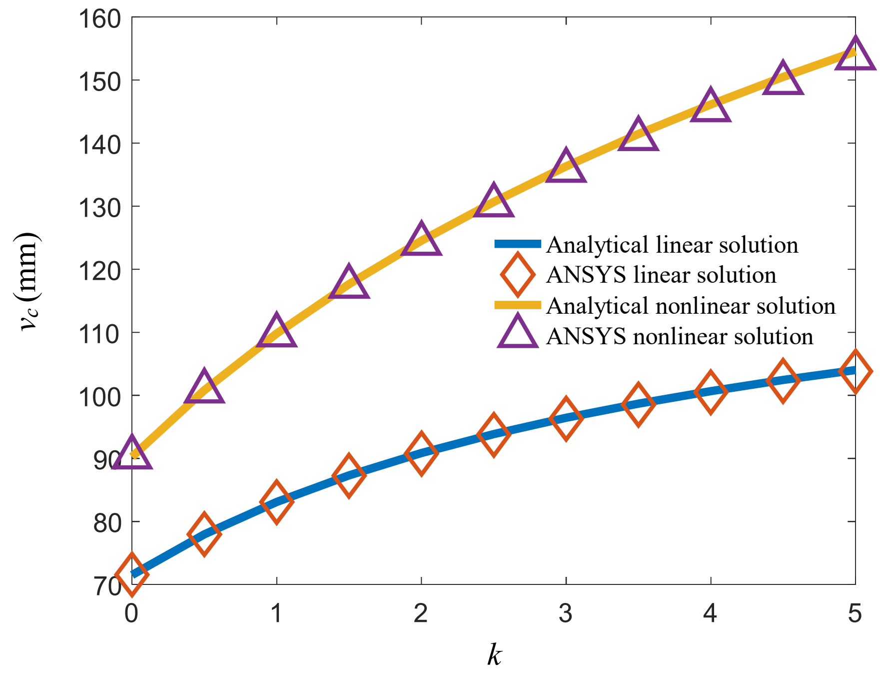

Figure 3.7 Radial central displacement v_c of fix-supported FG arches

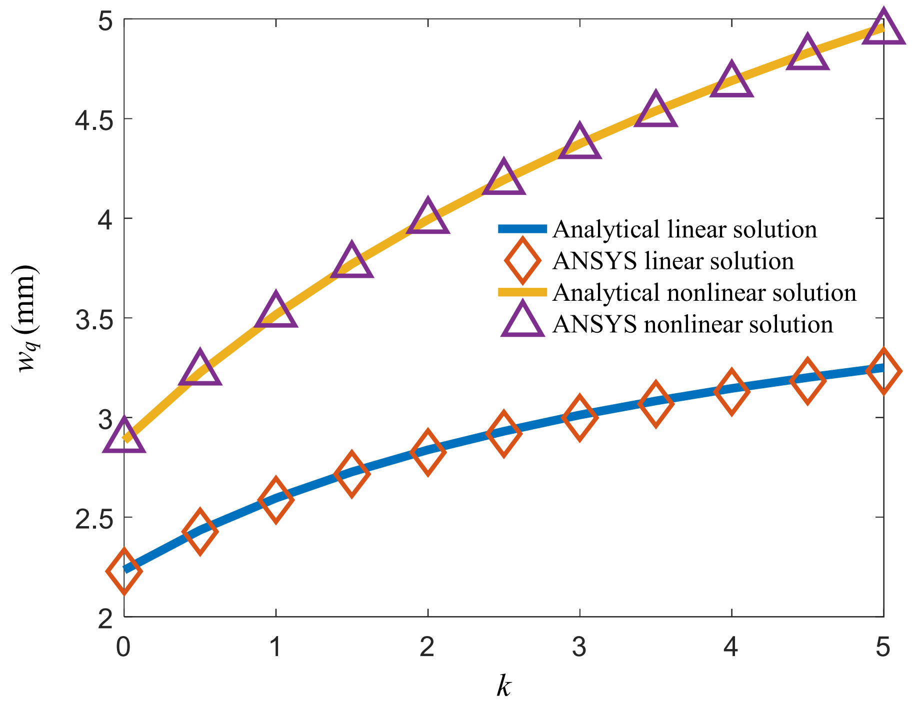

Figure 3.8 Axial displacement at quarter point w_q of fix-supported FG arches

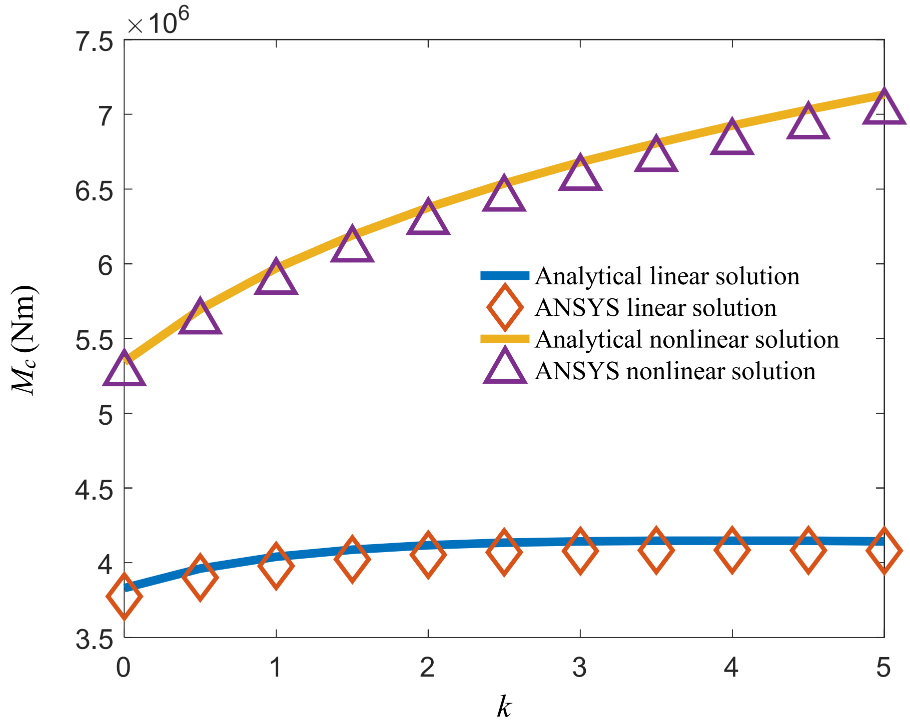

Figure 3.9 Central moment M_c of fix-supported FG arches

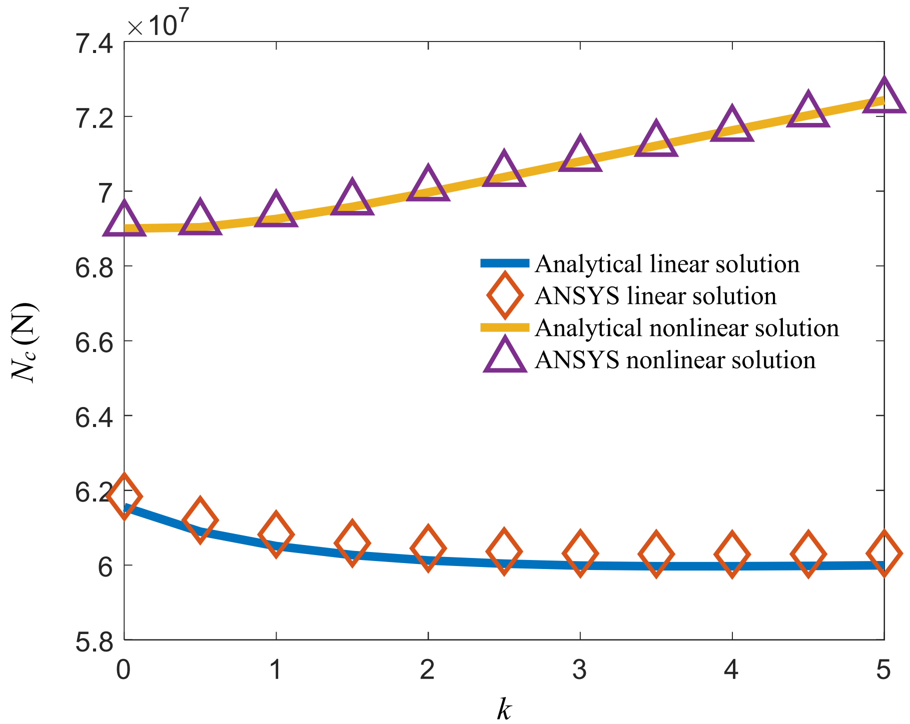

Figure 3.10 Central axial force N_c fix-supported FG arches

Figures 3.11 and 3.14 present FG arches under the snap-through symmetric bucking and anti-symmetric buckling mode respectively. Results show the buckling load of the

FG arches decrease rapidly when the exponential factor k is between 0 and 10 and the decreasing rate reduces significantly when the k factor is greater than 10. As illustrated, the proposed analytical solution agrees well to the ANSYS's prediction. However, the computational time consumption of the ANSYS prediction is very expensive. It took more than 10 hours in the limit point buckling analysis and more than 40 hours for arches with initial imperfection per calculation point. By adopting the proposed analytical equations, the computational efficiency can be increased dramatically, by coding in MatLab 2017, the computational time can be reduced to within 5 seconds per calculation point, which is thousands of times faster than the ANSYS prediction.

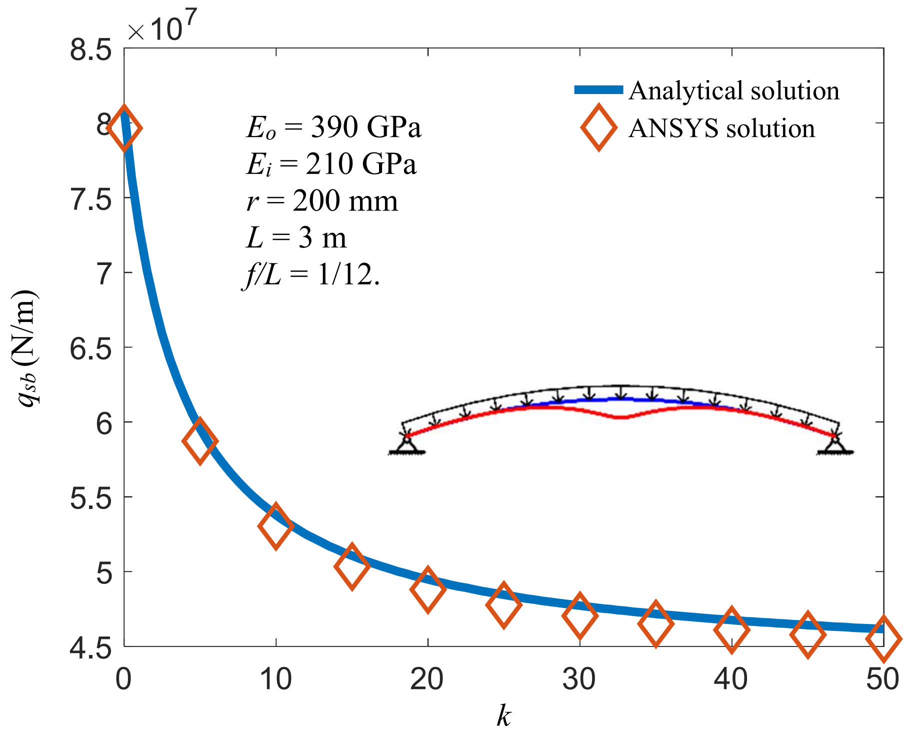

Figure 3.11 Limit point buckling load q_{sb} of pin-supported FG arches

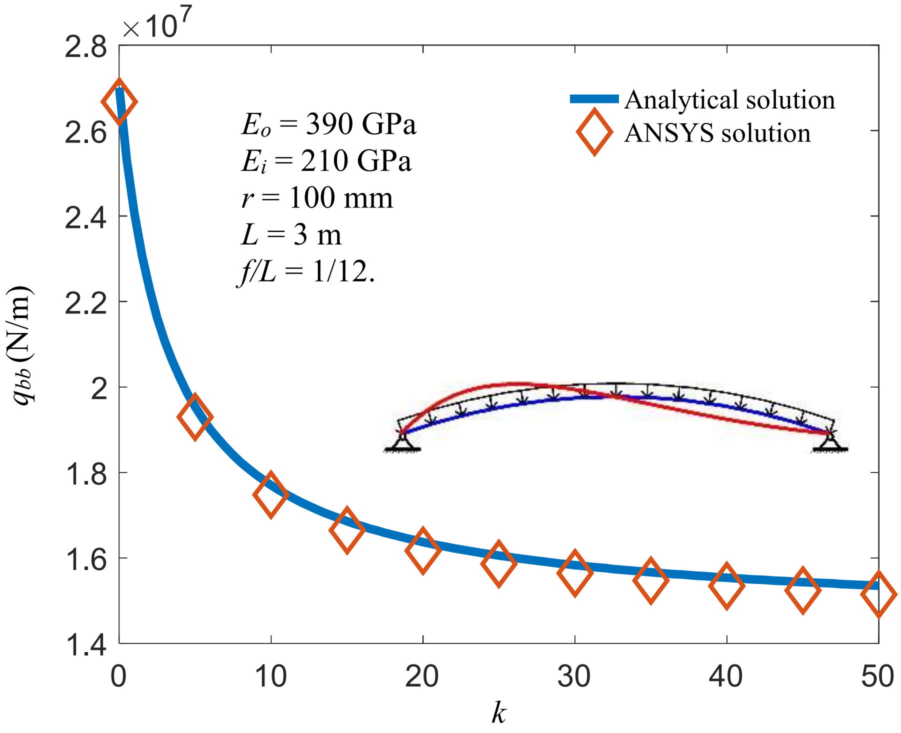

Figure 3.12 Bifurcation buckling load q_{bb} of pin-supported FG arches

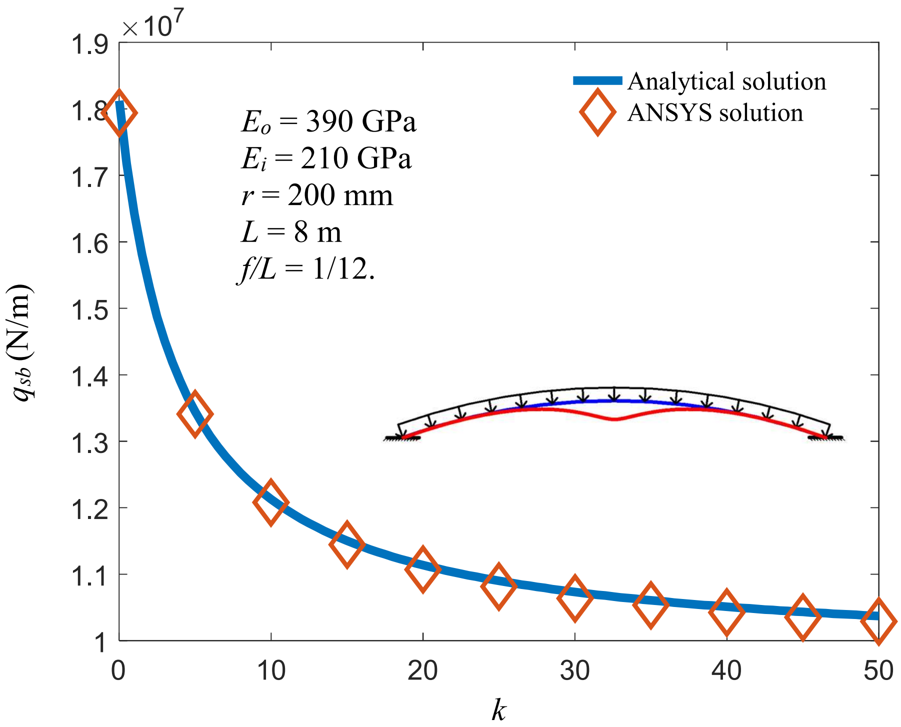

Figure 3.13 Limit point buckling load q_{sb} of fix-supported FG arches

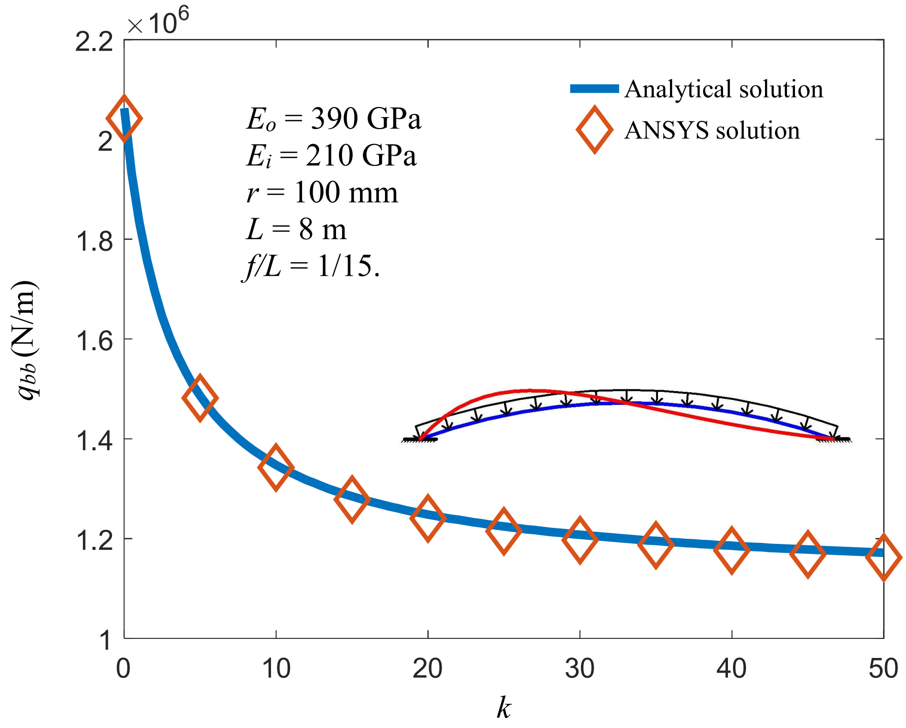

Figure 3.14 Bifurcation buckling load q_{bb} of fix-supported FG arches

3.6 Conclusion

In this chapter, the static responses and stability analysis of FGM circular shallow arch under radial uniform load are investigated. Particularly, analytical solution of linear elastic responses, geometric nonlinear elastic responses, symmetric limit point buckling and anti-symmetric bifurcation buckling are derived. In order to verify the accuracy of proposed approaches, results are compared with those produced by commercial software ANSYS 18.1. Results show the proposed method agreed well to the solution from ANSYS 18.1 while has a dramatic computational efficiency. Following phenomenon were observed from the numerical investigation:

- the static response of the FG circular shallow arches against radial uniform distributed load is rather nonlinear;

- the deformations and internal forces are increasing with the increment of power-law exponent *k*;
- the buckling load can be decreased by adopting higher *k* for the power-law of the FG material.

The proposed method can be used as benchmarks for the further numerical investigations of the FGM arches. Furthermore, the enhanced calculation efficiency can contribute to the further design optimisation or reliability analysis of FGM arches when numerous calculations are required.

Chapter 4

Static response and in-plane stability of FG porous arches with graphene platelets reinforcements

4.1 Introduction

This chapter presents an analytical approach for nonlinear static responses and stability analysis of functionally graded porous (FGP) arches with graphene platelets (GPLs) reinforcements (i.e., FGP-GPLRC arches). The constitutive material composition of the FGP-GPLRC arch varies along the radial direction of the cross section specifically, so that the mechanical performance of the arch such as buckling strength and weight can be well controlled for various engineering design purposes. The effective Young's modulus of the FGP-GPLRC arch is determined by the volume fraction distribution of materials. Based on the Euler-Bernoulli hypothesis, the structural responses of the arch considering the geometric nonlinearity are derived by using the virtual work method. Two boundary conditions are considered which are including the pinned-pinned and the fixed-fixed supports. The loading condition is defined as uniformly distributed load in the radial direction of the arch. Different buckling modes are discussed by the illustration of the equilibrium paths. By adopting the developed analytical solution, the relationship between the structural response, buckling load, self-weight, porosity level and the percentage of content of the GPLs can be investigated efficiently. The applicability and effectiveness of the proposed analytical approach for the geometric nonlinear analysis of FGP-GPLRC arch structures are demonstrated through numerical examples.

4.2 Static stability analysis of FGP-GPLRC arches

A circular FGP-GPLRC arch is considered as shown in Figure 4.1. The porosity of the material varies continuously along the radial direction in the cross section. Figure 4.2 and Figure 4.3 demonstrate the two considered porosity distributions with GPLs reinforcement and, Z is the radial axis in the cross section, r is the radius of the cross section, E_{max} and E_{min} denote the maximum and the minimum elastic modulus of porous material shown in the diagram respectively.

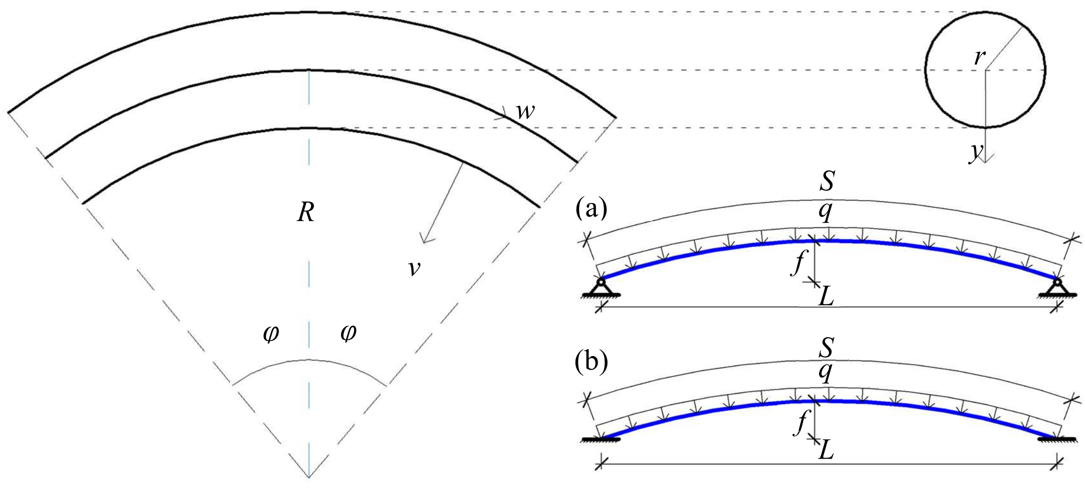

Figure 4.1 Shallow arch under uniformly distributed load with support condition: (a) pinned support, (b) fixed support

4.2.1 The porosity distributions and GPLs reinforcement

Following the dramatic improvement of modern manufacturing technology, the manufacture of porous materials can be customised according to engineers' design specifications. Conceivably, many different porous materials with various porosity distributions can be manufactured to fulfil the engineering demands (Chen, Yang, & Kitipornchai, 2015). For example, various types of aluminium foam were manufactured and then their mechanical properties were tested in (Hangai Y. et al. 2013).

In this study, the material composition of the FGP-GPLRC arch is assumed to be varied in the radial direction of the cross-section. According to the well-established literatures (Magnucki K. & Stasiewica P., 2004; Magnucka-Blandzi E., 2008; 2010; Jabbari M., Mojahedin A, Khorshidvandb A. & Eslami M., 2014), two non-uniform FG pore distributions are adopted herein, which can be explicitly formulated as:

$$\gamma_{(Z)} = \begin{cases} \cos\left(\dfrac{\pi\left(2t-r\right)}{2r}\right) & \text{Porosity Distribution 1} \\ \cos\left(\dfrac{\pi t}{2r}\right) & \text{Porosity Distribution 2} \end{cases} \tag{4.1}$$

$$\begin{cases} E_{(Z)} = E_1[1-e_0\gamma_{(Z)}] \\ \rho_{(Z)} = \rho_1[1-e_m\gamma_{(Z)}] \end{cases} \tag{4.1}$$

where e_0 denotes the porosity coefficient which is defined as

$$e_0 = 1 - \frac{E_{\min}}{E_{\max}} \tag{4.2}$$

The effects of the two adopted porosity distributions on the overall Young's modulus of a structural member are illustrated in Figure 4.2 and Figure 4.3.

Under the Gaussian random field scheme, the mechanical properties of the closed-cell cellular solids can be expressed as (Song et al., 2017)

$$\frac{E_{(Z)}}{E_1} = \left(\frac{1.121 - e_m \gamma_{(Z)}}{1.121} \right)^{2.3} \tag{4.3}$$

which leads to the expression of the mass coefficient e_m

$$e_m = \frac{1.121\left(1 - \sqrt[2.3]{1.121 - e_0 \gamma_{(Z)}}\right)}{\gamma_{(Z)}} \tag{4.4}$$

Research shows that the Halpin-Tsai micromechanics model has a good prediction in the Young's modules of the non-porous nanocomposite structures which was extended to the estimation of the nano-composite reinforced porous materials (Kitipornchai, Chen, & Yang, 2017; Yang, Wu, & Kitipornchai, 2017; Rafiee et al., 2009). That is.

$$E_1 = \frac{3}{8}\left(\frac{1 + \xi_L^{GPL} \eta_L^{GPL} V_{GPL}}{1 - \eta_L^{GPL} V_{GPL}} \right) E_M + \frac{5}{8}\left(\frac{1 + \xi_W^{GPL} \eta_W^{GPL} V_{GPL}}{1 - \eta_W^{GPL} V_{GPL}} \right) E_M \tag{4.5}$$

where

$$\begin{aligned} \xi_L^{GPL} &= \frac{2 l_{GPL}}{t_{GPL}} \\ \xi_W^{GPL} &= \frac{2 w_{GPL}}{t_{GPL}} \\ \eta_L^{GPL} &= \frac{E_{GPL} - E_M}{E_{GPL} - E_M \xi_L^{GPL}} \\ \eta_W^{GPL} &= \frac{E_{GPL} - E_M}{E_{GPL} - E_M \xi_W^{GPL}} \end{aligned} \tag{4.6}$$

$$V_{GPL} = \frac{\rho_M \Lambda_{GPL}}{\rho_M \Lambda_{GPL} + \rho_{GPL}\left(1 - \Lambda_{GPL}\right)} \tag{4.7}$$

and

$$\rho_1 = \rho_{GPL} V_{GPL} + \rho_M V_M \tag{4.8}$$

where Λ_{GPL} denotes the weight fraction of the GPLs reinforcement in percentage unit; l_{GPL} , w_{GPL} , and t_{GPL} are the length, width and thickness of the graphene platelets respectively.

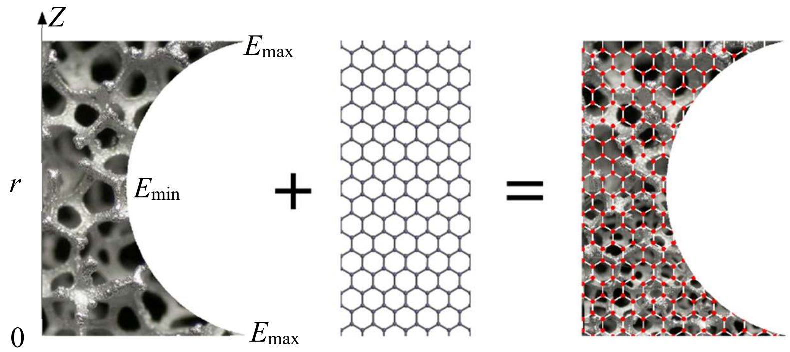

Figure 4.2 Porosity distribution 1 and GPLs reinforcement

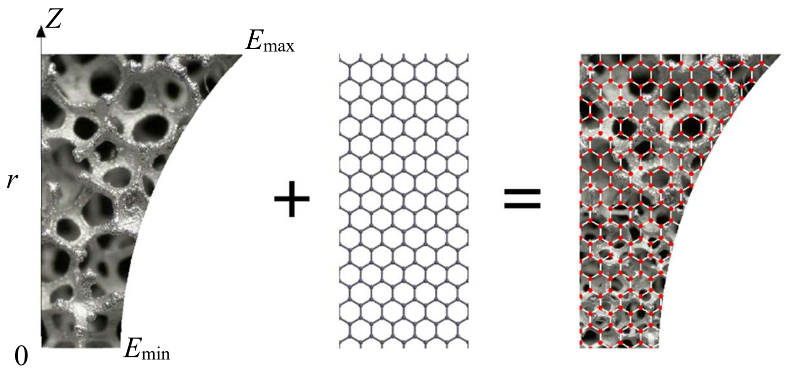

Figure 4.3 Porosity distribution 2 and GPLs reinforcement

4.2.2 Nonlinear responses and internal actions

Based on the Euler-Bernoulli hypothesis, the strain at an arbitrary point at the centroid line of the arch is the sum of the membrane strain ε_m and bending strain ε_b while the shear strains are neglected. Researches shown that the axial deformation of the shallow arch has an insignificant influence on the radial deformation (Pi, Bradford, & Uy, 2002; Pi, & Trahair, 1998), thus it is neglected in the nonlinear elastic strain equation. The nonlinear elastic strain equation is obtained from (Pi, & Trahair, 1998) as:

$$\varepsilon = \frac{\partial \tilde{w}}{\partial \theta} - \tilde{v} + \frac{1}{2}\left(\frac{\partial \tilde{v}}{\partial \theta}\right)^2 - \frac{y}{R}\left(\frac{\partial^2 \tilde{v}}{\partial \theta^2}\right) \tag{4.9}$$

where $\tilde{w}$ and $\tilde{v}$ denote the dimensionless axial and radial displacements, i.e. $\tilde{w} = w/R$ and $\tilde{v} = v/R$.

While the arch is sustaining the uniform distributed load q and at equilibrium, the virtual potential energy vanishes:

$$\delta\Pi = \int_V \sigma\delta\varepsilon \mathrm{d}V - \int_{-\varphi}^{\varphi} qR^2 \delta\tilde{v} \mathrm{d}\theta = 0 \tag{4.10}$$

By substituting Eq. (4.10) into Eq. (4.11), the nonlinear equilibrium equation of the potential energy can be obtained as:

$$\delta\Pi = \int_{-\varphi}^{\varphi} -NR\left(\delta\frac{\partial \tilde{w}}{\partial \theta} - \delta\tilde{v} + \frac{\partial \tilde{v}}{\partial \theta}\delta\frac{\partial \tilde{v}}{\partial \theta}\right) - M\delta\frac{\partial^2 \tilde{v}}{\partial \theta^2} - qR^2\delta\tilde{v}\mathrm{d}\theta = 0 \tag{4.11}$$

where N and M are compressive axial force and bending moment of the arch given in Eq. (4.13) and Eq. (4.14):

$$N = \int_A -\sigma \mathrm{d}A = -\int_A E_{(Z)}\varepsilon_m \mathrm{d}A = -\left[\frac{\partial \tilde{w}}{\partial \theta} - \tilde{v} + \frac{1}{2}\left(\frac{\partial \tilde{v}}{\partial \theta}\right)^2\right] K_a \tag{4.12}$$

$$M = \int_A \sigma y \mathrm{d}A = \int_A E_{(Z)}\varepsilon_b y \mathrm{d}A = -\frac{1}{R}\left(\frac{\partial^2 \tilde{v}}{\partial \theta^2}\right) K_b \tag{4.13}$$

where K_a and K_b are the axial stiffness and the bending stiffness given by Eq. (4.15) and Eq. (4.16):

$$K_a = 2\pi \int_0^r E_{(Z)} Z \mathrm{d}Z \tag{4.14}$$

$$K_b = \pi \int_0^r E_{(Z)} Z^3 \mathrm{d}Z \tag{4.15}$$

and r_e is the effective radius of gyration defined by Eq. (4.17):

$$r_e = \sqrt{\frac{K_b}{K_a}} \tag{4.16}$$

Substituting Eq. (4.13) and Eq. (4.14) into Eq. (4.12) and then apply the calculus of variations to the resultant formulation leads to the equilibrium equations in the radial direction and the axial direction given by Eq. (4.17) and Eq. (4.18):

$$\frac{\partial N}{\partial \theta} = 0 \tag{4.17}$$

$$-\frac{\partial^2 M}{\partial \theta^2} + NR\frac{\partial^2 \tilde{v}}{\partial \theta^2} + NR - qR^2 = 0 \tag{4.18}$$

Moreover, the substitution of Eq. (4.13) into Eq. (4.18) leads to:

$$\frac{\partial^4 \tilde{v}}{\partial \theta^4}\frac{K_b}{NR^2} + \frac{\partial^2 \tilde{v}}{\partial \theta^2} - \frac{qR - N}{N} = 0 \tag{4.19}$$

The boundary conditions for pin-supported arches are

$$\tilde{v} = 0 \text{ and } \tilde{w} = 0 \text{ at } \theta = \pm\varphi \tag{4.20}$$

and the boundary conditions for fix-supported arches are

$$\tilde{v} = 0 \text{ and } \frac{\partial \tilde{v}}{\partial \theta} = 0 \text{ at } \theta = \pm\varphi \tag{4.21}$$

By applying the boundary conditions in Eq. (4.20) for the pin-supported and Eq. (4.21) for the fix-supported arches, the dimensionless displacements $\tilde{w}$ and $\tilde{v}$ for pin-supported arches can be obtained by solving the differential equations formulated by Eq. (4.22) and Eq. (4.23) accordingly:

$$\begin{aligned}\tilde{w}_p =& \frac{qR - N_p}{6N_p}\left(2 - \frac{qR}{N_p}\right)\left(\theta^3 - \theta\varphi^2\right) + \frac{(qR - N_p)^2 K_b}{N_p^3 R^2}\left(1 - \frac{C_\theta}{C_\varphi}\right)\\ &+ \frac{q(qR - N_p)K_b^{1.5}}{N_p^{3.5} R^2 \varphi}\frac{S_\theta \varphi - S_\varphi \theta}{C_\varphi} + \frac{(qR - N_p)^2 K_b^{1.5}}{4N_p^{3.5} R^3 \varphi}\frac{S_\theta C_\theta \varphi - S_\varphi C_\varphi \theta}{C_\varphi^2}\end{aligned} \tag{4.22}$$

$$\tilde{v}_p = \frac{(qR - N_p)K_b}{N_p^2 R^2}\left(\frac{C_\theta}{C_\varphi} - 1\right) + \frac{qR - N_p}{2N_p}\left(\theta^2 - \varphi^2\right) \tag{4.23}$$

The dimensionless displacements $\tilde{w}$ and $\tilde{v}$ for the fix-supported arches can be obtained by solving the differential equations presented in Eq. (4.23) and Eq. (4.24):

$$\tilde{w}_f = \frac{(qR-N_f)\theta}{6N_f}\left(1-\frac{qR-N_f}{N_f}\right)\left(\theta^2-\varphi^2\right)+\frac{\varphi^2 S_\theta C_\theta (qR-N_f)^2\sqrt{K_b}}{N_f^{2.5}RS_\varphi^2}$$
$$+\frac{q}{N_f^2}\left(\frac{1}{N_f}-\frac{1}{R}\right)\left(\frac{\varphi S_\theta K_b^2}{S_\varphi R^2 N_f}-\theta K_b\right)+\frac{(qR-N_f)^2\sqrt{K_b}}{N_f^{2.5}R}\left(\frac{3C_\varphi}{4}-C_\theta\right) \tag{4.24}$$

$$\tilde{v}_f = \frac{(qR-N_f)\varphi C_\varphi\sqrt{K_b}}{S_\varphi N_f^{1.5}R}+\frac{qR-N_f}{2N_f}\left(\theta^2-\varphi^2-\varphi\frac{2C_\varphi\sqrt{K_b}}{RS_\varphi\sqrt{N_f}}\right) \tag{4.25}$$

where

$$S_\theta = \sin\left(R\theta\sqrt{\frac{N}{K_b}}\right),\ S_\varphi = \sin\left(R\varphi\sqrt{\frac{N}{K_b}}\right)$$
$$C_\theta = \cos\left(R\theta\sqrt{\frac{N}{K_b}}\right),\ C_\varphi = \cos\left(R\varphi\sqrt{\frac{N}{K_b}}\right) \tag{4.26}$$

By substituting Eq. (4.22) and Eq. (4.24) into Eq. (4.12), the nonlinear equation of bending moment can be obtained as:

$$M_p = \frac{(qR-N_p)K_b}{N_p R}\left(\frac{C_\theta}{C_\varphi}-1\right) \tag{4.27}$$

for the pin-supported FGP-GPLRC arches and

$$M_f = \frac{(qR-N_f)K_b}{N_f}\left(\varphi\frac{C_\theta}{S_\varphi}\sqrt{\frac{N}{K_b}}-\frac{1}{R}\right) \tag{4.28}$$

for the fix-supported FGP-GPLRC arches.

Eq. (4.17) implies the axial force is constant through the arch, which can be expressed as:

$$N = \frac{1}{2\varphi}\int_{-\varphi}^{\varphi} N \mathrm{d}\theta \tag{4.29}$$

For pin-supported arches, substituting Eq. (4.12) and Eq. (4.20) into Eq. (4.27); and for fix-supported arches, substituting Eq. (4.12) and Eq. (4.21) into Eq. (4.27) with consideration of the axial displacements at the end-supports are zero, the following equilibrium equations can be obtained for pin-supported arches in Eq. (4.30):

$$D_{p1}\frac{(qR - N_p)^2}{N_p^2} + D_{p2}\frac{qR - N_p}{N_p} + D_{p3} = 0 \tag{4.30}$$

where

$$D_{p1} = \frac{5K_b}{4\varphi^2 N_p R^2}\left[\frac{S_\varphi^2}{5C_\varphi^2} - \frac{S_\varphi}{C_\varphi \varphi R}\sqrt{\frac{K_b}{N_p}} + 1\right] + \frac{1}{6} \tag{4.31}$$

$$D_{p2} = \frac{\pi K_b}{\varphi^2 N_p R^2} - \frac{S_\varphi K_b^{1.5}}{C_\varphi N_p^{1.5} R^3 \varphi^3} + \frac{1}{3} \tag{4.32}$$

$$D_{p3} = \frac{N_p r_e^2}{K_b \varphi^2} \tag{4.33}$$

and fix-supported arches in Eq. (4.34):

$$D_{f1}\frac{(qR-N_f)^2}{N_f^2}+D_{f2}\frac{qR-N_f}{N_f}+D_{f3}=0 \tag{4.34}$$

where

$$D_{f1}=\frac{3C_\varphi\sqrt{K_b}}{4\varphi RS_\varphi\sqrt{N_f}}+\frac{C_\varphi^2}{4S_\varphi^2}-\frac{K_b}{\varphi^2R^2N_f}+\frac{5}{12} \tag{4.35}$$

$$D_{f2}=\frac{C_\varphi\sqrt{K_b}}{S_\varphi\varphi\sqrt{N_f}R}-\frac{K_b}{N_fR^2\varphi}+\frac{1}{3} \tag{4.36}$$

$$D_{f3}=\frac{N_fr_e^2}{\varphi^2K_b} \tag{4.37}$$

The axial force N_p of the pin-supported arch and N_f of the fix-supported arch with the consideration of geometric nonlinearity can be obtained by solving Eq. (4.30) and Eq. (4.34) respectively.

4.2.3 Buckling analysis

The energy equation of the in-plane buckling can be obtained from the second variation of the total potential energy Eq. (4.11), where the buckling displacement can be expressed as $\tilde{v}_b=\delta\tilde{v}$ and $\tilde{w}_b=\delta\tilde{w}$.

$$\delta^2\Pi=\int_{-\varphi}^{\varphi}\left(\varepsilon_{mb}^2+\varepsilon_m\frac{\partial\tilde{v}_b}{\partial\theta}+\frac{r_e^2}{R^2}\frac{\partial^2\tilde{v}}{\partial\theta^2}\right)\mathrm{d}\theta=0 \tag{4.38}$$

where

$$\varepsilon_{mb}^{2} = \varepsilon_{mb}\left(\frac{\partial \tilde{w}_b}{\partial \theta} - \frac{\partial \tilde{v}_b}{\partial \theta} + \frac{\partial \tilde{v}}{\partial \theta}\frac{\partial \tilde{v}_b}{\partial \theta}\right) \tag{4.39}$$

Considering the axial buckling displacement, $\frac{\partial \varepsilon_{mb}}{\partial \theta} = 0$ can be obtained which implies ε_{mb} is a constant in the axial direction. The following differential equation can be obtained by re-arranging Eq. (4.38)

$$\frac{\partial^4 \tilde{v}_b}{\partial \theta^4}\frac{K_b}{NR^2} + \frac{\partial^2 \tilde{v}_b}{\partial \theta^2} - \frac{\varepsilon_{mb} K_b}{N r_e^2}\left(1 + \frac{\partial^2 \tilde{v}}{\partial \theta^2}\right) = 0 \tag{4.40}$$

and the average membrane strain during buckling can be obtained as

$$\varepsilon_{mb} = \frac{1}{2\varphi}\int_{-\varphi}^{\varphi} \varepsilon_{mb} \mathrm{d}\theta = \frac{1}{2\varphi}\int_{-\varphi}^{\varphi}\left(\frac{\partial \tilde{w}_b}{\partial \theta} - \frac{\partial \tilde{v}_b}{\partial \theta} + \frac{\partial \tilde{v}}{\partial \theta}\frac{\partial \tilde{v}_b}{\partial \theta}\right)\mathrm{d}\theta \tag{4.41}$$

For pin-supported arches, substituting Eq. (4.23) into Eq. (4.40) and then apply the boundary conditions presented in Eq. (4.42)

$$\tilde{v}_b = \frac{\partial^2 \tilde{v}_b}{\partial \theta^2} = 0 \quad \text{at } \theta = \pm\varphi \tag{4.42}$$

leads

$$\tilde{v}_b = \frac{\varepsilon_{mb} K_a^2 K_b}{(NR)^2}\left(D_{pvb1} + D_{pvb2} + D_{pvb3}\right) \tag{4.43}$$

where

$$D_{pvb1}=\frac{\left(qR-N\right)R^2}{K_b}\left(\theta^2-\varphi^2\right) \tag{4.44}$$

$$D_{pvb2}=\frac{\left(qR-N\right)R}{2\sqrt{N}K_b}\left(C_\varphi S_\theta \theta-C_\theta S_\varphi \varphi\right) \tag{4.45}$$

$$D_{pvb3}=\left(\frac{2qR}{N}-1\right)\left(\frac{C_\theta}{C_\varphi}-1\right) \tag{4.46}$$

By substituting Eq. (4.43) into Eq. (4.41), the equilibrium equation under the snap-through symmetric buckling scenario for a pin-supported FGP-GPLRC arch can be obtained as:

$$D_{psb1}\frac{(qR-N_p)^2}{N_p^2}+D_{psb2}\frac{qR-N_p}{N_p}+D_{psb3}=0 \tag{4.47}$$

where

$$\begin{aligned}D_{psb1}=&\frac{2NR^2\varphi^2}{K_b}\left(\frac{4RC_\varphi^3\varphi\sqrt{N}}{\sqrt{K_b}}-3S_\varphi\right)\\&+\frac{R\sqrt{N}}{\sqrt{K_b}}C_\varphi\varphi\left(72C_\varphi^2+33\right)-105C_\varphi^2 S_\varphi\end{aligned} \tag{4.48}$$

$$D_{psb2}=\frac{16C_\varphi^3\varphi R\sqrt{N}}{\sqrt{K_b}}\left(\frac{4NR^2\varphi^2\sqrt{N}}{K_b}+6\right)+\frac{24\varphi RC_\varphi\sqrt{N}}{K_b}-120C_\varphi^2 S_\varphi \tag{4.49}$$

$$D_{psb3} = \frac{8N^{1.5}R^3C_\varphi^3\varphi}{\left(K_b\right)^{2.5}}\left[3NR^2 + K_b\varphi^2 - \frac{3N^2R^4}{r_e}\right] \tag{4.50}$$

Solving Eqs. (4.30) and (4.47) simultaneously, the symmetric snap-through buckling load $q = q_{sb}$ for pin-supported FGP-GPLRC arches can be obtained.

Moreover, substituting Eq. (4.25) into Eq. (4.40), and then apply the boundary conditions stated in Eq. (4.51)

$$\tilde{v}_b = \frac{\partial \tilde{v}_b}{\partial \theta} = 0 \quad \text{at } \theta = \pm\varphi \tag{4.51}$$

leads

$$\tilde{v}_b = \frac{-\varepsilon_{mb}K_a\sqrt{K_b}}{2N^{1.5}RS_\varphi^2}\left(D_{fvb1} + D_{fvb2} + D_{fvb3}\right) \tag{4.52}$$

where

$$D_{fvb1} = \left(\frac{R\sqrt{N}}{\sqrt{K_b}} - \frac{C_\varphi^2 qR^2}{\sqrt{NK_b}}\right)\left(\theta^2 - \varphi^2\right) \tag{4.53}$$

$$D_{fvb2} = \frac{S_\varphi \varphi(3qR - N)}{N}(C_\theta - C_\varphi) \tag{4.54}$$

$$D_{fvb3} = \frac{\varphi qR^2\sqrt{N}}{\sqrt{K_b}}\left(\theta\left(S_\theta S_\varphi + \frac{\theta}{\varphi}\right) + \varphi\left(C_\theta C_\varphi - 2\right)\right) \tag{4.55}$$

By substituting Eq. (4.52) into Eq. (4.41), the equilibrium equation under the snap-through symmetric buckling scenario for a fix-supported FGP-GPLRC arch can be obtained as:

$$D_{fsb1}\frac{(qR-N_f)^2}{N_f^2}+D_{fsb2}\frac{qR-N_f}{N_f}+D_{fsb3}=0 \tag{4.56}$$

where

$$D_{fsb1}=\frac{4}{3}+\frac{C_\varphi R\sqrt{N}}{S_\varphi\sqrt{K_b}}\left(\frac{3}{2\varphi}+\frac{\varphi}{4S_\varphi^2}\right)+\frac{5C_\varphi^2}{4S_\varphi^2}-\frac{3K_b}{\varphi^2 NR^2} \tag{4.57}$$

$$D_{fsb2}=\frac{2}{3}+\frac{\sqrt{K_b}}{R\sqrt{N}}\left[\frac{1}{S_\varphi^2}+\frac{1}{\varphi}\left(\frac{3C_\varphi}{S_\varphi}-\frac{4\sqrt{K_b}}{\varphi R\sqrt{N}}\right)\right] \tag{4.58}$$

$$D_{fsb3}=\frac{1}{3}+\frac{C_\varphi\sqrt{K_b}}{\varphi S_\varphi R\sqrt{N}}-\frac{1}{\varphi^2}\left(\frac{K_b}{NR^2}+\frac{N}{K_a}\right) \tag{4.59}$$

By solving Eqs. (4.34) and (4.56) simultaneously, the symmetric snap-through buckling load $q=q_{sb}$ for fix-supported FGP-GPLRC arches can be obtained.

When the arch is buckled in the anti-symmetric mode, the membrane strain $\varepsilon_{mb}=0$, and the substitution of it into Eq. (4.40) leads

$$\frac{\partial^4\tilde{v}_b}{\partial\theta^4}\frac{K_b}{NR^2}+\frac{\partial^2\tilde{v}_b}{\partial\theta^2}=0 \tag{4.60}$$

For pin-supported arches, solving Eq. (4.60) by apply the boundary conditions stated in Eq. (4.42) leads to

$$\sin\left(R\varphi\sqrt{\frac{N_p}{K_b}} \right) = 0 \tag{4.61}$$

and the fundamental solution for Eq. (4.61) can be obtain as

$$R\varphi\sqrt{\frac{N_p}{K_b}} = \pi \tag{4.62}$$

then

$$N_p = N_{pcr} = \frac{\pi^2 K_b}{R^2 \varphi^2} \tag{4.63}$$

By substituting Eq. (4.63) into Eq. (4.30), the anti-symmetric buckling load for pin-ended FGP-GPLRC arches q_{bb} can be solved.

For fix-supported arches, solving Eq. (4.60) by applying the boundary conditions stated in Eq. (4.51) leads to

$$\tan\left(R\varphi\sqrt{\frac{N_f}{K_b}} \right) = R\varphi\sqrt{\frac{N_f}{K_b}} \tag{4.64}$$

and the lowest value to satisfy Eq. (4.64) can be obtain as

$$R\varphi\sqrt{\frac{N_f}{K_b}} \approx 1.4303\pi \tag{4.65}$$

$$N_f = N_{fcr} = \frac{(1.4303\pi)^2 K_b}{R^2\varphi^2} \tag{4.66}$$

By substituting Eq. (4.66) into Eq. (4.34), the anti-symmetric buckling load for fix-ended FGP-GPLRC arches q_{bb} can be solved.

4.3 Numerical investigation

In this section, the numerical verification and investigation are presented. Aluminium based metal matrix is adopted in the numerical study with the following material properties: E_M = 70 GPa, ρ_M = 2700 kg/m^3. The adopted properties of the graphene platelets are based on the previous researches (Kitipornchai, Chen, & Yang, 2017; Chen, Yang, & Kitipornchai, 2016b): E_{GPL}=1010 GPa, ρ_{GPL}=1062.5 kg/m^3, l_{GPL} =2.5 μm, w_{GPL} =1.5 μm, t_{GPL}=1.5 nm.

In order to validate the proposed method, geometric nonlinear analyses were performed by using the commercial finite element analysis software ANSYS 18.1 with the adoption of BEAM188 elements. To simulate the material variation, the cross section is subdivided into multiple layers in the radial direction. The material properties are assigned to each layer according to Eq. (3.2). From the convergence study, the variance of the results between 400 layers and 200 layers is less than 0.5%. Thus, 200 sub-layers are adopted in the numerical verification for efficient computation but without compromising the accuracy of the results. The proposed analytical approaches are coded by MATLAB 2016b. Following computer configurations are used in the numerical simulation: Microsoft Windows 7; Intel Core i7-6700 3.4 GHz; 16.0 GB RAM.

4.3.1 Result verifications of the nonlinear structural responses

In the nonlinear structural response analysis, the radial central displacement (v_c, $\theta = 0$), axial displacement at quarter point ($w_{q,}$, $\theta = 0.5\varphi$), central compressive axial force (N_c, $\theta = 0$) and central bending moment(M_c, $\theta = 0$) are verified with various GPLs weight fractions Λ_{GPL}. In Case 1, the nonlinear static response verification of a pin-supported aluminium based FGP-GPLRC arch is illustrated in Figure 4.4. In this example, the following geometry parameters are adopted: r = 25 mm, L = 2 m, f/L = 1/10, where r, L, f are the radius of the cross section, span length and fall of the arch illustrated in Figure 4.1. The applied uniform distributed load is $q = \frac{0.65 N_{pcr}}{R}$. The porosity coefficient e_0 = 0.3 and the porosity distribution 2 are adopted for this numerical verification. In Case 2, the nonlinear static response verification of a pin-supported aluminium based FGP-GPLRC arch is illustrated in Figure 4.5. The arch is under a uniform pressure $q = \frac{0.65 N_{fcr}}{R}$. The following geometry parameters are adopted in this study: r = 25 mm, L = 2 m, f/L = 1/10, e_0 = 0.4 with porosity distribution 1.

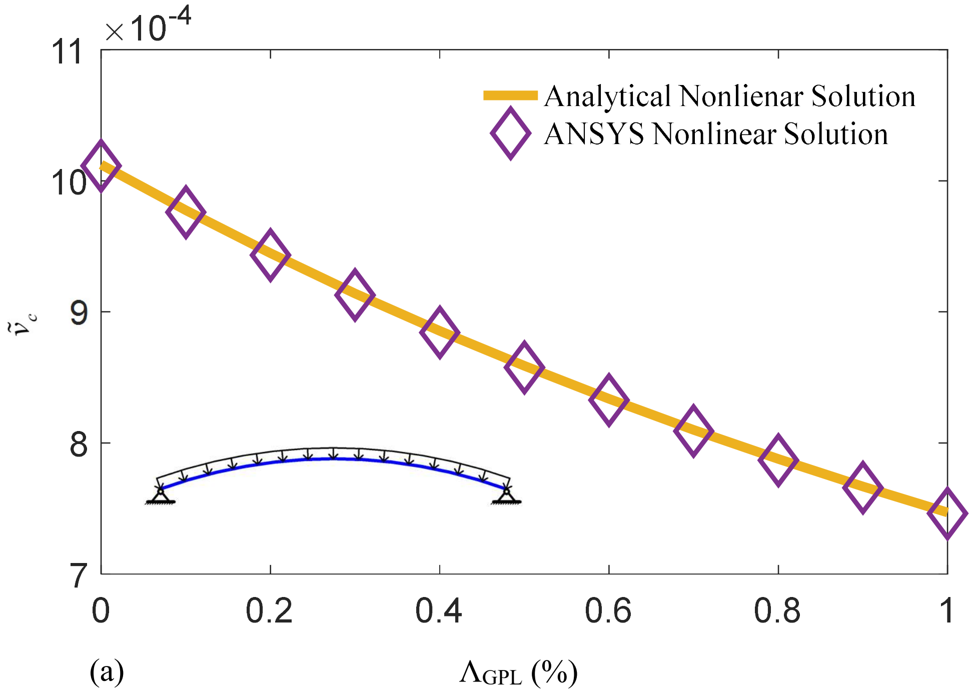

×10^-4
11
10
9
8
7
$\tilde{v}_c$
0
0.2
0.4
0.6
0.8
1
Analytical Nonlienar Solution
ANSYS Nonlinear Solution
(a)
Λ_{GPL} (%)

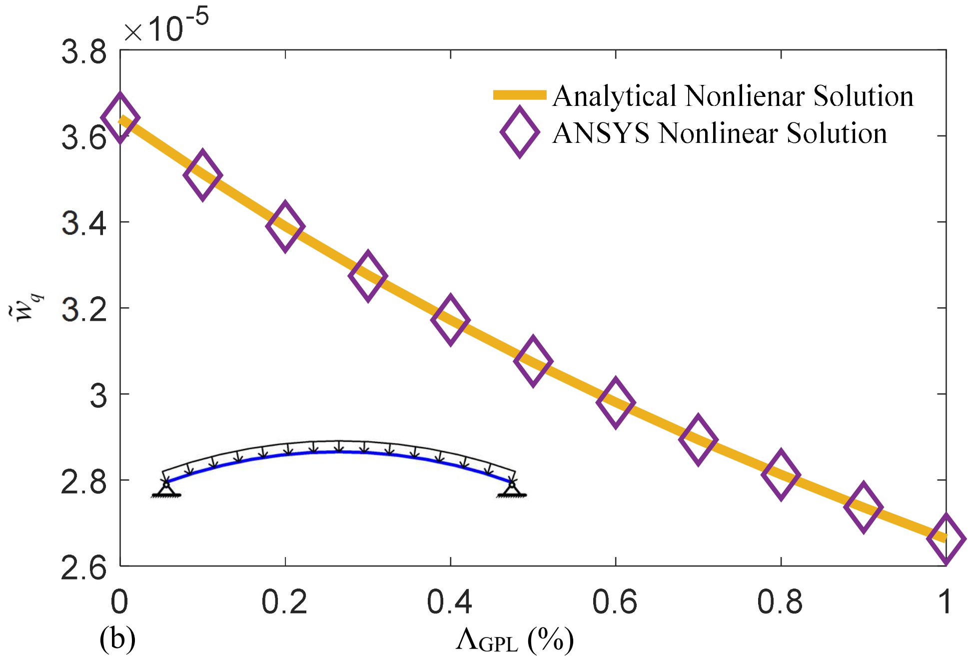

×10^-5
3.8
3.6
3.4
3.2
3
2.8
2.6
$\tilde{w}_q$
0
0.2
0.4
0.6
0.8
1
Analytical Nonlienar Solution
ANSYS Nonlinear Solution
(b)
Λ_{GPL} (%)

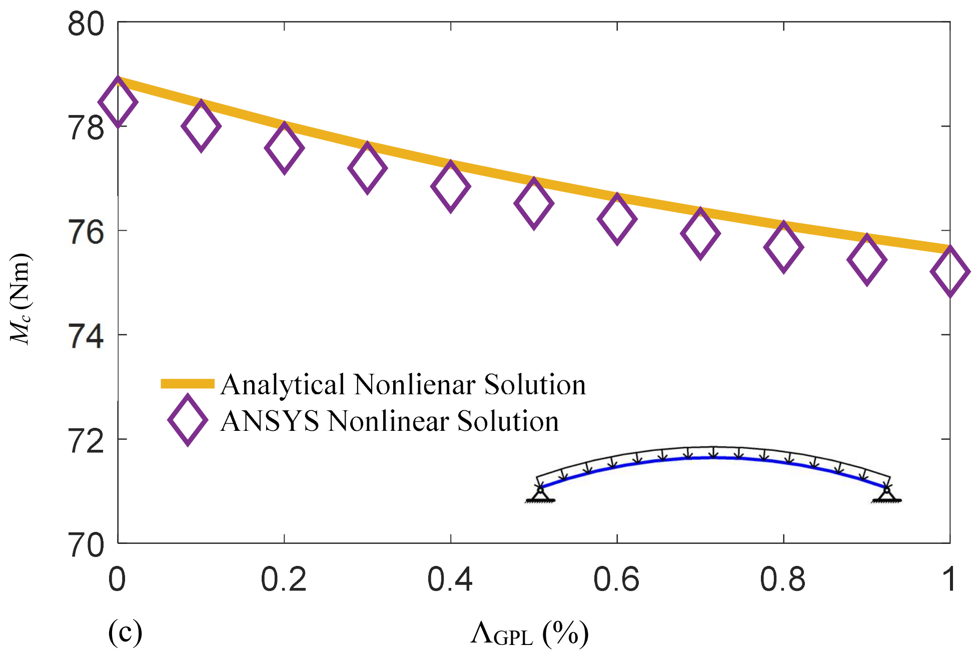

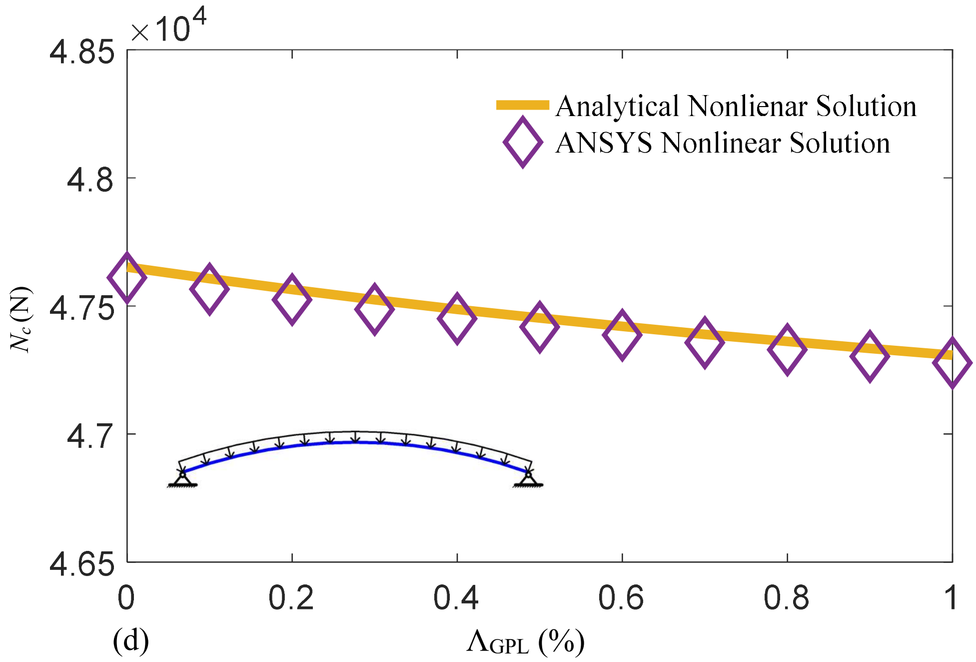

Figure 4.4 Results validation of (a) radial central displacement $\tilde{v}_c$; (b) axial displacement at quarter point $\tilde{w}_q$; (c) central moment M_c and (d) central axial force N_c for a pin-supported aluminium based FGP-GPLRC arch.

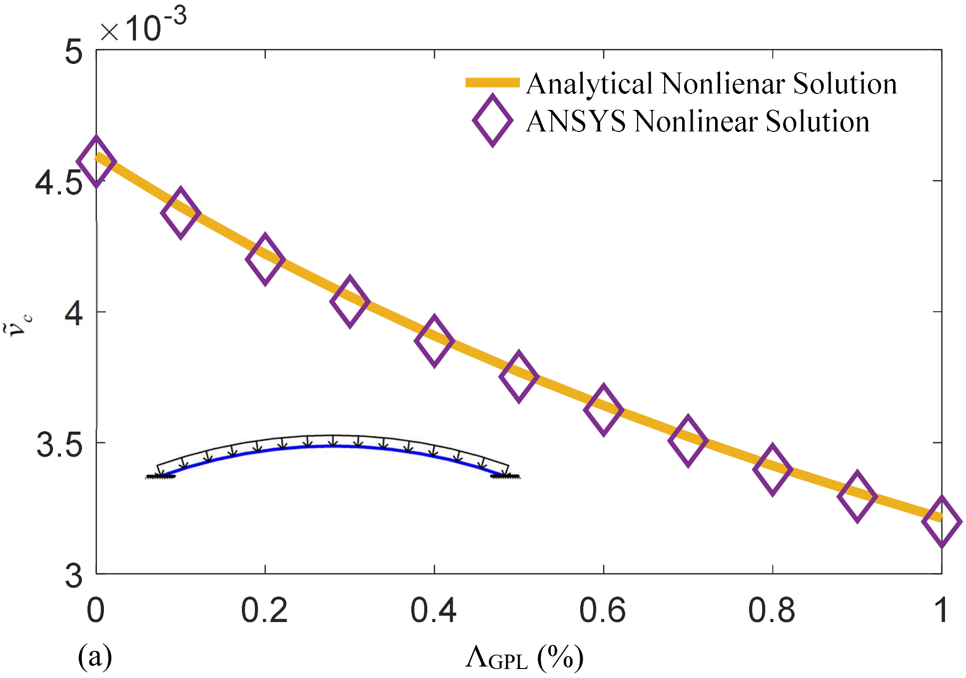

×10^-3
5
4.5
4
3.5
3
0
0.2
0.4
0.6
0.8
1
Analytical Nonlienar Solution
ANSYS Nonlinear Solution
$\tilde{v}_c$
ΛGPL (%)

(a)

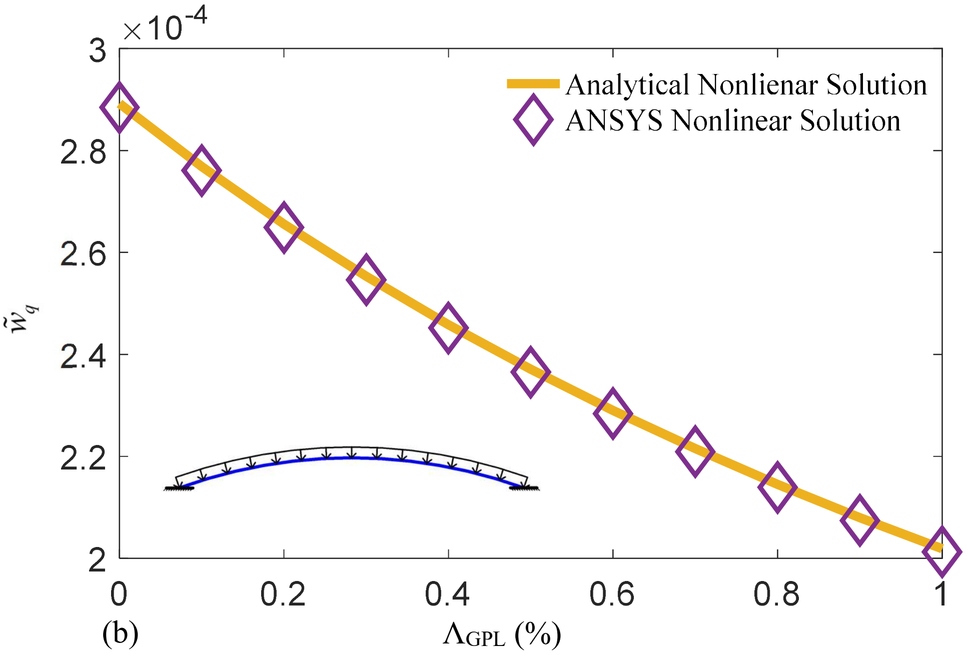

×10^-4
3
2.8
2.6
2.4
2.2
2
0
0.2
0.4
0.6
0.8
1
Analytical Nonlienar Solution
ANSYS Nonlinear Solution
$\tilde{w}_q$
ΛGPL (%)

(b)

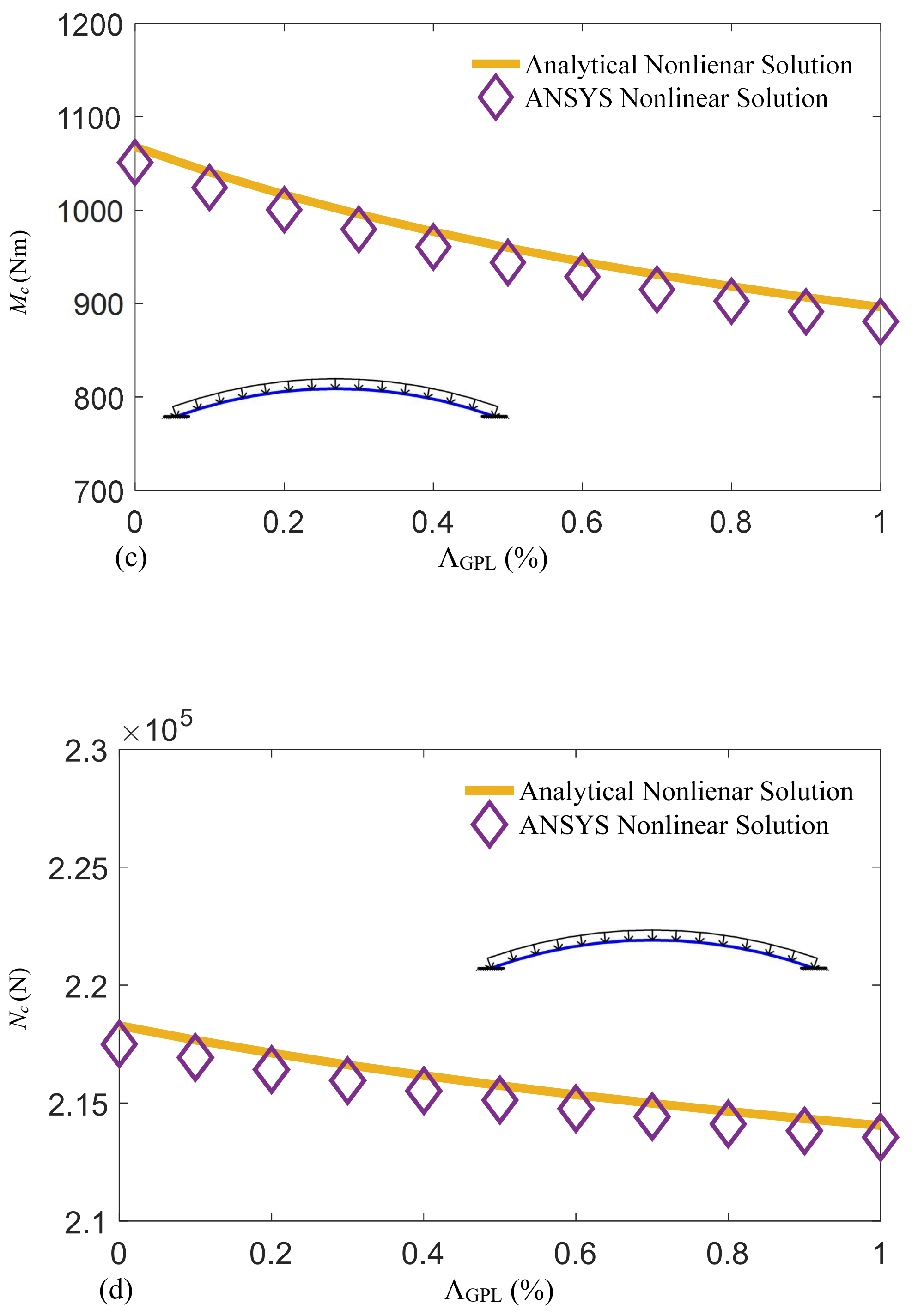

Figure 4.5 Results validation of (a) radial central displacement $\tilde{v}_c$; (b) axial displacement at quarter point $\tilde{w}_q$; (c) central moment M_c and (d) central axial force N_c for a fix-supported aluminium based FGP-GPLRC arch.

In the verifications of the nonlinear structural responses, agreements of results between the proposed approach and the ANSYS simulation can be well observed in Figure 4.4 and Figure 4.5. In addition to the demonstration of the accuracy of the proposed method, the computational times of two methods are also recorded herein. The total computational time of ANSYS was approximately 90 mins per individual calculating point in Figure 4.4 and Figure 4.5, whereas the calculation time of the proposed method was approximate 0.5 seconds per calculation point (less than 50 second for 101 individual calculation points). Thus, the proposed method has superior computational efficiency over the numerical method through ANSYS.

4.3.2 Result verifications of the structural buckling loads

The result verificaitons of the structural buckling loads of pin- and fix-ended supports are presented in this section. Figure 4.6 (a) presents the numerical verification for the anti-symmetric bifurcation buckling load for a fix-supported FGP-GPLRC arch with r=20mm, L=2m, f/L = 1/25, e_0 = 0.6 and porosity distribution 1. On the other hand, Figure 4.6 (b) presents the numerical verification for the symmetric limit point buckling load for a pin-supported FGP-GPLRC arch with r=5 mm, L=2 m, f/L=1/25, e_0 =0.6, and porosity distribution 2.

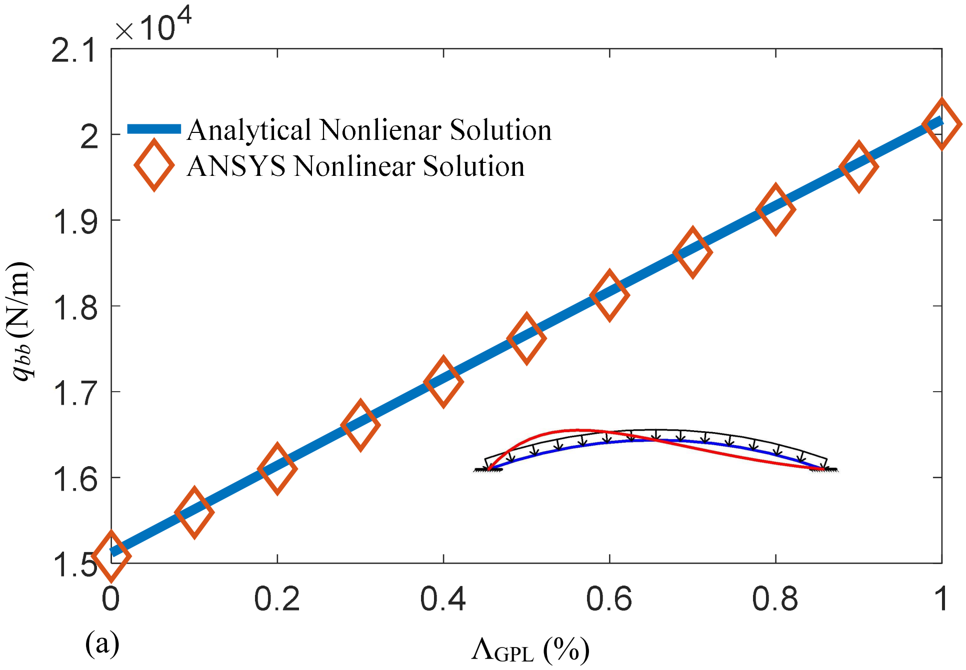

(a)

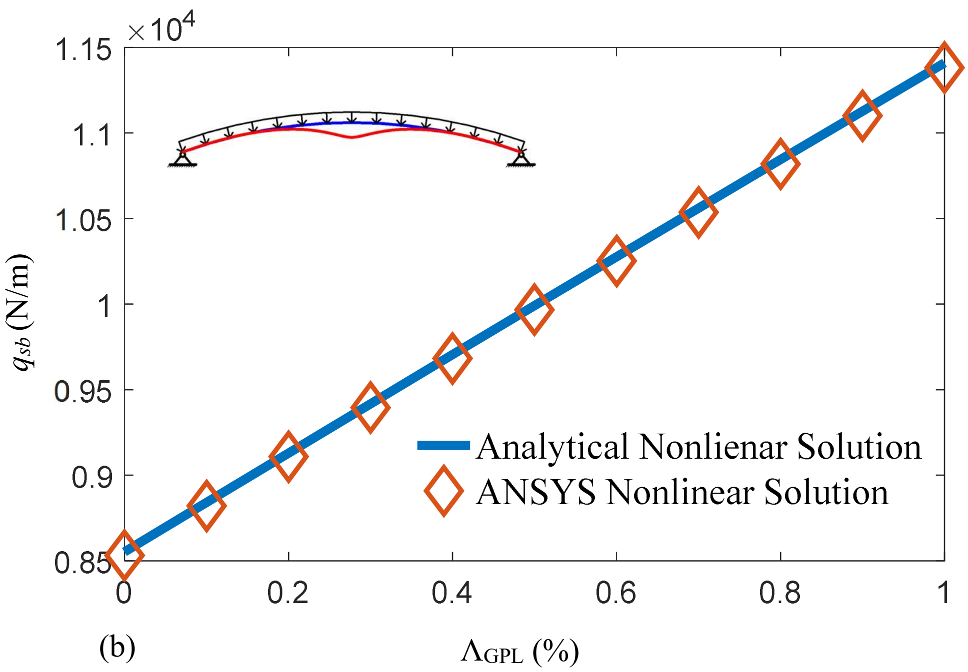

(b)

Figure 4.6 Results validation of buckling analysis (a) anti-symmetric bifurcation buckling load of a fix-supported aluminium based FGP-GPLRC arch and (b) limit point buckling load of a pin-supported aluminium based FGP-GPLRC arch.

In the buckling analysis verifications, the results presented in Figure 4.6 illustrate that the proposed analytical solution agrees well with the ANSYS's prediction. The total calculation time of ANSYS is about 10 hours per individual calculating point for the limit point buckling analysis and over 40 hours for the bifurcation buckling analysis. However, the calculation time of the proposed method is about 5 seconds per calculation point for the limit point buckling analysis and 0.5 seconds for the bifurcation buckling analysis. Once again, the computational efficiency of the proposed method is well demonstrated.

4.3.3 Numerical investigation - system responses and internal actions

The system responses and internal actions of FGP-GPLRC arches are studied in this section. Two case studies are presented: Case A presents a pin-supported FGP-GPLRC arch with porosity distribution type 1; and Case B presents a fix-supported FGP-GPLRC arch with porosity distribution type 2. The following parameters are adopted for both cases: r = 25 mm, L = 2 m, f/L = 1/10. The applied pressure is adopted as $q = \frac{0.7N_{pcr}}{R}$ for Case A and $q = \frac{0.7N_{fcr}}{R}$ for Case B. Figure 4.7 to Figure 4.10 present the the radial central displacement (v_c, $\theta = 0$), axial displacement at quarter point ($w_{q,}$, $\theta = 0.5\varphi$), central compressive axial force (N_c, $\theta = 0$), central bending moment(M_c, $\theta = 0$) and per meter length normalised to the solid arch without GPLs reinforcement. Figure 4.7 to Figure 4.10 are illustrated with various porosity coefficients in the x-axis and GPLs weight fractions in the y-axis, so the effectiveness of the graphene platelet reinforcement on the concerned nonlinear structural responses can be illustrated. As shown in Figure 4.7 to Figure 4.10, the GPLs reinforcement significantly reduces the nonlinear system responses of the arches with all porosity levels. Figure 4.11 presents the impacts of the porosity and the weight fraction of the GPLs reinforcement on the overall normalized mass of the arch. Indeed, the porosity has a significant contribution in the weight-reduction of the structure. On the other hand, the increase of the weight fraction of the GPLs reinforcement barely affects the normalized mass of the structure. Therefore, the mass contribution from the inserted GPLs on the overall structural weight can be neglected.

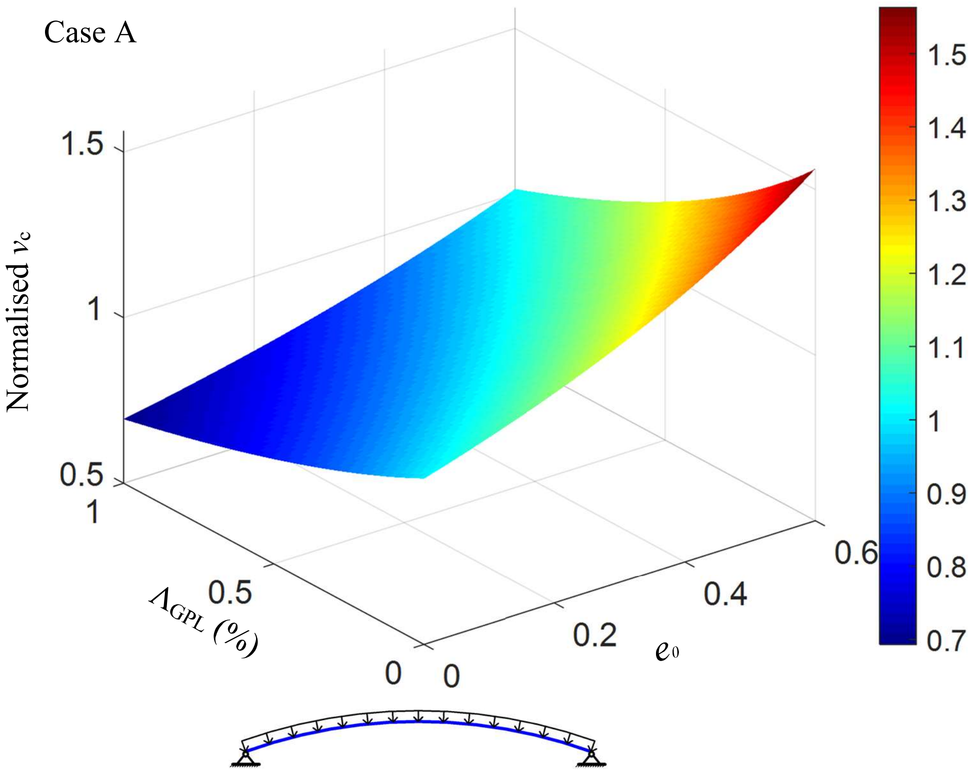

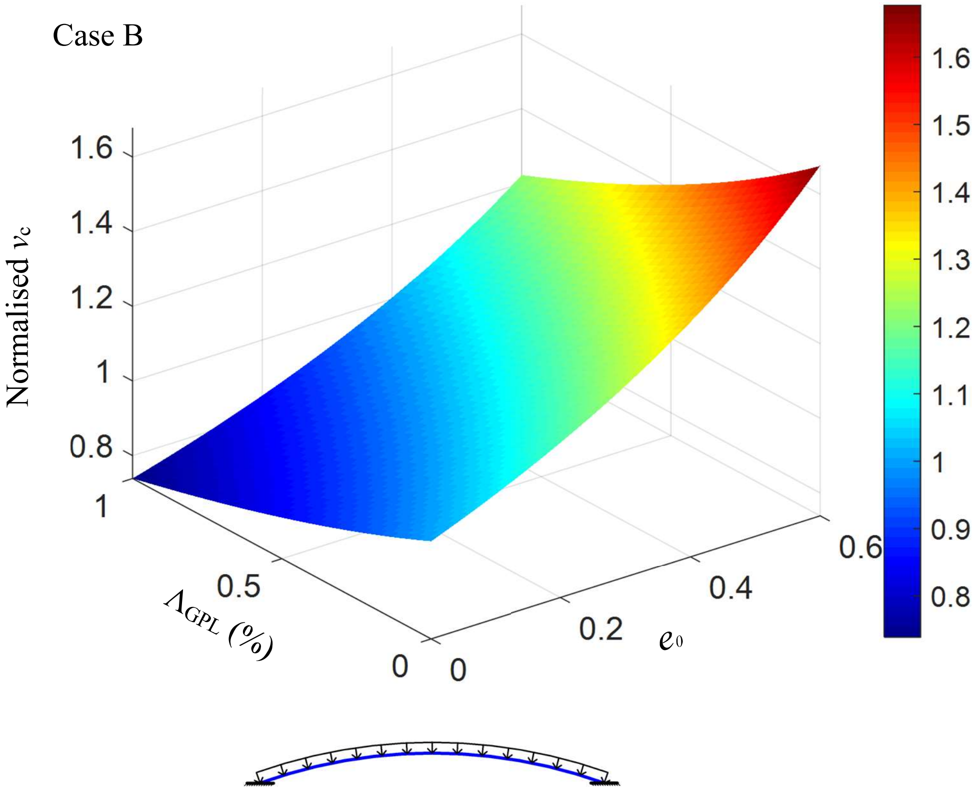

Figure 4.7 Normalised Radial Displacement v_c in the Case A: pin-supported; and in the Case B: fix-supported.

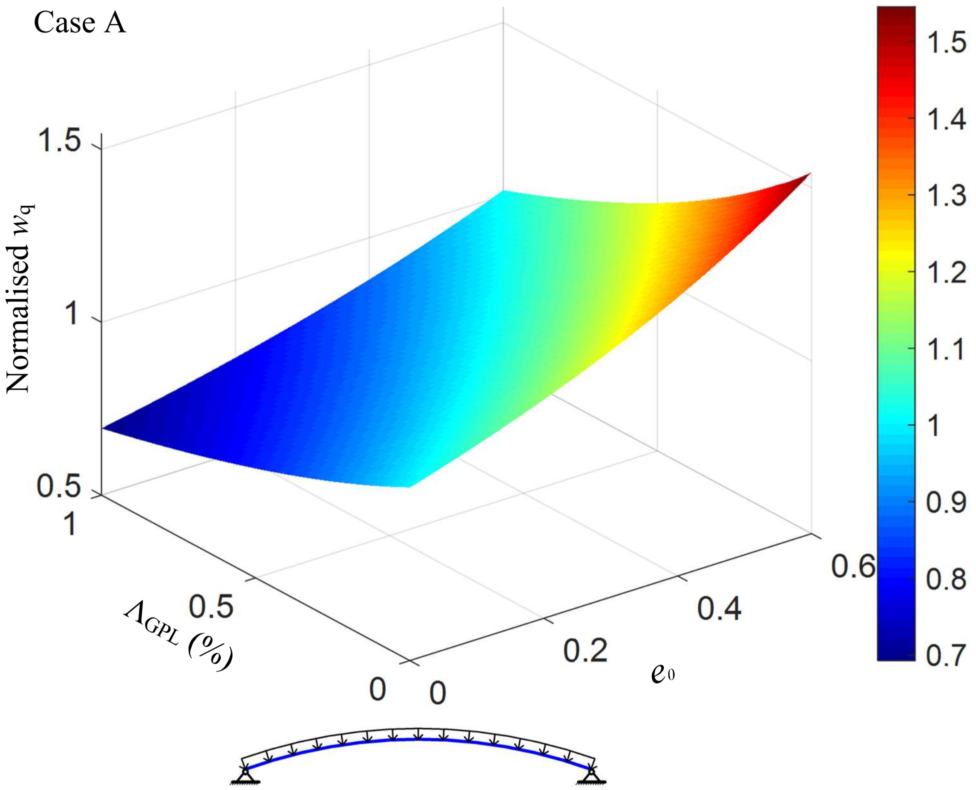

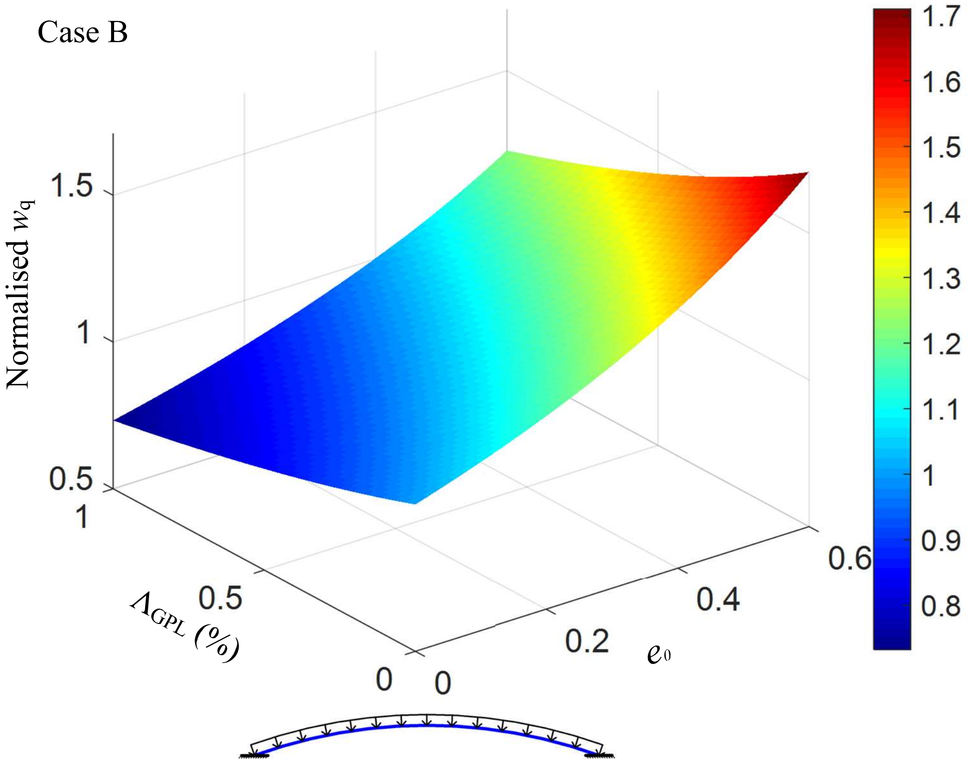

Figure 4.8 Normalised Axial Displacement w_q in the Case A: pin-supported; and in the Case B: fix-supported.

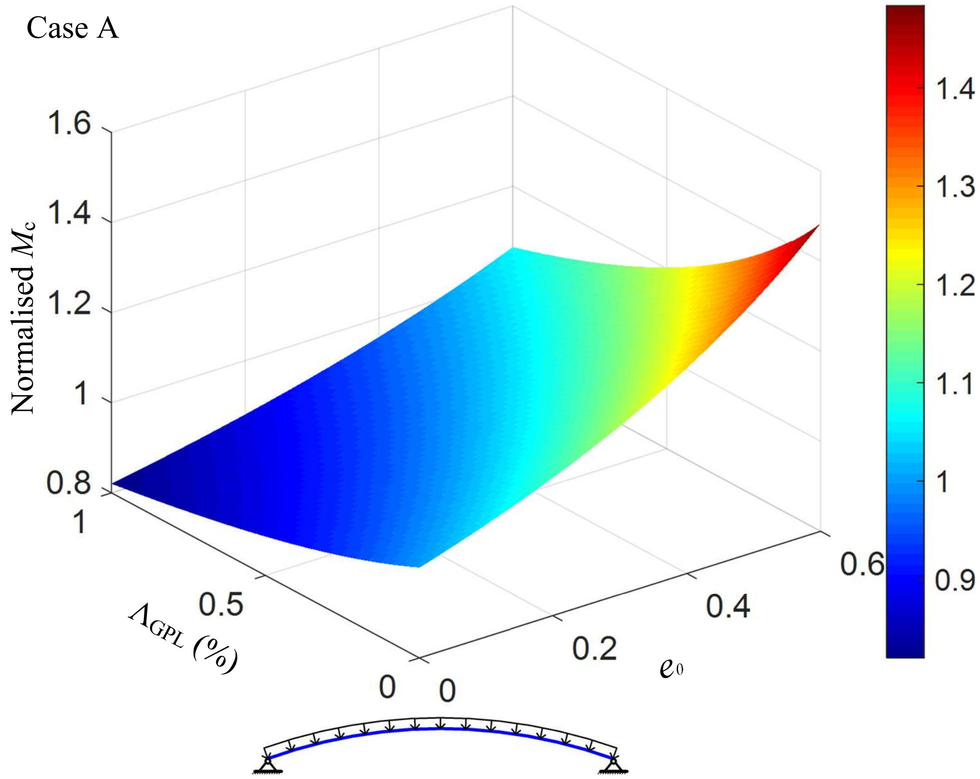

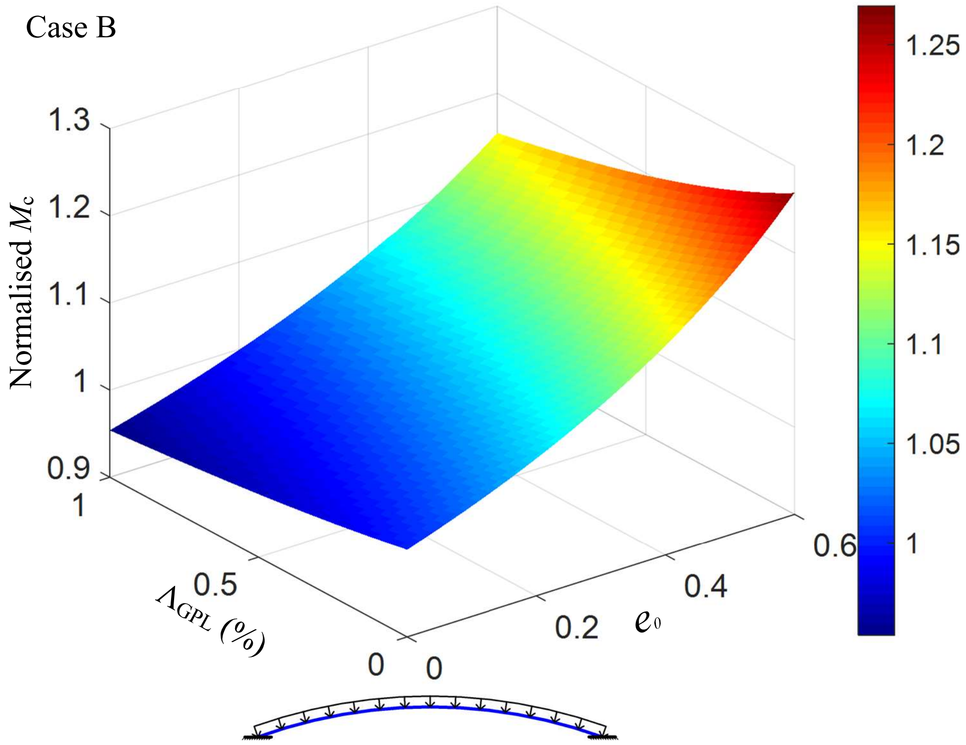

Figure 4.9 Normalised Bending Moment M_c in the Case A: pin-supported; and in the Case B: fix-supported.

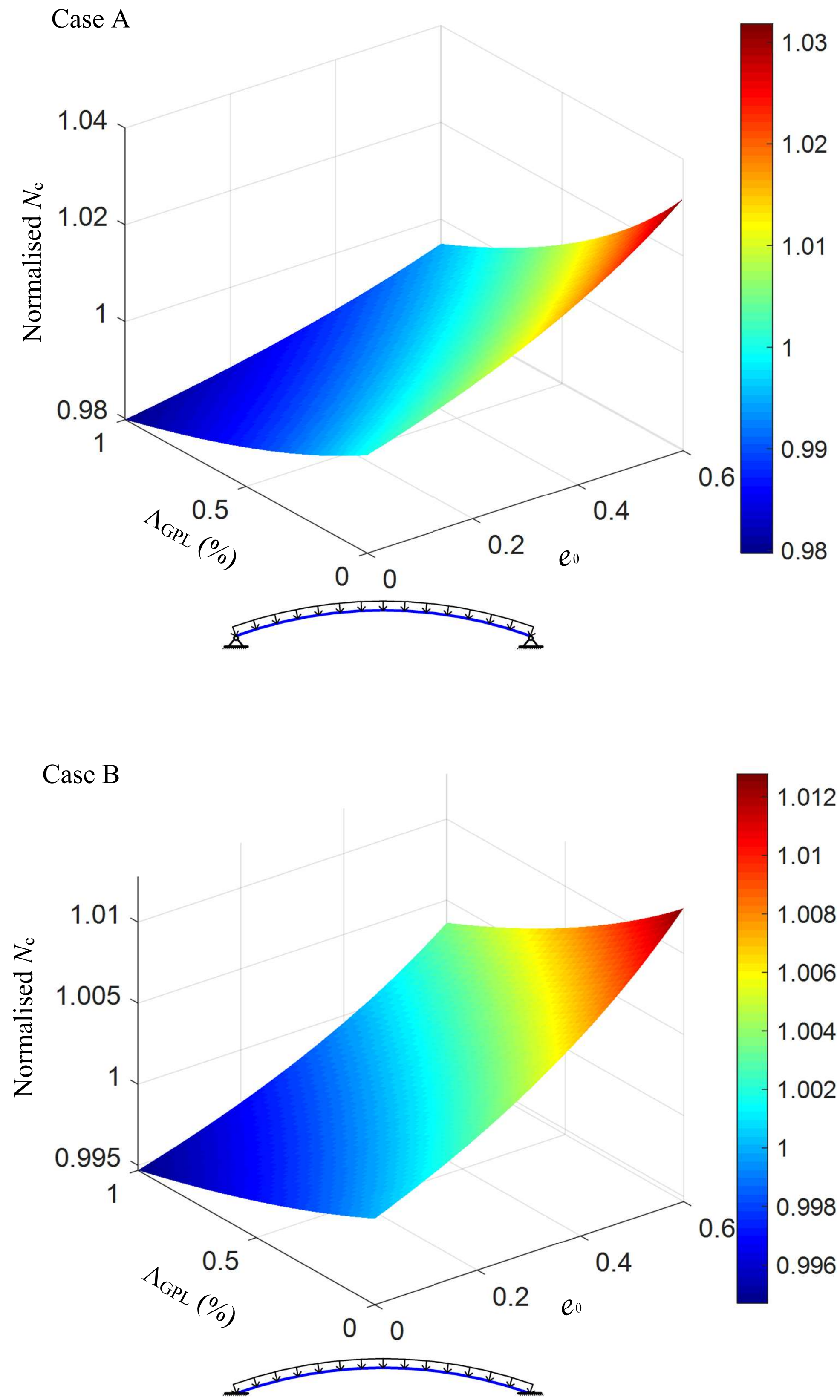

Figure 4.10 Normalised Compressive Axial Force N_c in the Case A: pin-supported; and in the Case B: fix-supported.

Case A

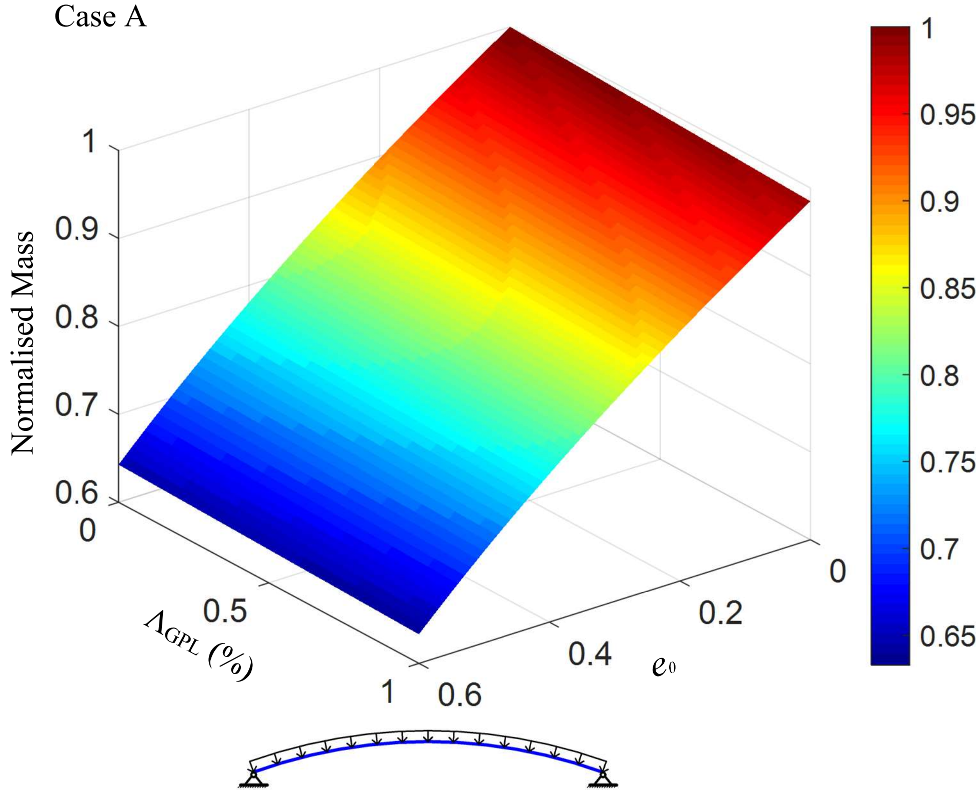

Case B

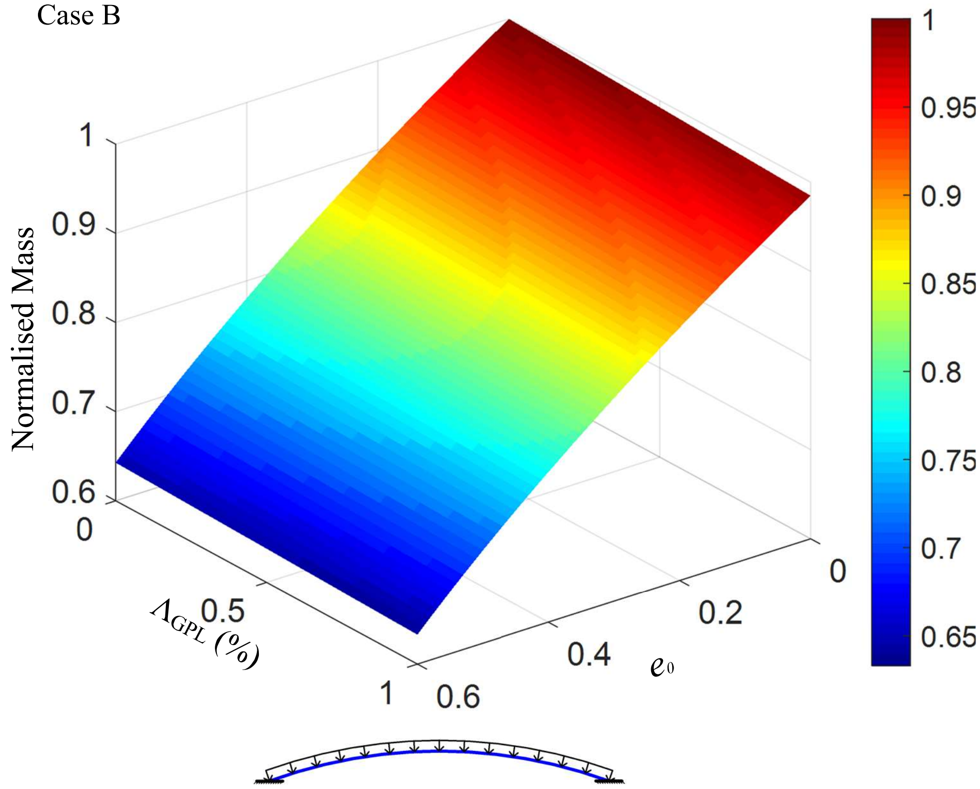

Figure 4.11 Normalised Mass per Arch Length in the Case A: pin-supported; and in the Case B: fix-supported. Note: y-axis(e_0) in Figure 4.11 is inversed for illustration purpose

4.3.4 Numerical investigation - buckling load and specific strength

The in-plane buckling strength and specific strength against buckling are studied in this section. The specific strength is the ratio between the buckling load and the mass of the arch which is defined as:

$$Specific\ strength = \frac{q_{bb}}{M_{arch}} \tag{4.67}$$

for bifurcation buckling load or

$$Specific\ strength = \frac{q_{sb}}{M_{arch}} \tag{4.68}$$

for limit point buckling load, where M_{arch} denotes the mass of the arch structure.

Case 1 presents the anti-symmetric bifurcation buckling load study of a pin-supported FGP-GPLRC with porosity distribution type 1. Figure 4.12 illustrates the bifurcation buckling load and specific strength defined in Eq. (4.68). The following geometrical parameters are used in this numerical investigation: *r*=20mm, *L*=2 m, *f/L*=1/25.

In the second case study, the symmetric limit point buckling load of a fix-supported FGP-GPLRC arch with porosity distribution type 2 is analysed by the proposed method. Figure 4.13 illustrates the symmetric limit point buckling load and the specific strength defined in Eq. (4.69). The following geometrical parameters are used in this example: *r* = 25 mm, *L* = 2 m, *f/L* = 1/25.

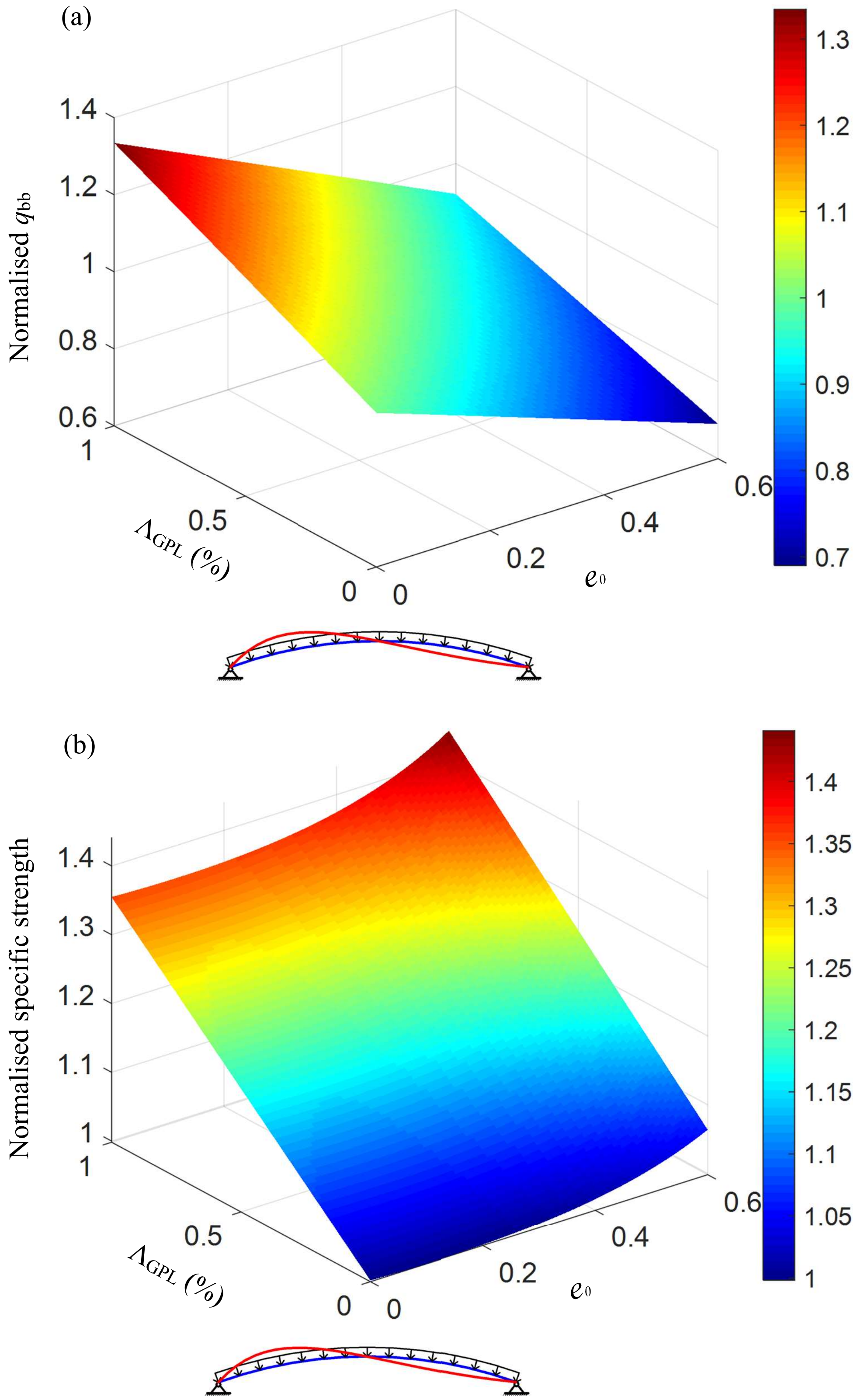

Figure 4.12 Stability analysis of a pin-supported FGP-GPLRC arch (a) normalised bifurcation buckling load (b) normalised specific strength against bifurcation buckling

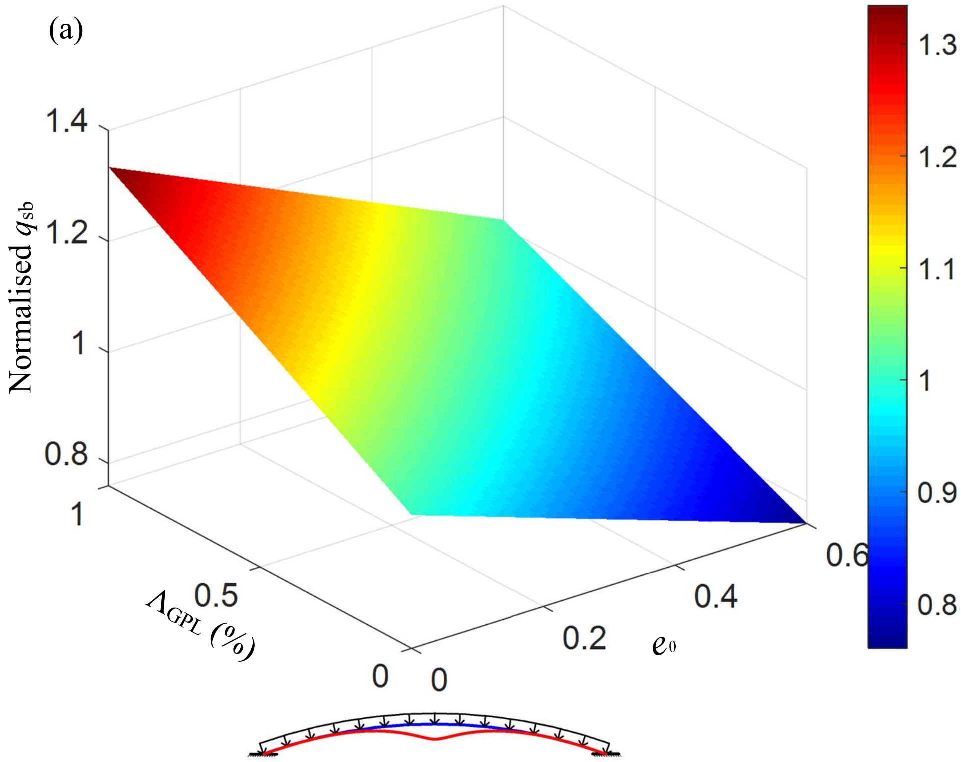

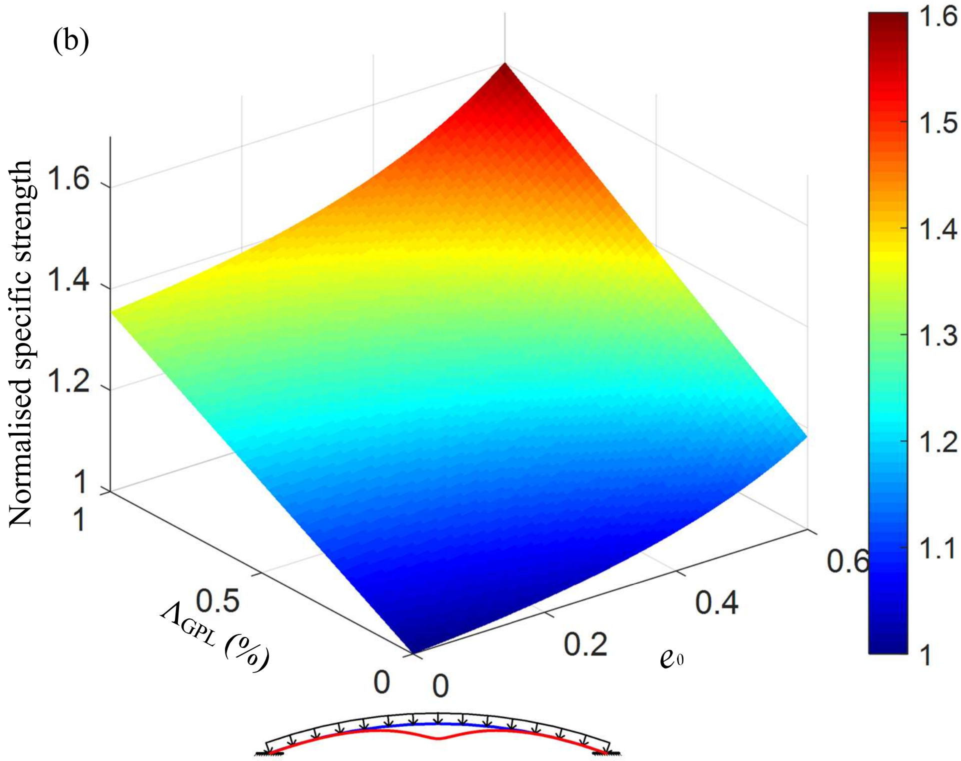

Figure 4.13 Stability analysis of a fix-supported FGP-GPLRC arch (a) normalised limit point buckling load (b) normalised specific strength against limit point buckling

In Figure 4.12 and Figure 4.13, it is noticeable that at any specific Λ_{GPL}, the increase of porosity e_0 reduces the buckling load of the pin- and fix-supported arches, but increases the specific strength of the two arches. The variations of the buckling loads and the specific strengths of the two considered arches against Λ_{GPL} and e_0 are not linear, but they are monotonic. Even though the porosity e_0 has a remarkable contribution in the specific strength, the side effect of this is that the buckling load of the arches will be reduced.

By introducing the GPL nano-composites, the buckling capacity and the specific strength of the two investigated arches increase significantly at all level of e_0. Therefore, the FGP-GPLRC arch has an excellent performance in specific strength against buckling and maintains a high level static buckling capacity. By using the proposed equations, the influence of the porosity and the GPLs reinforcement can be well illustrated. For example in Figure 4.13, it is evidently illustrated that by introducing a porosity level of 0.6, the specific strength is increased by approximately 20%. However, the buckling strength is reduced over 20% in this case. By adding 1% GPLs, the buckling load is maintained at the same level as the one without porosity. The specific strength, as demonstrated in Figure 4.13 (b), is increased dramatically by 60%.

4.3.5 Numerical investigation - equilibrium paths

In addition to the investigation on the buckling capacity of the FGP-GPLRC arch with various Λ_{GPL} and e_0, the equilibrium paths of the FGP-GPLRC arch with different porosity distributions are explored in this section. More specifically, the equilibrium paths of the FGP-GPLRC arches, the solid arch with the same geometric dimension of the FGP-

GPLRC arch, as well as the FGP arch without nano-composites against various porosities and GPL weight fractions are investigated. The illustrated result is normalised to the second mode flexural buckling load of the corresponding solid arch (Pi, Bradford, & Uy, 2002) given by: $N_{cr} = \dfrac{\pi^2 EI}{\left(S/2\right)^2}$ for pin supported arches, and $N_{cr} = \dfrac{\left(1.4303\pi\right)^2 EI}{\left(S/2\right)^2}$ for fix-supported arches. For each case, all adopted parameters are shown in the corresponding figure. The slenderness of the solid arch λ, is defined as $\lambda = \dfrac{R\varphi^2}{r_e}$ and used to distinguish the various buckling mode of the arch (Pi, Bradford, & Uy, 2002).

Figure 4.14 to Figure 4.17 present the equilibrium paths of pin-supported FGP-GPLRC arches, and Figure 4.18 to Figure 4.21 illustrated the equilibrium paths of fix-supported FGP-GPLRC arches. Figure 4.14 and Figure 4.18 demonstrate the case that no local extrema can be found thus the structure remains stable. That is, the buckling is not occurred for the pin- and fix-supported arches in Figure 4.14 and Figure 4.18, respectively. Figure 4.15 and Figure 4.19 demonstrate the case which only symmetric buckling mode is triggered. In these two figures, the porosity and GPL weight fraction have more obvious impacts on the upper limit points of the arches than the lower limit points. Figure 4.16 and Figure 4.20 demonstrate the case that symmetric buckling mode is triggered before the anti-symmetric buckling. In Figure 4.16, the lower bifurcation points are very close, while the variation of the upper bifurcation point is larger. Figure 4.17 and Figure 4.21 demonstrate the case that the anti-symmetric buckling mode occurs before the symmetric buckling mode is occurred. When the upper bifurcation point is reached, it snaps from the upper bifurcation point to the lower one.

From the observation, by adding the porosity to the arch, the static response is increased, and the buckling load is reduced. The FGP arch with the porosity distribution 2 has less static responses and has a higher buckling capacity comparing to the FGP arch with the porosity distribution 1. This phenomenon is not changed with the GPLs reinforcement. Figure 4.15 shows the porosity result a significant reduction in the buckling capacity. By introducing the GPLs reinforcement, the overall structural strength is improved significantly; the buckling capacity is also increased. In the extreme case, i.e. when porosity level is very high such as shown in Figure 4.16 and 3.20, the FGP-GPLRC arch with low level of GPLs reinforcement may not reach the same buckling capacity comparing to the solid arch with the same geometric configuration (Figure 4.16), but can lead to a better result with higher level of GPLs reinforcement (Figure 4.19).

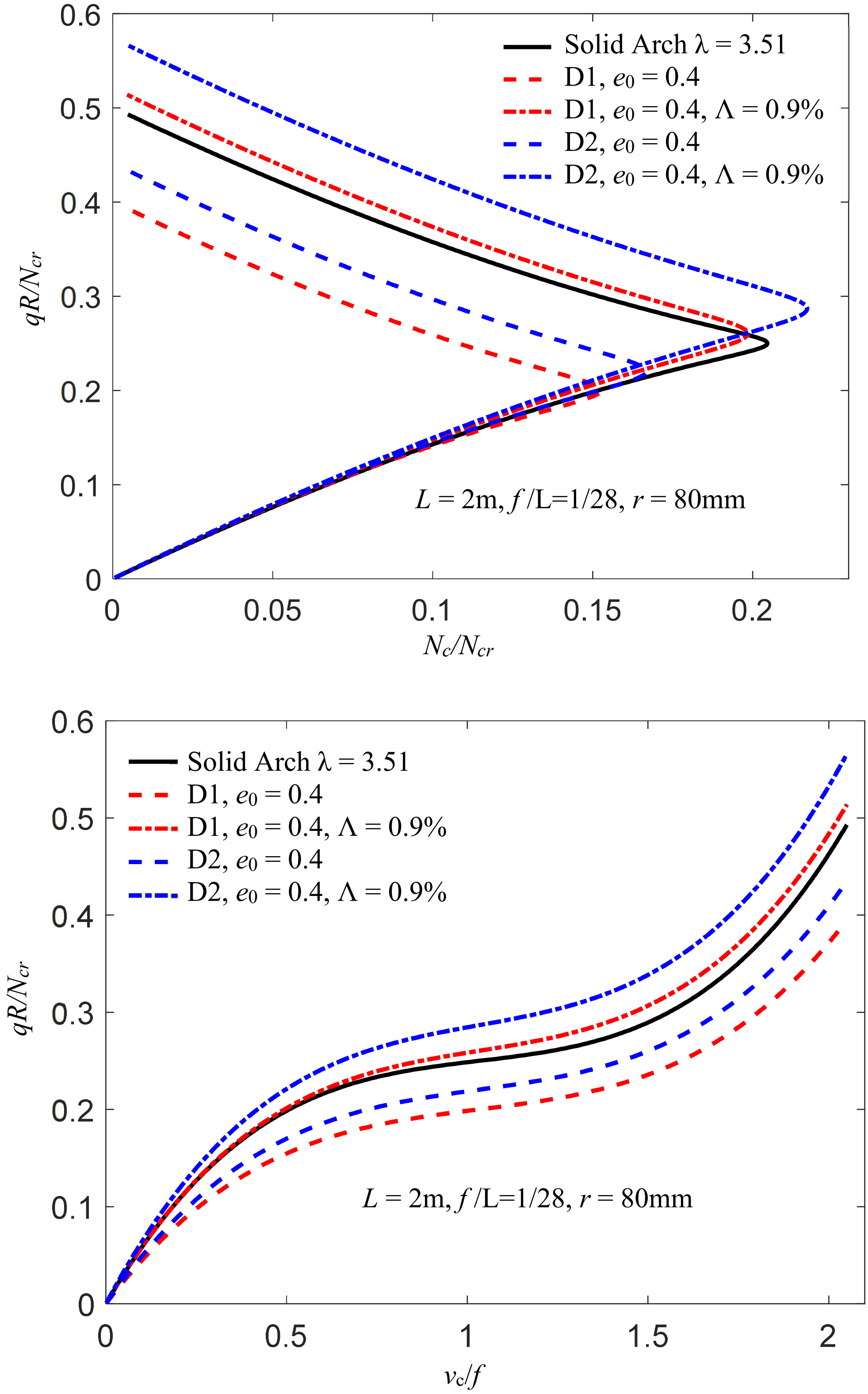

Figure 4.14 Nonlinear equilibrium paths of a pin-supported aluminium based FGP-GPLRC arch, Case 1

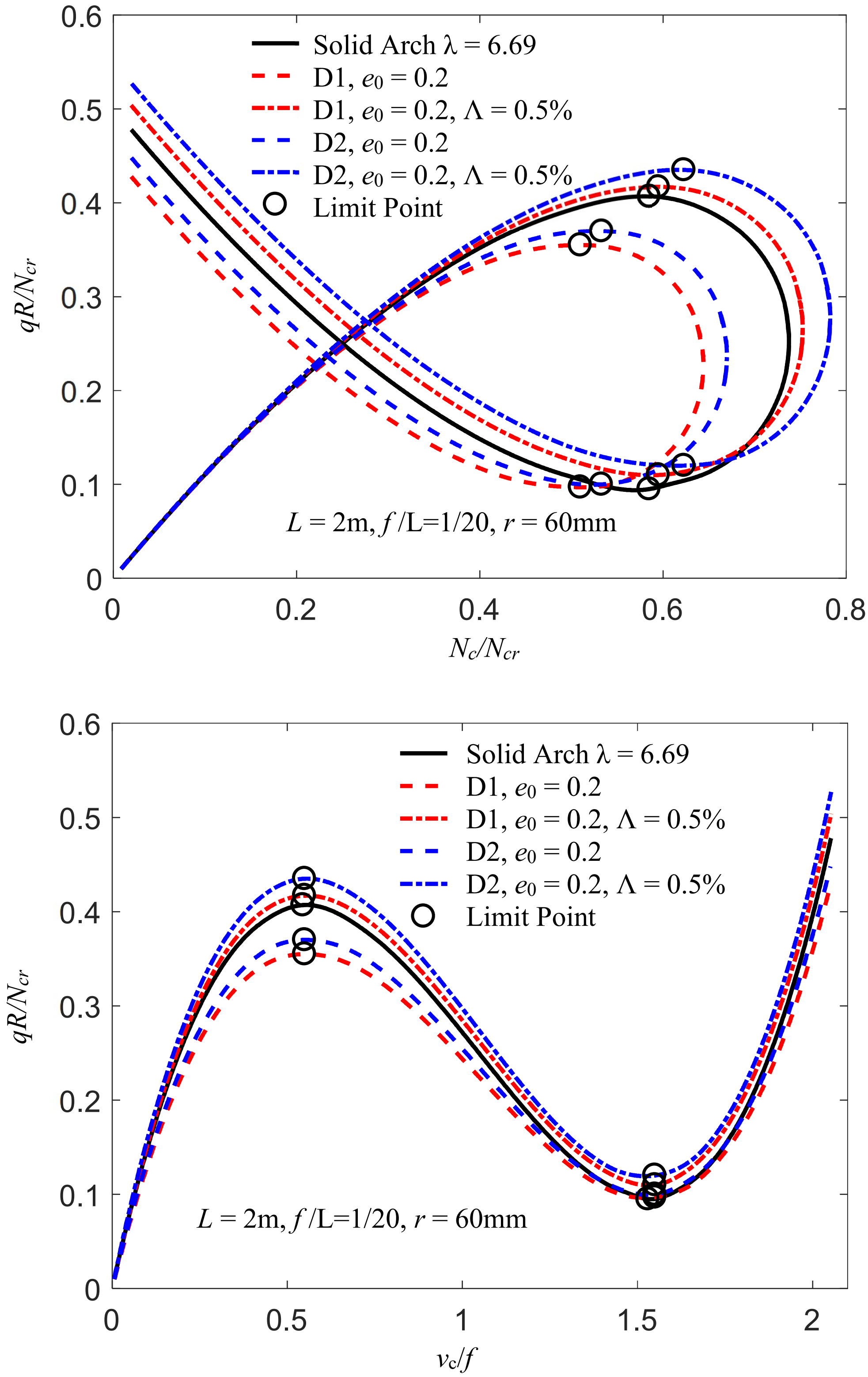

Figure 4.15 Nonlinear equilibrium paths of a pin-supported aluminium based FGP-GPLRC arch, Case 2

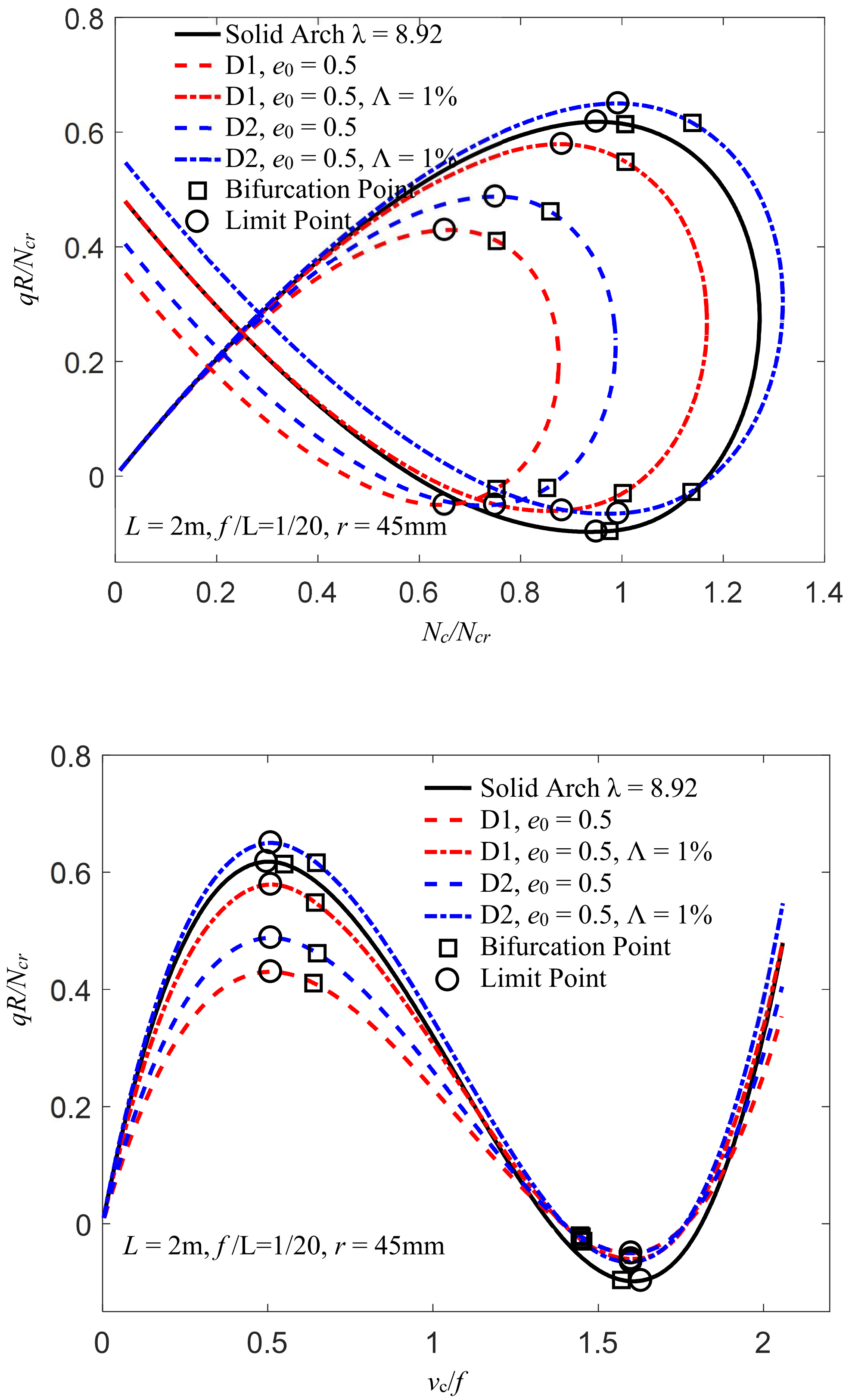

Figure 4.16 Nonlinear equilibrium paths of a pin-supported aluminium based FGP-GPLRC arch, Case 3

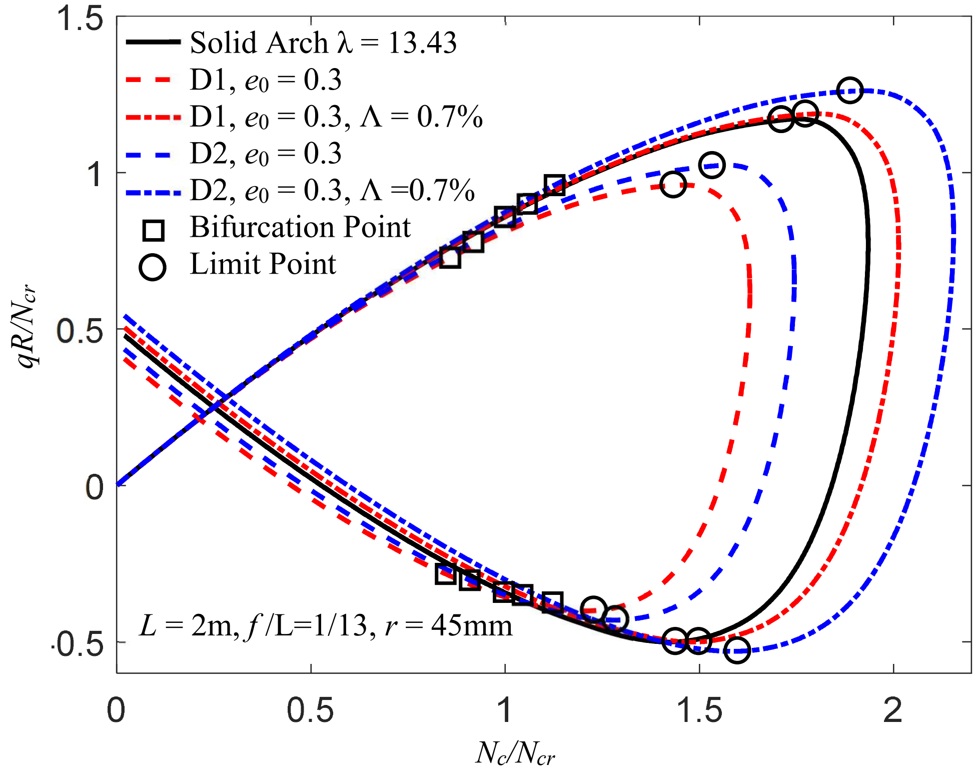

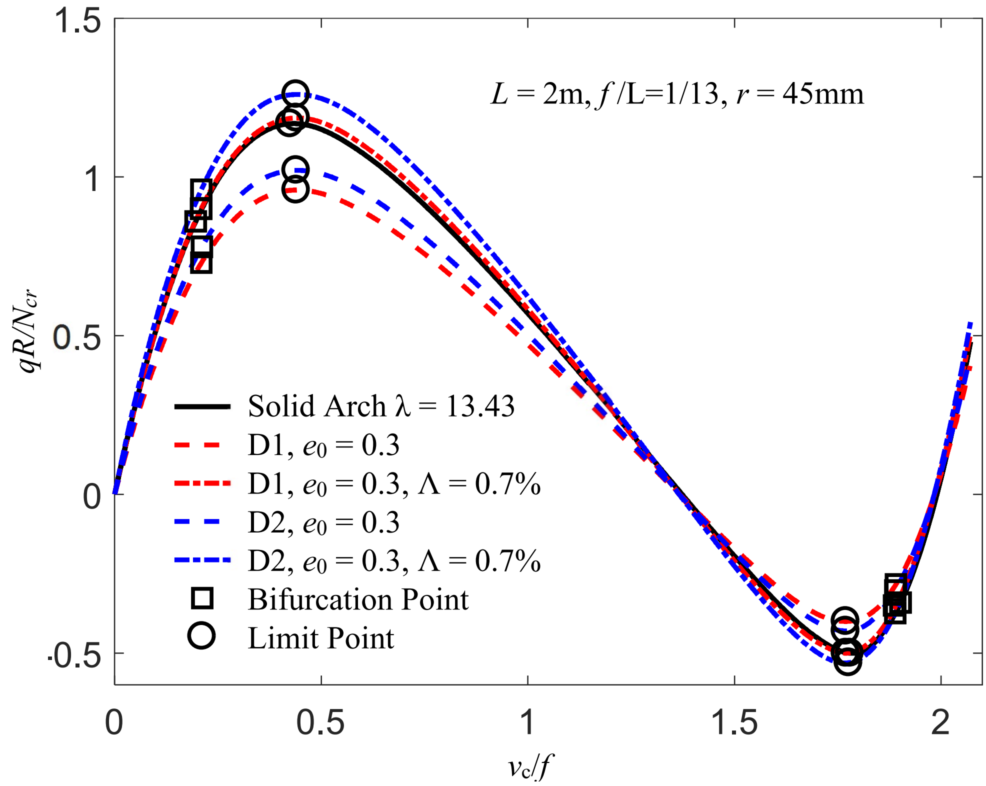

Figure 4.17 Nonlinear equilibrium paths of a pin-supported aluminium based FGP-GPLRC arch, Case 4

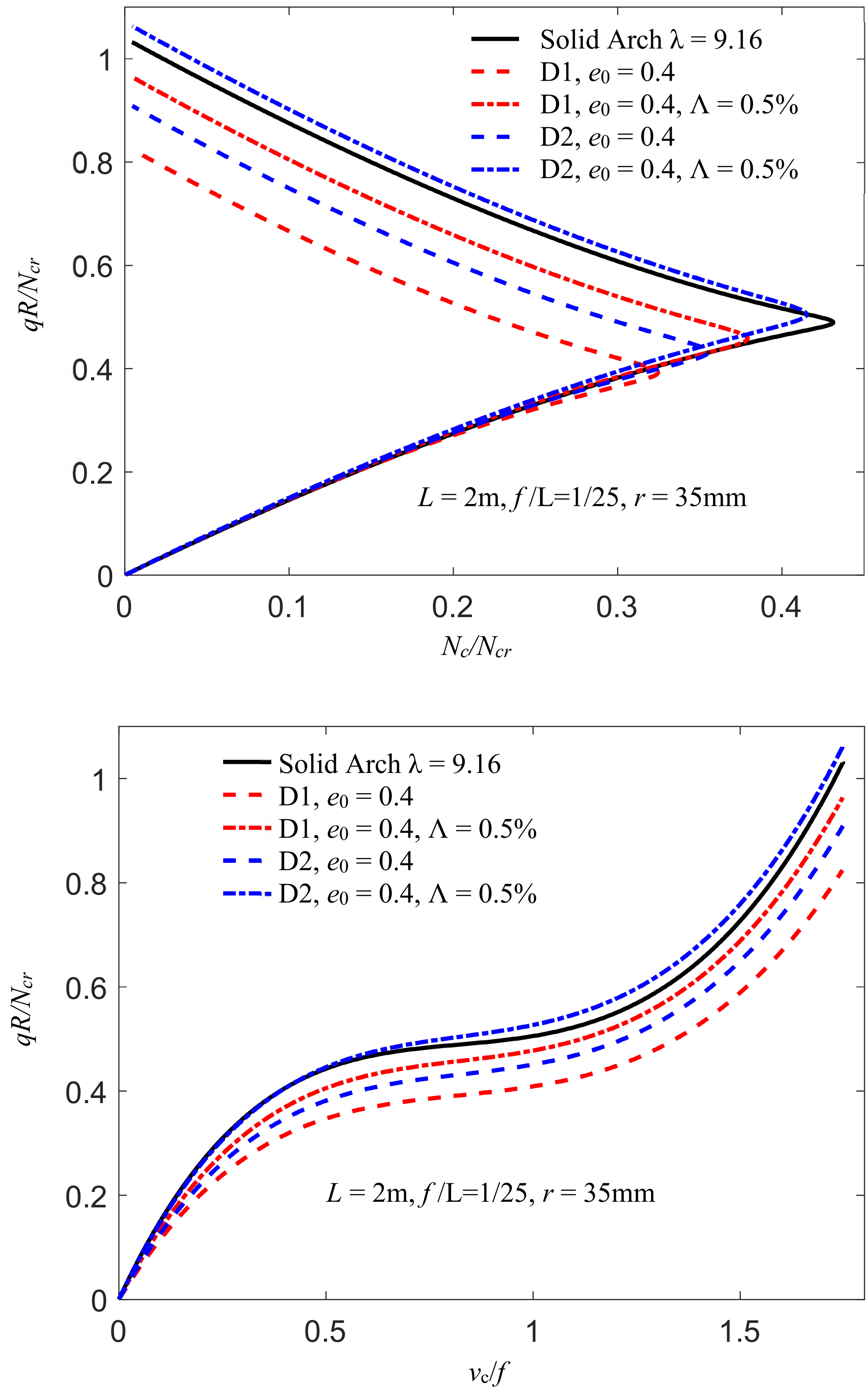

Figure 4.18 Nonlinear equilibrium paths of a fix-supported aluminium based FGP-GPLRC arch, Case 1

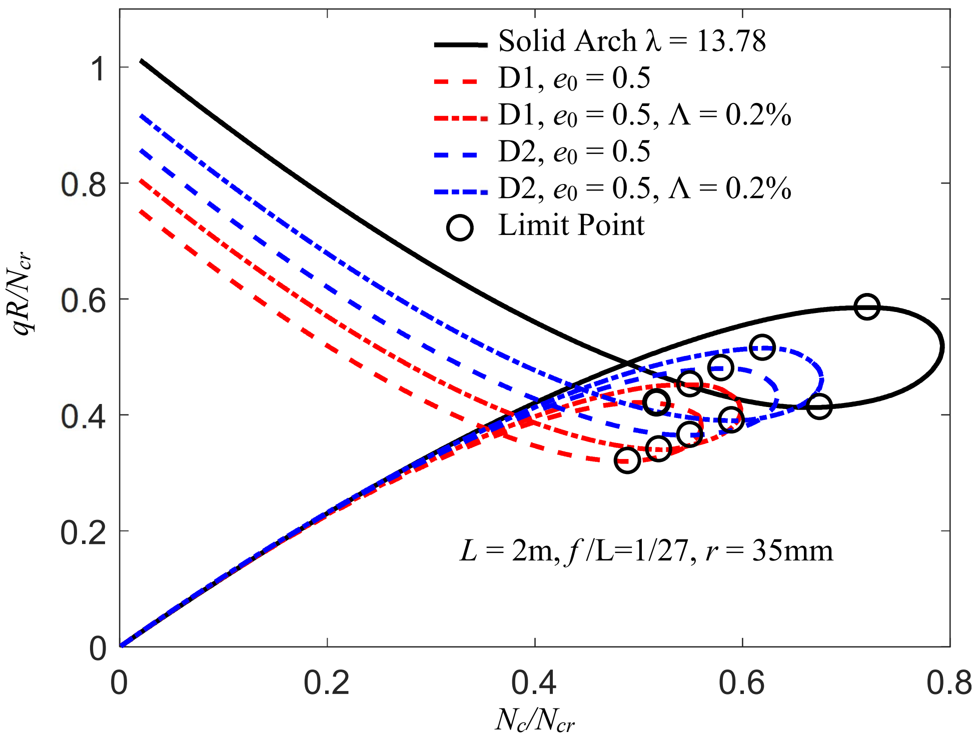

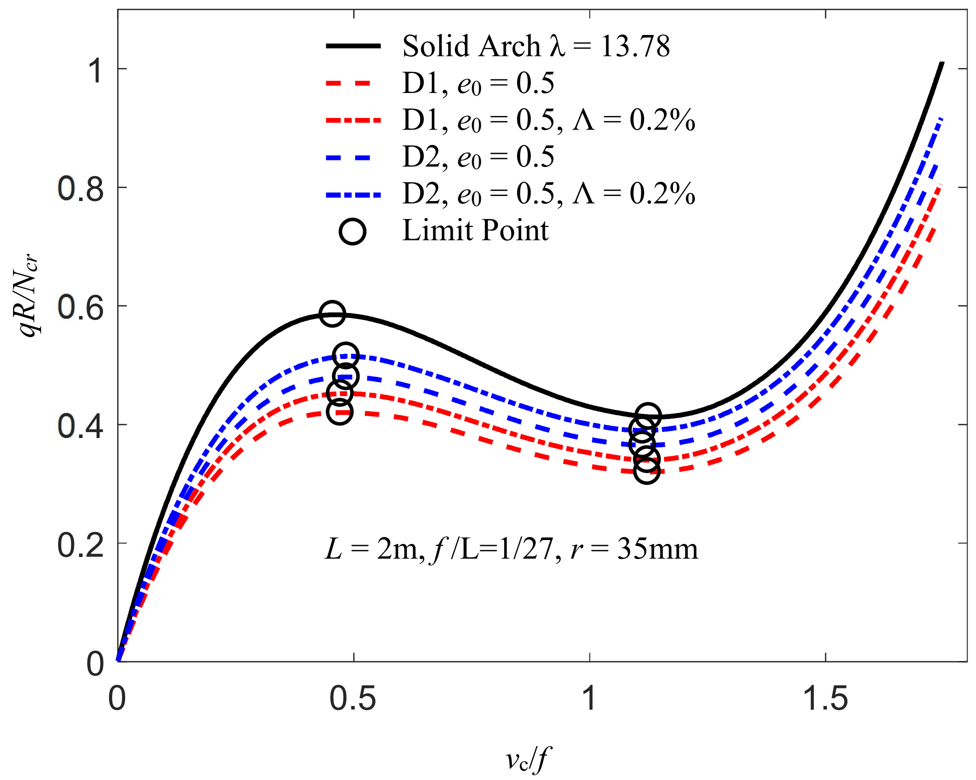

Figure 4.19 Nonlinear equilibrium paths of a fix-supported aluminium based FGP-GPLRC arch, Case 2

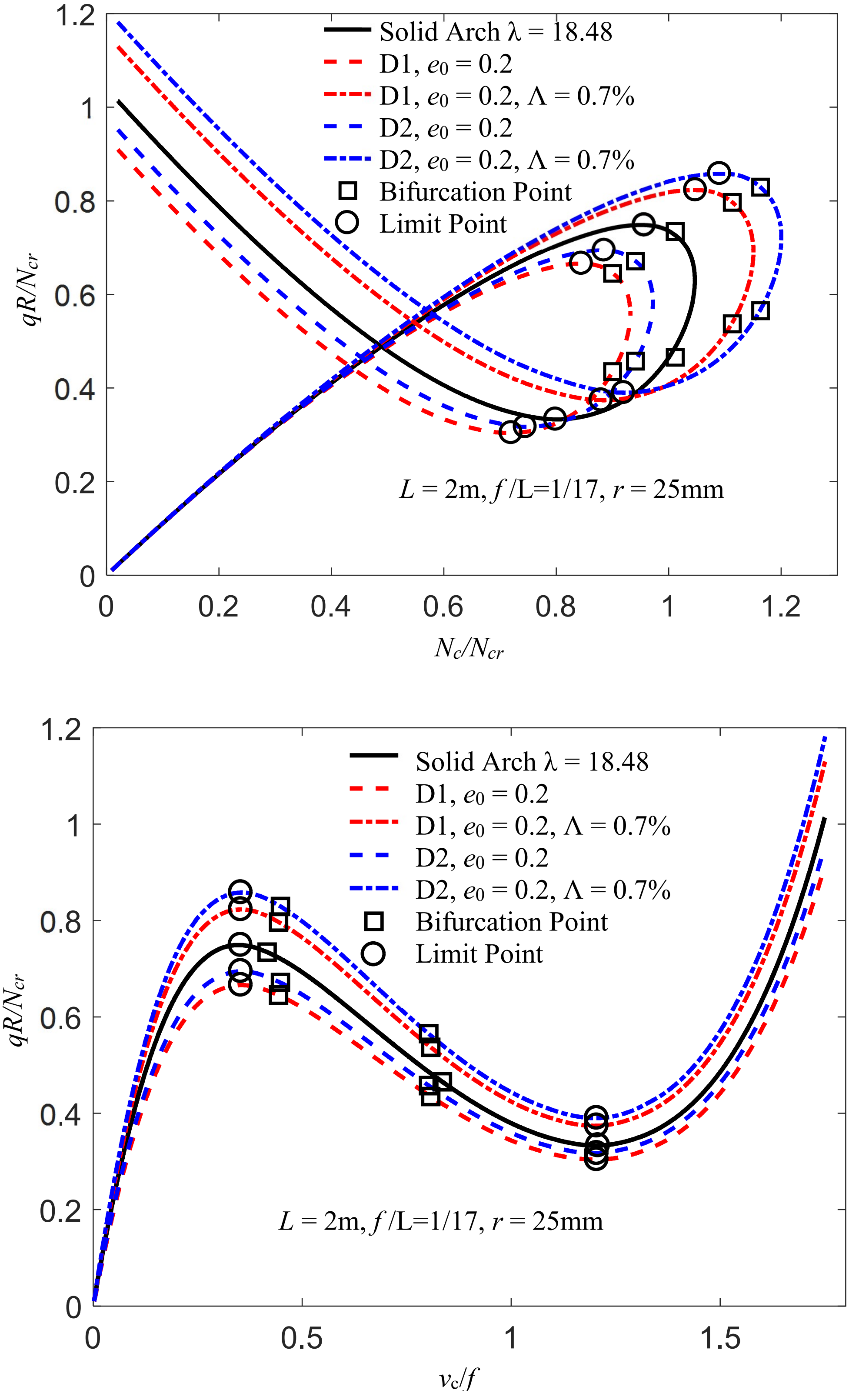

Figure 4.20 Nonlinear equilibrium paths of a fix-supported aluminium based FGP-GPLRC arch, Case 3

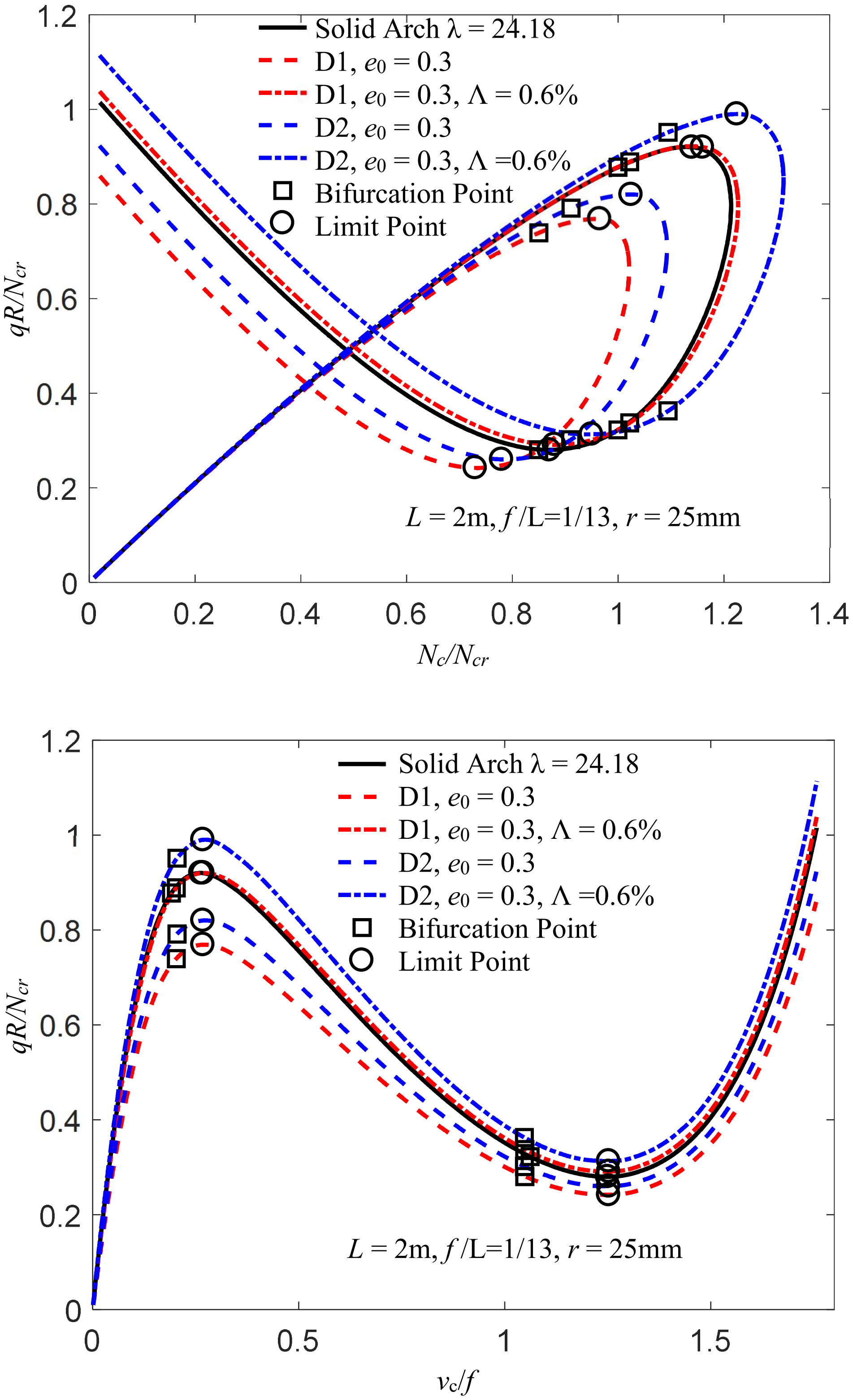

Figure 4.21 Nonlinear equilibrium paths of a fix-supported aluminium based FGP-GPLRC arch, Case 4

4.4 Conclusion

In this chapter, the nonlinear static response and buckling analysis of FGP-GPLRC circular shallow arch under radial uniform load are investigated. The nonlinear elastic equations based on the Euler-Bernoulli hypothesis are derived by adopting the potential energy method. In order to verify the correctness of the proposed approaches, the computational results are compared with those produced by commercial software ANSYS 18.1. The results show the proposed equations conform to the calculation of ANSYS, but with much better calculation efficiency. Thus, the proposed method can be used as benchmarks for the further numerical investigations of the FGP-GPLRC arches. Furthermore, the enhanced calculation efficiency can contribute to the further design optimisation or reliability analysis of FGP-GPLRC arches when numerous calculations are required.

The advantages of the GPLs reinforcement are illustrated in 3-dimensional figures. Compare to the solid arch, the FGP arch has a good performance in weight reduction and has a high strength-to-weight ratio, however, the strength is sacrificed, and the static responses are increased. By introducing the GPLs reinforcing technique, the FGP-GPLRC arches maintain all the advantages of the FGP arches, furthermore, it improves the buckling capacity and reduces the static responses significantly. Also, the self-weight of the arch is further reduced as the density of GPLs is much smaller than most metal matrixes. Moreover, it is found the FGP-GPLRC arches with porosity distribution 2 has less static response and higher buckling load than the FGP-GPLRC arches with porosity distribution 1 from the equilibrium path illustration.

Chapter 5

Conclusion and future studies

5.1 Conclusion

In order to meet the modern engineering design, the in-plane static behaviour of two types of advanced composite arches have been discussed in this thesis. Analytical solutions are provided and validated. Comparing to the commercial finite element software, the proposed analytical approach has an unbeatable calculation efficiency, while the accuracy is guaranteed.

Chapter 3 investigates the in-plane static responses and buckling analysis of FG shallow arch structures under uniform pressures. Based on the Euler-Bernoulli hypothesis, analytical solutions of the buckling load are derived by using the virtual work method. Both linear and geometric nonlinear equation in static responses are given. Also, two buckling modes are discussed in the stability analysis, which are the symmetric buckling and the anti-symmetric buckling. The solutions are validated by ANSYS APDL 18.1. By adopting the derived analytical solution, the relationship between the buckling load and the various FG material properties can be analysed efficiently. The applicability and effectiveness of the proposed analytical approach for the geometric nonlinear buckling analysis of FG arch structures are demonstrated through numerical examples.

Chapter 4 presents an analytical approach to the static responses and in-plane buckling analysis of FGP-GPLRC circular shallow arch sustaining uniform radial pressure. The geometric nonlinearity is considered. Analytical solutions are derived by potential energy method based on Euler-Bernoulli beam theory. Results are verified by ANSYS APDL 18.1, the accuracy and the calculation efficiency are compared. The effect of various porosity patterns, porosity level and nano-reinforcement ratio are discussed. System responses, internal actions, buckling analyses, and equilibrium paths of the FGP-GPLRC arches are investigated. In addition, the influence of the porosity level and nano-reinforcement level are illustrated against the nonlinear responses, internal actions and the buckling strength.

5.2 Future studies

This thesis assessed static responses and buckling analysis of the FGM arches and FGP-GPLRC arches under uniform pressure. Further researches and investigations are needed to fulfil the design criteria of advanced composite arch, including:

1. Static responses and stability analysis of FGP-GPLRC arches under point load at arbitrary point.
2. Natural frequency of FGP-GPLRC arches.
3. Dynamic responses and instabilities of FGP-GPLRC arches under imposed/cyclic load.
4. Non-deterministic study in the FPG-GPLRC arches considering geometric and material uncertainties.

References

Arockiasamy, M., Chidambaram, S., Amer, A., and Shahawy, M. (2000). Time dependent deformations of concrete beams reinforced with CFRP bars. *Composites Part B: Engineering, 31(67):* 577 - 592.

Asgari H., Bateni M., Kiani Y. & Eslami M.R. (2014). Non-linear thermo-elastic and buckling analysis of FGM shallow arches. *Composite Structures, 109,* 75-85.

Attia M.A. & Rahman A.A.A. (2018). On vibrations of functionally graded viscoelastic nanobeams with surface effects. *International Journal of Engineering Science, 127,* 1-32.

Austin, W. J. (1971). In-plane bending and buckling of arches. *Journal of the Structural Division, ASCE, 97(5):* 1575 - 1592.

Austin, W. J. and Ross, T. J. (1976). Elastic buckling of arches under symmetrical loading. *Journal of the Structural Division, ASCE, 102(5):* 1085 - 1095.

Aydogdu M, Taskin V. (2007) Free vibration analysis of functionally graded beamswith simply supported edges. *Materials & Design, 28(5):* 1651 - 1656

Bateni M. & Eslami M.R. (2014). Non-linear in-plane stability analysis of FGM circular shallow arches under central concentrated force. *International Journal of Non-Linear Mechanics, 60,* 58-69.

Bateni M. & Eslami M.R. (2015). Non-linear in-plane stability analysis of FG circular shallow arches under uniform radial pressure. *Thin-Walled Structures,* 94, 302-313.

Calhoun, P. R. and DaDeppo, D. A. (1983). Non-linear finite element analysis of clamped arches. *Journal of Structural Engineering, ASCE, 109(3):* 599612.

Chen D., Yang J. & Kitipornchai S. (2015). Elastic buckling and static bending of shear deformable functionally graded porous beam. *Composite Structures, 133*, 54-61.

Chen D., Yang J. & Kitipornchai S. (2016a). Free and forced vibrations of shear deformable functionally graded porous beams. *International Journal of Mechanical Sciences 108-109*, 14–22.

Chen D., Yang J. & Kitipornchai S. (2016b). Nonlinear vibration and postbuckling of functionally graded graphene reinforced porous nanocomposite beams. *International Journal of Mechanical Sciences, 108-109*, 14-22.

DaDeppo, D. A. and Schmidt, R. (1969). Non-linear analysis of buckling and post-buckling behaviour of circular arches. *Journal of Applied Mathematics and Physics, 20(6):* 847-857.

Dehrouyeh-Semnani A.M. (2018). On the thermally induced non-linear response of functionally graded beams. *International Journal of Engineering Science, 125,* 53-74.

Dou C., Guo Y.-L., Zhao S.-Y. & Pi Y.-L. (2015). Experimental investigation into flexural-torsional ultimate resistance of steel circular arches. *Journal of Structural Engineering, 141(10),* 04015006.

Dou C., Guo Y.-L., Zhao S.-Y. & Pi Y.-L. (2016). Flexural-torsional buckling resistance design of circular arches with elastic end restraints. *Journal of Structural Engineering, 142(2),* 04015104.

Dou C., Jiang Z.-Q., Pi Y.-L. & Gao W. (2018). Elastic buckling of steel arches with discrete lateral braces. *Engineering Structures, 156,* 12–20.

Elias, Z. M. and Chen, K. L. (1988). Non-linear shallow curved-beam finite element. *Journal of Engineering Mechanics, ASCE, 114(6):* 1076 - 1087.

Evci C. & Gulgec M. (2018). Functionally graded hollow cylinder under pressure and thermal loading: Effect of material parameters on stress and temperature distributions. *International Journal of Engineering Science, 123,* 92-108.

Feng C., Kitipornchai S. & Yang J. (2017a). Nonlinear free vibration of functionally graded polymer composite beams reinforced with grapheme platelets (GPLs). *Engineering Structures, 140,* 110-119.

Feng C., Kitipornchai S. & Yang J. (2017b). Nonlinear bending of polymer nanocomposite beams reinforced with non-uniformly distributed grapheme platelets (GPLs). *International Journal of Structural Stability and Dynamics, 110,* 132-140.

Frikha A. and Dammak F. (2017), Geometrically non-linear static analysis of functionally graded material shells with a discrete double directors shell element, *Computer Methods in Applied Mechanics and Engineering, 315:* 1-24

Govorov A., Wentzel D., Miller S., Kanaan A. & Sevostianov I. (2018). Electrical conductivity of epoxy-graphene and epoxy-carbon nanofibers composites subjected to compressive loading. *International Journal of Engineering Science, 123,* 174-180.

Hangai Y., Saito K., Utsunomiya T., Kitahara S., Kuwazuru O. & Yoshikawa N. (2013). Compression properties of Al/Al-Si-Cu alloy functionally graded aluminum foam fabricated by friction stir processing route. *Materials Transactions, 54,* 405-408.

Hashemi R. (2016). On the overall viscoelastic behavior of graphene/polymer nanocomposites with imperfect interface. *International Journal of Engineering Science, 105,* 38-55.

Huang Y., Yang Z., Liu A. & Fu J. (2018). Nonlinear buckling analysis of functionally graded graphene reinforced composite shallow arches with elastic rotational constraints under uniform radial load. *Materials (Basel), 11(6),* 910.

Jabbari M., Mojahedin A, Khorshidvandb A. & Eslami M. (2014). Buckling analysis of a functionally graded thin circular plate made of saturated porous materials. *Journal of Engineering Mechanics, 140(2),* 287-295.

Kitipornchai S., Chen D. & Yang J. (2017). Free vibration and elastic buckling of functionally graded porous beams reinforced by graphene platelets. *Materials and Design*, *116*, 656-665.

Koizumi M. (1997). FGM activities in Japan. *Composites Part B: Engineering, 28:* 1-4.

Liu A., Bradford M.A. & Pi Y.-L. (2017). In-plane nonlinear multiple equilibria and switches of equilibria of pinned–fixed arches under an arbitrary radial concentrated load. *Archive of Applied Mechanics, 87,*1909–1928.

Liu A., Lu H., Fu J., Pi Y.-L., Huang Y., Li J. & Ma Y. (2017). Lateral-torsional buckling of circular steel arches under arbitrary radial concentrated load. Journal of Structural Engineering 143(9): 04017129.

Liu A., Lu H., Fu J. & Pi Y.-L. (2017). Lateral-torsional buckling of fixed circular arches having a thin-walled section under a central concentrated load. *Thin-Walled Structures, 118,* 46-55.

Liu A., Lu H., Fu J., Pi Y.-L., Huang Y. Li J. & Ma Y. (2017). Analytical and experimental studies on out-of-plane dynamic instability of shallow circular arch based on parametric resonance. *Nonlinear Dynamics 87,* 677-694.

Liu A., Yang Z. Bradford M.A. & Pi Y.-L. (2018). Nonlinear dynamic buckling of fixed shallow arches under an arbitrary step radial point Load. *Journal of Engineering Mechanics, 144(4),* 04018012.

Liu A., Yang Z., Lu H., Fu J. & Pi Y.-L. (2018). Experimental and analytical investigation on the in-plane dynamic instability of arches owing to parametric resonance. *Journal of Vibration and Control, 24(19),* 4419-4432.

Luo K., Pi Y.-L., Bradford M.A. & Gao W. (2013a). Long-term in-plane analysis of concrete-filled steel tubular arches. *American Environmentalism: Philosophy, History, and Public Policy,* 119-125.

Luo K., Pi Y.-L., Gao W. & Bradford M.A. (2013b). Creep of concrete core and time-dependent non-linear behaviour and buckling of shallow concrete-filled steel tubular arches. *Computer Modelling in Engineering and Science, 95 (1),* 32-58.

Luo K., Pi Y.-L., Gao W., Bradford M.A. & Hui D. (2015). Investigation into long-term behaviour and stability of concrete-filled steel tubular arches. *Journal of Constructional Steel Research, 104,* 127-136.

Magnucka-Blandzi E. (2008). Axi-symmetrical deflection and buckling of circular porous-cellular plate. *Thin-Walled Structures, 46,* 333-337.

Magnucka-Blandzi E. (2010). Non-linear analysis of dynamic stability of metal foam circular plate. *Journal of Theoretical and Applied Mechanics, 48,* 207-217.

Magnucki K. & Stasiewica P. (2004). Elastic buckling of a porous beam. *Journal of Theoretical and Applied Mechanics, 42(4),* 859-868.

Ma, Y. S. and Wang, Y. F. (2013). Creep effects on the reliability of a concrete-filled steel tube arch bridge. *Journal of Bridge Engineering, 18(10):* 1095 - 1104.

Pi Y.-L. & Bradford M.A. (2014). Long-term analyses of concrete-filled steel tubular arches accounting for interval uncertainty. *CMES: Computer Modelling in Engineering & Sciences 99 (3),* 233-253.

Pi Y.-L., Bradford M.A. & Qu W. (2011). Long-term non-linear behaviour and buckling of shallow concrete-filled steel tubular arches. *International Journal of Non-Linear Mechanics 46, (9)* 1155–1166.

Pi Y.-L., Bradford M.A. & Tin-Loi F. (2007). Nonlinear analysis and buckling of elastically supported circular shallow arches. *International Journal of Solids and Structures, 44 (7-8),* 2401-2425.

Pi Y.-L., Bradford M.A., Tin-Loi F. & Gilbert R.I. (2007). Geometric and material nonlinear analysis of elastically restrained arches. *Engineering Structures 29 (3)* 283–295.

Pi Y.-L., Bradford M.A. & Uy B. (2002). In-plane stability of arches. *International Journal of Solids and Structures, 39*, 105–125.

Pi Y.-L., Liu C., Bradford M.A. & Zhang S. (2012). In-plane strength of concrete-filled steel tubular circular arches. *Journal of Constructional Steel Research 69,* 77–94.

Pi, Y.-L. and Trahair, N. S. (1996). Three-dimensional nonlinear analysis of elastic arches. *Engineering Structures, 18(1):* 49 - 63.

Pi Y.-L. & Trahair N.S. (1998). Non-linear buckling and postbuckling of elastic arches. *Engineering Structures, 20 (7),* 571–579.

Pi Y.-L. & Trahair N.S. (1999). In-plane buckling and design of steel arches. *Journal of Structural Engineering 125 (11),* 1291-1298.

Rafiee M.A. et al. (2009) Enhanced mechanical properties of nanocomposites at low graphene content. *ACS Nano, 3*(12) 3884-3890.

Ranzi, G., Leoni, G., and Zandonini, R. (2013). State of the art on the time-dependent behaviour of composite steel-concrete structures. *Journal of Constructional Steel Research, 80:* 252 - 263.

Shafiee H., Naei M.H. & Eslami M.R. (2006). In-plane and out-of-plane buckling of arches made of FGM. *International Journal of Mechanical Sciences, 48,* 907–915.

Shahverdi H. & Barati M.R. (2017). Vibration analysis of porous functionally graded nanoplates. *International Journal of Engineering Science, 120,* 82-99.

Shaker A., Abdelrahman W., Tawfik M. & Sadek E. (2007), Stochastic Finite element analysis of the free vibration of functionally graded material plates. *Computational Mechanics, 41(5):* 707 – 714.

Şimşek M., Kocatürk T., (2009), Free and forced vibration of a functionally graded beam subjected to a concentrated moving harmonic load, *Composite Structures, 90:* 465-473.

Song M., Kitipornchai S. & Yang J. (2017). Free and forced vibrations of functionally graded polymer composite plates reinforced with graphene nanoplatelets. *Composite Structures, 159,* 579-588.

Song M., Yang J., Kitipornchai S. & Zhu W. (2017). Buckling and postbuckling of biaxially compressed functionally graded multilayer graphene nanoplatelet-reinforced polymer composite plates. *International Journal of Mechanical Sciences, 131-132,* 345-355.

Srividhya S., Raghu P., Rajagopal A. & Reddy JN. (2018). Nonlocal nonlinear analysis of functionally graded plates using third-order shear deformation theory. *International Journal of Engineering Science, 125,* 1-22.

Taczała M., Buczkowski R. and Kleiber M. (2017) Nonlinear buckling and post-buckling response of stiffened FGM plates in thermal environments, *Composites Part B, 109:* 238 - 247

Taati E. (2018). On buckling and post-buckling behavior of functionally graded micro-beams in thermal environment. *International Journal of Engineering Science, 128,* 63-78.

Walker, A. C. (1969). A non-linear finite element analysis of shallow circular arches. *International Journal of Solids and Structures, 5(2):* 97 - 107.

Wang Y., Feng C., Zhao Z. & Yang J. (2018). Eigenvalue buckling of functionally graded cylindrical shells reinforced with graphene platelets (GPL). *Composite Structures, 202,* 38-46.

Wang Y., Feng C., Zhao Z. & Yang J. (2017). Buckling of graphene platelet reinforced composite cylindrical shell with cutout. *International Journal of Structural Stability and Dynamics,* 18(3).

Wen, R. K. and Suhendro, B. (1991). Non-linear curved-beam element for arch structures. *Journal of Structural Engineering, ASCE, 117(11):* 3496 - 3515.

Wentzel D., Millers S. & Sevostianov. I. (2017). Dependence of the electrical conductivity of graphene reinforced epoxy resin on the stress level. *International Journal of Engineering Science, 120,* 63-70.

Wentzel D. & Sevostianov I. (2018). Electrical conductivity of unidirectional carbon fiber composites with epoxy-graphene matrix. *International Journal of Engineering Science, 130,* 129-135.

Wu B., Wu D., Gao W. & Song C. (2016a). Time-variant random interval response of concrete-filled steel tubular composite curved structures. *Composites Part B: Engineering, 94,* 122-138.

Wu D., Gao W., Feng J. & Luo K. (2016b). Structural behaviour evolution of composite steel-concrete curved structure with uncertain creep and shrinkage effects. *Composites Part B: Engineering, 86,* 261-272.

Wu D., Gao W. & Tangaramvong S. (2017a). Time-dependent buckling analysis of concrete-filled steel tubular arch with interval viscoelastic effects. *Journal of Structural Engineering 143(7),* 04017055, 127-136.

Wu D., Gao W., Gao K. & Tin-Loi F. (2017b). Robust safety assessment of functionally graded structures with interval uncertainties. *Composite Structures, 180:* 664-685

Wu D., Gao W., Hui D., Gao K. & Li K., (2017c). Stochastic static analysis of Euler-Bernoulli type functionally graded structures. *Composites Part B: Engineering, 134:* 69 - 80

Wu D., Liu A., Huang Y., Huang Y., Pi Y. & Gao W. (2018a). Dynamic analysis of functionally graded porous structures through finite element analysis. *Engineering Structures 165,* 287-301.

Wu D., Liu A., Huang Y., Huang Y., Pi Y. & Gao W. (2018b). Mathematical programming approach for uncertain linear elastic analysis of functionally graded porous structures with interval parameters. *Composites Part B: Engineering 152,* 282-291.

Wu H., Kitipornchai S. & Yang J. (2016). Thermal buckling and postbuckling analysis of functionally graded carbon nanotube-reinforced composite beams. *Applied Mechanics and Materials, 846,* 182-187.

Wu H., Kitipornchai S. & Yang J. (2017a). Imperfection sensitivity of thermal post-buckling behaviour of functionally graded carbon nanotube-reinforced composite beams. *Applied Mathematical Modelling, 42,* 735-752.

Wu H., Kitipornchai S. & Yang J. (2017b). Thermal buckling and postbuckling of functionally graded graphene nanocomposite plates. *Materials and Design, 132,* 430-441.

Wu H., Yang J. & Kitipornchai S. (2017). Dynamic instability of functionally graded multilayer graphene nanocomposite beams in thermal environment. *Composite Structures, 162*, 244-254.

Yang J., Wu H. & Kitipornchai S. (2017). Buckling and postbuckling of functionally graded multilayer graphene platelet-reinforced composite beams. *Composite Structures, 161*, 111-118.

Yang Z., Yang J., Liu, A. & Fu J. (2018). Nonlinear in-plane instability of functionally graded multilayer graphene reinforced composite shallow arches. *Composite Structures, 204:*301-312.

Zhao Z., Feng C., Wang Y. & Yang J. (2017). Bending and vibration analysis of functionally graded trapezoidal nanocomposite plates reinforced with graphene nanoplatelets (GPLs). *Composite Structures, 180:* 799-808.

Zuo Z.H., Xie Y.M. & Huang X. (2009) Combining genetic algorithms with BESO for topology optimization. *Structural and Multidisciplinary Optimization, 38:* 511-523